

PATTERN FORMATION IN A ROTATING
SUSPENSION OF NON-BROWNIAN
SETTLING PARTICLES

By
WILLIAM ROBERT MATSON
Bachelor of Science
Humboldt State University
Arcata, California
1999

Submitted to the Faculty of the
Graduate College of
The Oklahoma State University
in partial fulfillment of
the requirements for
the Degree of
DOCTOR OF PHILOSOPHY
July, 2004

PATTERN FORMATION IN A ROTATING
SUSPENSION OF NON-BROWNIAN
SETTLING PARTICLES

Thesis Approved:

Dr. Penger Tong

Thesis Advisor

Dr. Bruce Ackerson

Dr. Al Rosenberger

Dr. Frank Chambers

Dr. Al Carlozzi

Dean of the Graduate College

Preface

This study examines concentration and velocity patterns observed in a horizontal rotating cylinder completely filled with a monodisperse suspension of non-Brownian particles. A phase diagram is developed identifying velocity and concentration patterns, or *phases*, over a range of rotation rates and solvent viscosities. Individual phases are studied using both frontal (θ - z plane) and axial (r - θ plane) views in order to identify and collect information about each phase. Phase boundaries are defined which separate adjacent phases. Additional phase diagrams are developed using a different particle radius, cylinder radius, and several particle concentrations. An analysis of each boundary, and its functional dependence on particle radius, cylinder radius, and particle concentration, is provided in order to facilitate the theoretical understanding of this system. Several dimensionless parameters are presented and examined in a search for the forces governing the phase transitions.

I would like to thank the members of my advisory committee for their advice and insight: Dr. Penger Tong, Dr. Bruce Ackerson, Dr. Al Rosenberger, and Dr. Frank Chambers. I would also like to thank Warren Grider for his technical expertise and frank discussions. I would like to thank Mike Lucas and his staff for their assistance in manufacturing and designing the equipment used in this study. I would also like to thank my own colleagues, Makrand Kalyankar and Daniel Bergman, for their discussions, ideas, and assistance. My sincerest thanks goes to Dr. Paul Westhaus, without whom I would not be at Oklahoma State University. His assistance and valuable advice early in my graduate career has been of immense help. I would also thank the Department Head, Dr. Wicksted, for his advice and understanding. And finally, I would like to thank the Department of Physics as whole for providing me with a solid foundation upon which I can build a career in science.

Contents

Preface	iii
Nomenclature	x
1 Introduction	1
2 Background	3
3 Experimental Methods	7
3.1 Apparatus	7
3.1.1 Single Tube	7
3.1.2 Multiple Tube Rack	10
3.1.3 Short Cell	12
3.1.4 Motors & Drive Control Units	12
3.1.5 Precision Indexer	15
3.1.6 Temperature Controlled Environment	16
3.1.7 End View Imaging Tent	18
3.2 Preparation Procedures	18
3.2.1 Solution Preparation	18
3.2.2 Bead Size Analysis	22
3.2.3 Sample Preparation	23
3.2.4 Cylinder Preparation	26
4 Observations	27
4.1 General	27
4.2 (GB) Granular Bed	29
4.3 (F2) Fingering with 2 Flows	34
4.4 (F3) Fingering with 3 Flows	35
4.5 (LR) Low Rotation Transition - The Start of 3-D Flow	36
4.6 (BF) Band Formation	38
4.7 (DO) Pattern Drop-Out	43
4.8 (NH) Near Homogeneous Concentration	43
4.9 (HR) High Rotation Transition	44
4.10 (DG) Discontinuous Axial Gradient	45

4.11	(CD) Centrifugal Force Dominance	46
4.12	Coexistent States	47
4.12.1	General Concepts	47
4.12.2	(CL) Concentration Line Thickening	49
4.12.3	(OL) Outer Layer Development	49
4.12.4	(HF) High Frequency Structures	51
4.12.5	(SB) Segregation Band Structures	51
4.13	Transition Boundaries	52
5	Transition Boundary Analysis and Scaling	55
5.1	General Overview and Nomenclature	55
5.2	Power Law Models	56
5.2.1	GbF2 Boundary	56
5.2.2	DgCd Boundary	58
5.2.3	Power Law Results	58
5.3	Direct Plot Analysis	60
5.3.1	Particle Size Scaling	60
5.3.2	Cylinder Diameter Scaling	63
5.4	Dimensionless Parameter Analysis	68
5.4.1	Units Analysis	68
5.4.2	Dimensionless Boundary Analysis	70
5.5	Navier-Stokes Analysis	77
5.6	Volume Fraction Dependence	78
5.7	Correlation with Other Recent Experiments	78
5.7.1	Breu, Kruelle, and Rehberg (2003)[17]	78
5.7.2	Breu, Kruelle, and Rehberg (2004)[19]	80
5.7.3	Lipson (2001)[16]	81
5.7.4	Seiden, Lipson, and Franklin (2004)[20]	83
6	Conclusions and Recommendations	85
7	Bibliography	87
A	Theory and Design of the Custom Indexer	90
B	Temperature Controlled Environment Regulation System	93
B.1	Overview	93
B.2	Detection of the System Temperature	94
B.3	Positive Feedback	95
C	Program Code	97

D	Physical Properties of Materials and Solutions	116
D.1	Sources	116
D.2	Fluids	116

List of Tables

3.1	List of Cell Dimensions	8
3.2	Component volumes for two total quantities of the Standard, 76.96%M Solution	22
3.3	Component volumes for two total quantities of the 59.80%M solution	22
3.4	Inside Diameter Measurements in Millimeters	25
3.5	Inside Diameter Statistics for the Standard Tube	26
4.1	Band Spacing Statistics for the Standard Tube	42
5.1	Values of the Power Law Exponents and Amplitudes	60
5.2	Raw Scaling Parameters	66
5.3	Boundary Slope (M) values for the three systems	73
5.4	Boundary Intercept (B) values for the three systems	73
5.5	Intercepts using Average Slope	74
D.1	Properties of Water	116
D.2	Properties of Glycerine (Glycerol)	117
D.3	Properties of Plexiglas (Average)	117

List of Figures

3.1	Standard Single Tube Apparatus	8
3.2	Standard Tube Dimensions	9
3.3	Thermo-Neslab Refrigerated Bath unit Model RTE-211 with Digital Control Head	9
3.4	5-Tube Rack inside a temperature controlled box	10
3.5	Rack Drive Motor wrapped with copper tubing to reduce heat generation	11
3.6	View of Rack Drive Gear system	11
3.7	Front View of Short Cell	12
3.8	Side View of Short Cell	13
3.9	Breakdown of End View Cell	13
3.10	NEMA 23 frame Model M063-FD06 Stepper Motor	14
3.11	Compumotor C-Series Stepper Motor Driver	14
3.12	Custom designed Precision Indexer	15
3.13	Controlled Temperature Environment for 5-Tube Rack System	17
3.14	Sensor Temperature inside the Controlled Temperature Environment	18
3.15	Laser illumination	19
3.16	Measured viscosity of standard (76.96 mass percent) solutions at dif- ferent temperatures	21
3.17	Measured viscosity of 59.80 mass percent solution at different temper- atures	21
3.18	Size Distribution of Blue 200 and 100 micron samples	24
4.1	End View Image Composites	30
4.2	Front view light transmission still shots	31
4.3	Front view Absorption Plots	32
4.4	Front view Absorption Plots	33
4.5	Flow Paths	37
4.6	Low Rotation Transition Comparisons	39
4.7	Low Rotation Transition Comparisons	40
4.8	Low Rotation Transition with and without the granular bed	41
4.9	Band Angle Geometry	43
4.10	Front views of coexistent states	47
4.11	Coexistent State Absorption Plots	48
4.12	Outer Layer Development	50

4.13	Outer Layer Thickness versus Rotation Rate	50
4.14	High Frequency with Center Line Thickening	51
4.15	Raw Data Phase Transition Boundaries	53
4.16	Raw Data Coexistent State Onset Boundaries	54
5.1	Power law fit of GbF2 data	57
5.2	Log-Log plot of rescaled GbF2 data	57
5.3	DgCd Phase Transition Data for Standard System	59
5.4	DgCd with Newtonian Limit	59
5.5	Raw Data Phase Transition Boundaries for 100 micron sample	61
5.6	Raw Data Phase Transition Boundaries for 3.75cm diameter cylinder	62
5.7	Raw Scaling of 100 micron Boundaries	64
5.8	Raw Scaling of 100 micron Coexistant States	65
5.9	Raw Scaling of 100 micron Coexistent States	65
5.10	Raw Scaling of 375 micron Boundaries	67
5.11	Raw Scaling of 375 micron Coexistant States	68
5.12	Dimensionless Phase Diagrams	71
5.13	Dimensionless State Diagrams	72
5.14	Dimensionless Phase Diagrams using Average Slope	75
5.15	Dimensionless State Diagrams using Average Slope	76
5.16	Transition boundaries using different concentrations	79
5.17	Phase space covered by Breu <i>et al.</i> in their 2003 paper.	80
5.18	Phase space covered by Breu <i>et al.</i> in their 2004 paper.	82
5.19	Phase space covered by Lipson in the 2001 paper.	83
5.20	Phase space covered by Seiden <i>et al.</i> in their 2004 paper.	84
A.1	Circuit Diagram of Indexer	92
B.1	Block Diagram of Controlled Environment Regulation System	94
B.2	Thermistor Resistance and associated Temperature	95
B.3	Log Resistance versus Temperature	96

Nomenclature

mL	milliliter
%V	volume fraction, or percent by volume
%M	mass fraction, or percent by mass
a	particle radius
R	cylinder inside radius
L	cylinder inside length
ρ	density in grams per cubic centimeter
ρ_s	solvent density in grams per cubic centimeter
ρ_b	particle (bead) density in grams per cubic centimeter
$\Delta\rho$	buoyant density, $\rho_b - \rho_s$
μ	solvent viscosity in centipoise
r, θ , z	cylindrical coordinates
ω	angular velocity of the cylinder
g	gravitational acceleration
cm	centimeter, 10^{-2} meters
mm	millimeter, 10^{-3} meters
μm	micrometer, 10^{-6} meters
mA	milliamp, 10^{-3} amperes electrical current
ms	millisecond, 10^{-3} seconds
μs	microsecond, 10^{-6} seconds
ns	nanosecond, 10^{-9} seconds
Φ	mass percent variable
ϕ	particle concentration
V	volume
λ	wavelength
v_r , v_θ , v_z	suspension velocity components
T	period, in general
T_0	cylinder rotation period at $\mu = 0$
κ , Γ	power law fitting values
σ , γ	raw data scaling values
α , β , ζ , ϵ , χ , ξ	dimensionless parameter exponents
M, B	linear fitting parameters

Chapter 1

Introduction

Pattern formations have been observed since the dawn of civilization. From days of pre-history to the modern era, we have been fascinated by regularly spaced ripples in sand and on water, shapes of clouds and star-clusters, the rings which form around an impacting droplet of water on the surface of a lake, and the lively dance of the fingers of flame in a campfire. Ancient astrologers fancied the images of gods and heros in the positions of the stars. Ancient priests would observe patterns in the weather and the seasons over the course of years and even generations. Many of these mysteries have been solved in the last century, many more observations and conclusions have been lost to history in the face of modern science and skepticism, but some of the mysteries still remain. I will examine one such mystery in a very simple system: the patterns which emerge in a monodisperse suspension of non-Brownian particles in a horizontal, rotating cylinder.

Suspensions and particle laden flows play an important role in many commercial, residential, and environmental areas. Oil companies use particle laden flows to open or maintain fissures deep underground. Polishing compounds are essentially high concentration suspensions. Sedimentation in river beds and hillsides are of particular importance to environmental engineers and activists. Although commonplace, particle laden systems are mathematically complex and, consequently, little is completely understood. Theoretical research has focused mainly on dilute systems; nevertheless, empirical studies of particle laden flows can reveal many interesting features and render insight into the forces governing the behavior. Recent efforts using a variety of simulation techniques have met with modest success and may yet provide

detailed information through direct numerical implementation of the governing equations; however, the time needed to process significant sized samples is prohibitive. Current advancements in both hardware and software development may improve this situation considerably and allow for the simulation of reasonable sized samples over adequate periods of simulated time within a reasonable period of real time.

Empirical analysis of experimental data has allowed certain levels of advancement in the fields of hydraulic, aeronautical, and chemical engineering in spite of the absence of a complete or applicable theory; however, anomalies sometimes occur that are not captured by the rigid nature of the available empirical data, such as the spontaneous separation of reagents in a mixing vat. Pharmaceutical companies often spend millions of dollars in vain attempting to get completely homogeneous mixtures. The nearly infinite variations and lack of complete theoretical understanding means the construction design which works acceptably in one situation is often completely inadequate in another similar case. Empirical solutions are simply too numerous and costly to achieve for all possible permutations. Even an incomplete theoretical solution would be of immense value to these industries.

The system described in this study demonstrates a rich array of velocity fields and concentration patterns which occupy regions of physical phase space and are separated by *transition boundaries*. These boundaries are carefully mapped in physical phase space as defined by rotation period, t , and solvent viscosity, μ . Observations suggest the transition between adjacent phases might indicate a change in the balance of the forces governing the system; therefore, a careful study of the transition boundaries will suggest correlations between known (and unknown) forces in the form of dimensionless control parameters. This work seeks to identify the form of these parameters through empirical analysis by mapping the transition boundaries using a different particle size, cylinder size, and several concentrations. The effect on each transition boundary is examined using several analytical techniques.

Chapter 2

Background

In recent years, thin films seeded with a small volume fraction of granular material have attracted much attention. Various experiments have been carried out using both neutrally buoyant and heavier particles. Boote & Thomas[1] found that the modulated front observed in unseeded systems[2, 3, 4, 5, 6] occurs much earlier when granules are added, provided the volume fraction of the granular material is above a critical value. Thomas *et al.*[7] reported further work which detailed an even finer structure to the granular bands than indicated earlier. They showed the transition boundaries to be independent of granule size, and the characteristic wavelength of the granular bands to be independent of both granule size and shape. Tirumkudulu *et al.*[8] confirmed the suggestion of Boote & Thomas that this axial segregation is not a consequence of the wavy front noted by Melo[4]. Govindarajan, Nott, & Ramaswamy[9] claim to have resolved the axial segregation problem for granular seeded viscous films. Their analysis assumes the particle diffusion, driven by both a concentration gradient and a shear, is unstable to certain perturbations. Unfortunately, there are serious doubts about their results and conclusions. Acrivos recently published a scathing commentary citing numerous issues regarding their derivations[10]. Jin & Acrivos[11] suggested a similar theory for particle segregation based on the lubrication approximation and linear (axial) stability analysis.

Studies of partially filled Taylor-Couette devices seeded with particles have also received increasing attention in recent years[12]. Bands are observed around the central cylinder in concentrations as low as 1%V and as high as 65%V. The theoretical

explanation suggests the banding is due to the same shear-induced migration involving the free surface and film thickness described in the single cylinder coating flow.

A recent paper by Duong *et al.*[13] reported banding phenomena in a partially filled cylinder using very high concentrations of particles. Theoretical analysis was provided using Einstein's variable viscosity approximation and results in the coexistence of solid-like and fluid-like states which qualitatively agreed with observation. Raiskinmäki *et al.*[14] also recently used the variable viscosity method to study the clustering of particles in a Couette flow and its effects on viscosity in shear flows using direct numerical simulations. The observed behavior naturally divided into three regimes based on particle Reynolds number: ≤ 0.1 , ≈ 1 , and ≥ 10 .

Roberts *et al.*[15] provides an interesting theoretical study of a single particle inside a horizontal, rotating cylinder. Their calculations show a particle will continuously spiral outward until it reaches the wall. The time for the particle to reach the cell wall is given as

$$T_{out} = \frac{9\mu}{4a^2\Delta\rho\omega^2}Ln\left(\frac{R^2 - x_0^2}{\alpha^2}\right)$$

where the point at which gravity balances viscous drag is given by

$$x_0 = \frac{2\Delta\rho a^2 g}{9\mu\omega}$$

and α is the initial displacement from x_0 at $t = 0$. For our system, the migration time, T_{out} , is less than 10 minutes at $\mu = 40$ centipoise and $\omega = 5.236$ radians/second; however, velocity fields and concentration patterns have been observed under these conditions for several weeks without noticeable change. The collective dynamics of this rotating suspension are clearly inducing behavior very different from that of a single particle.

Lipson[16] reported band formation in supersaturated solutions of NH_4Cl while undergoing rotation in a horizontal drum (cylinder). Although the viscosity of the solution was not provided in the paper, the rotation rates are reported between $\frac{1}{2} \rightarrow 2$ seconds per rotation. Lipson reported spacial periodicity of $1.2 \rightarrow 1.7$ cylinder diameters independent of rotation rate. Lipson also observed band formations using

bubbles. Several possible explanations were suggested and subsequently disputed by Lipson in the same paragraph. Acoustic streaming was suggested and summarily dismissed, since the viscous penetration depth $\sqrt{\eta/\omega}$ is too short under these conditions. Saffman lift was considered as a focusing mechanism since the particles used were of near-neutral buoyancy. Lipson could not completely dismiss this mechanism, citing insufficient data to verify or disprove the arguments. Lipson also suggested that particle interactions mediated by the fluid might be significant.

Breu *et al.*[17] studied pattern formations of heavy particles undergoing high rotation rates. Patterns are observed when particles are pressed against the wall at rotation rates between 3.9 and 2.9 Hertz ($0.25 \rightarrow 0.34$ seconds per rotation). Their observed range agrees well with the phase diagram to be presented in Chapter 4. Breu *et al.* focuses on the growth and development of the instability. The explanation suggests that particles move off the wall near the top of the rotation cycle, then back onto the wall during the lower part of the cycle, following gravity. It is argued that this decreased path length allows particles to migrate along the wall and create the instabilities observed.

Lee & Ladd[18] attempted to model the band pattern reported in Section 4.6 by considering the hydrodynamic interaction of two particles of non-neutral buoyancy in the rotating cylinder. They argued that two particles at different radial positions would suffer different centrifugal forces and subsequently develop an attraction between them. Although the calculated onset times and axial spacing agrees with experiments, the observation of bands in suspensions of air bubbles, as in the case of Lipson, has brought their calculation into question.

Breu *et al.*[19] recently published a paper on traveling waves observed in rotating suspensions. Viscosities of $\approx 0.92, \approx 1.8, \approx 4.4$, & ≈ 7.8 centipoise (milli-Pascal Seconds) are used in the experiments. Space-time plots show particle concentration along the tube axis (z-axis) as a function of time. "Traveling waves" were not observed in the sample with $\mu = 0.92$. How their "traveling waves" compare with our results will be discussed in Chapter 5.

Seiden, Lipson, & Franklin[20] recently published a follow-up paper on Lipson's

earlier work[16]. Using water or dilute glycerin solutions, bands are reported using monodisperse suspensions of nylon, polystyrene, and plexiglass beads. Pictures of the bands over time indicate oscillation in the structures similar to that observed in Section 4.5. Seiden *et al.* are using, by comparison, very large spheres (3mm diameter) in large cylinders (4.5 centimeter diameter). Correlation between their observations and ours will be provided in Chapter 5. Seiden provides calculations of vector fields and wavelengths that agree with the observations provided in their paper, but not so well with the observations in this paper.

The work put forward in the following chapters will detail measurements in a completely filled, horizontal, rotating cylinder using monodisperse suspensions of silica glass spheres. Viscosities vary from 4 to 95 centipoise using glycerine-water solution under tightly controlled environmental conditions. Unlike the coating (rimming) flow examples of Acrivos, Melo, and others, this suspension does not possess a free surface. Unlike the Taylor-Couette device used by Timberlake and others, there is only the outer cylinder as a boundary condition; nevertheless, the system exhibits a profound variety of new velocity and concentration patterns in addition to those reported by Lipson and Breu. In Chapter 5, I will show how these tightly focused works can be incorporated into the global picture I will present. In doing so, this work will lay forth an unexplored realm of fluid physics that touches many works, including those by Acrivos, Melo, Timberlake, and many others.

Chapter 3

Experimental Methods

3.1 Apparatus

3.1.1 Single Tube

The majority of the experimental work is performed using a single horizontal cylinder similar to that shown in Figure 3.1. The cylindrical tube is constructed with one adjustable end and one fixed end to allow precise control of the tube length, as illustrated in Figure 3.2. The tube is constructed of Plexiglas, and the ends are made of brass. The ends of the tube are mounted on vertical supports with pressed ball bearings to minimize friction during rotation. The solid, fixed end of the tube is connected to a stepper motor using a thermal isolation coupler. The vertical support is thermally insulated from the mounting base as an added precaution. The base plate is equipped with adjustable legs to allow precise leveling, and anchor holes to keep the base positionally fixed on the optical table and provide a locking action for the leveling screws. A Plexiglas housing is constructed around the tube and supported by screws and guide shafts attached to the vertical supports, as seen in Figure 3.1. Seals allow tube rotation within the chamber with minimal leakage. A solution of water, glycerine, and soap is pumped through the chamber surrounding the rotating cylinder using a Thermo-Neslab Recirculator Bath temperature control system similar to that shown in Figure 3.3. Approximately 25 milliliters of soap per 7 liter reservoir is added to reduce surface tension and modify the affinity for adequate wetting of the Plexiglas surfaces. Approximately $\frac{1}{4}$ liters of glycerine per 7 liter reservoir is added to modify

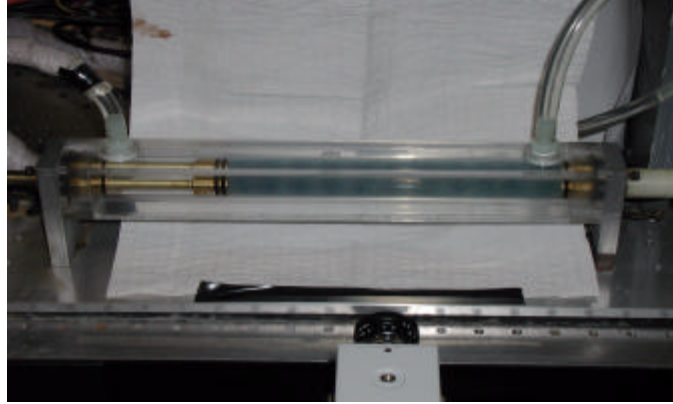


Figure 3.1: Standard Single Tube Apparatus

the index of refraction. The manufacturer claims temperature stability of the recirculation bath units is between 0.01° & 0.05° Celsius. The measured stability for most units is between 0.005° to 0.025° Celsius. The temperature regulated flow encompassing the cylinder reduces viscosity errors, and the modified index of refraction and external geometry reduces distortion, improving the ability to visualize the flow field. Digital controls allow precise temperature selection, and a temperature-dependence viscosity curve for a selected mass percent glycerin solution allows viscosity selection by setting the bath at the appropriate temperature. This allows flow phase measurements at multiple viscosities using a single suspension thereby reducing laboratory preparation time and materials consumption. The temperature drop across the tube length due to atmospheric exposure while transitting the box is too small to be accurately measured. Table 3.1 lists the physical dimensions of the cylinders used in the experiments. Further details regarding equipment configuration and usage will be described in Section 3.2.

Cell Group	Inside Diameter (cm)	Wall Thickness (cm)
Standard Cell	1.9	0.313
Double Diameter	3.8	0.625

Table 3.1: List of Cell Dimensions

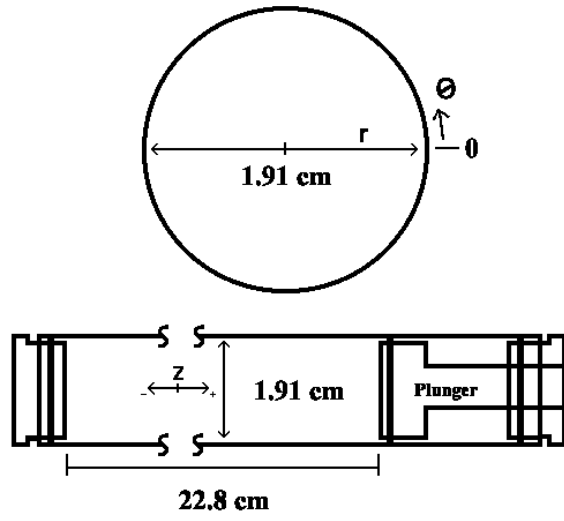


Figure 3.2: Standard Tube Dimensions



Figure 3.3: Thermo-Neslab Refrigerated Bath unit Model RTE-211 with Digital Control Head

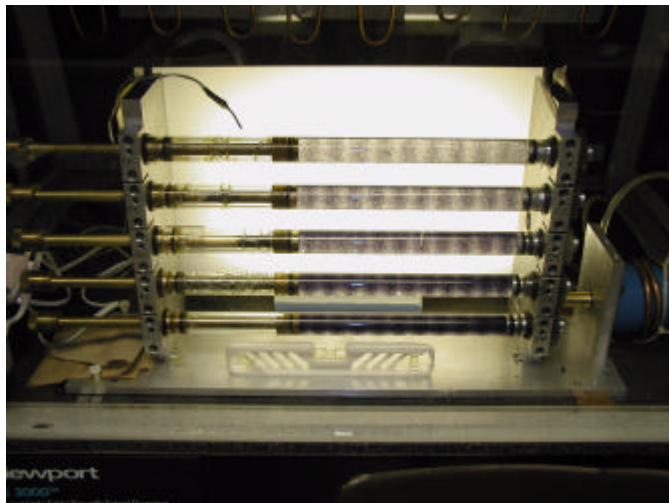


Figure 3.4: 5-Tube Rack inside a temperature controlled box

3.1.2 Multiple Tube Rack

The individual tubes are similar in construction to the "standard tube" outlined in Section 3.1.1. In this case, however, five tubes are mounted on a single set of vertical supports as shown in Figure 3.4. In place of the ball bearings used in the single tube support, low profile needle bearings are used to reduce vertical tube separation and the corresponding overall height of the system. Direct drive for the system is obtained through the gear drive system shown in Figure 3.6 powered by a single, high torque stepper motor. The entire system is enclosed in the temperature controlled environment shown in Figure 3.13. Details on the creation and control of this environment will be discussed in Section 3.1.6. The gear system uses interspatial idle gears and uniform drive gears to maintain speed and direction of rotation, allowing all tubes to rotate at the same speed and direction as the motor itself. To provide the large torque required, a Compumotor model M57-83 drive system is used, which includes both motor and driver as an inductively matched pair. Heat generation by the drive motor and fan motor are minimized by directing a portion of the coolant through copper tubes in thermal contact with these devices, as shown in Figure 3.5.

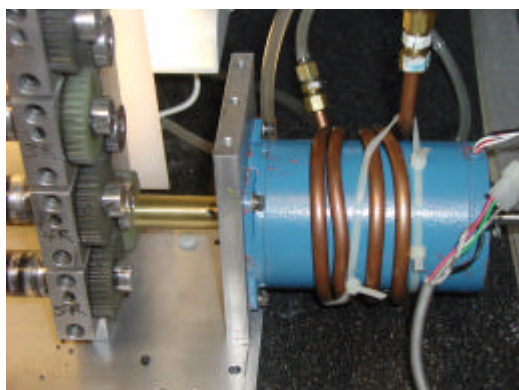


Figure 3.5: Rack Drive Motor wrapped with copper tubing to reduce heat generation

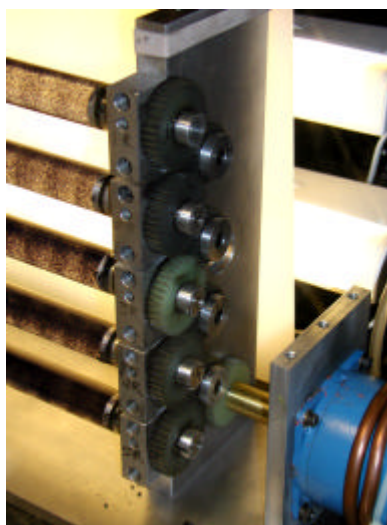


Figure 3.6: View of Rack Drive Gear system

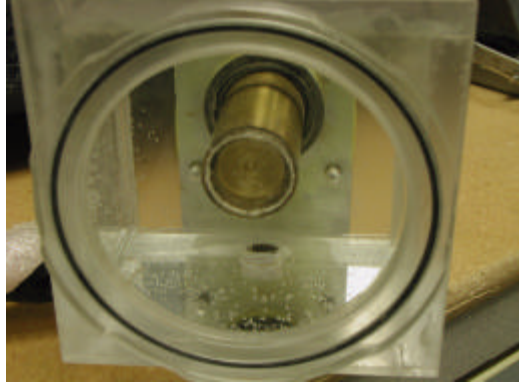


Figure 3.7: Front View of Short Cell

3.1.3 Short Cell

A special short cell is constructed to allow the viewing of cross-sections ($r - \theta$ plane) of the flow field and the performance of particle image velocimetry. This cell is also adjustable in length and is normally set to 2.2 centimeters, or one average band length. The adjustable end is constructed of brass with a threaded plunger for adjusting length, a threaded plexiglass cylinder with sealed plexiglass end cap, and an outer brass retaining shell. A threaded plug is used to allow excess fluid to escape during the final assembly process when sample length is set. A lock ring is used on the plunger to prevent vibrational or rotational drift of the plunger.

The brass outer shell passes through the vertical support and screws into a thermal insulating shaft connected to the drive motor. Passage through the support utilizes a ball bearing and a seal to minimize friction and prevent leakage, respectively. The water chamber surrounding the cell is also made of polished Plexiglas to allow viewing of the tube with one end anchored to the single vertical support. The entire system is mounted on an adjustable plane to allow adjustment of the cylinder with respect to the light sheet and camera used to illuminate and view the cross-section. Details regarding imaging and illumination are provided in Section 3.1.7.

3.1.4 Motors & Drive Control Units

All single tube systems are driven by a NEMA 23 frame 6-wire SLO-SYN synchronous stepper motor. The long single tubes are driven by a model M063-FD06

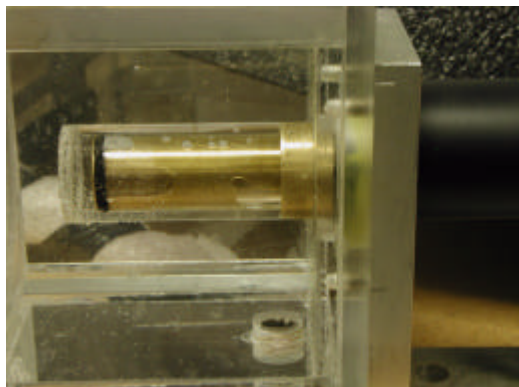


Figure 3.8: Side View of Short Cell

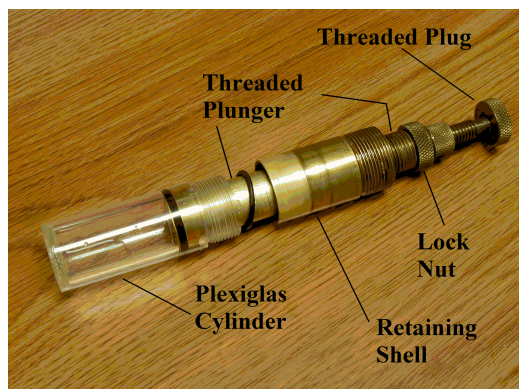


Figure 3.9: Breakdown of End View Cell



Figure 3.10: NEMA 23 frame Model M063-FD06 Stepper Motor

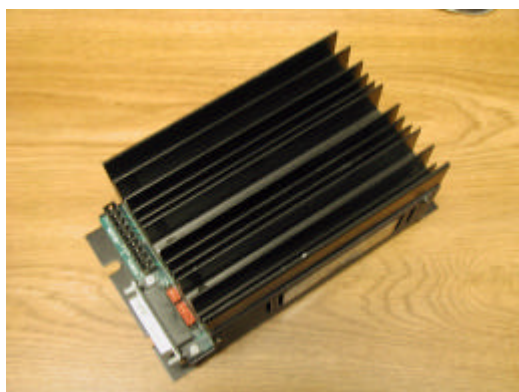


Figure 3.11: Compumotor C-Series Stepper Motor Driver

motor similar to the one shown in Figure 3.10, whereas the short cell, which requires less torque, uses a model M061-FC02. Each motor is controlled using a Compumotor C-Drive control unit, as shown in Figure 3.11. Power for the logic circuit is provided using the 12VDC output from a standard computer power supply. This power source is also used for the motor in low current requirement systems, such as the short cell discussed in Section 3.1.3. For the higher current requirement systems, such as the double diameter tube, the motor is powered using a Sorensen adjustable regulated power supply. Two models are used: DCS 60-18 and DCS 150-7. Stepping direction and speed are governed using a custom built, high precision indexer to be described in section 3.1.5. The drive motors are thermally isolated from the rotating cells using an insulating coupler about 4 inches in length.

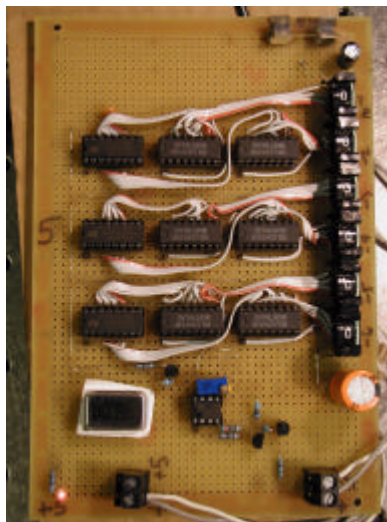


Figure 3.12: Custom designed Precision Indexer

3.1.5 Precision Indexer

The Compumotor C-Drive Control Unit shown in Figure 3.11 requires a standard TTL pulse to increment motor position. These units have a step resolution of 25,000 pulses per rotation. A single 5VDC input can be applied to the Direction Pin to reverse the direction of rotation.

Standard pulse generators typically drift several Hertz in output frequency over a short period of time. This error tends to increase linearly with frequency resulting in errors as large as 150Hz per 500kHz. The output current is typically limited to a few milliamps. Frequency selection is generally crude, since a single rotation of the control knob spans the entire range. The ease of rotation and general mechanical nature of rotary systems contribute to a long term drift in frequency, in addition to the more rapid fluctuations mentioned previously.

For their designated purpose, these capacities and accuracies are more than acceptable; however, the 250mA current requirement of the C-Drive input signal exceeds the capacity of many function generators on the market, and the resulting reduced signal amplitude creates large, irregular errors in rotation period. The frequency drift is unacceptable since the phase boundaries to be studied are sharp with long onset times. Some phase boundaries are less than 0.025 seconds per rotation in width, and the time to reach steady state can be as much as 18 hours. The needed resolution

and stability requirements made it necessary to design and construct the precision indexer shown in Figure 3.12. Details regarding theory of operation, circuit diagrams, and construction are included in Appendix A. The indexer has a resolution of $1\ \mu\text{s}$ per pulse with $< 0.1\text{ns}$ variance per pulse. Indeed, the frequency fluctuations over time could not be measured using any of the oscilloscopes or counters available in the laboratory.

3.1.6 Temperature Controlled Environment

The size and design of the 5-tube rack made construction of a fluid tight enclosure impractical; therefore, I decided on controlling the atmosphere around the tubes within a confined space. Though this lacked the ability to properly index match the surroundings for easy flow visualization, it did resolve the viscous drift associated with an unregulated environment such as the laboratory rooms and allowed for temperature selection of viscosity as discussed in Section 3.1.1.

The box in Figure 3.13 is made of $\frac{1}{4}$ inch Plexiglas. The outside surface is covered with (black) foam insulation using double sided tape and weather stripping adhesive at the edges. The box is placed on a single piece of foam insulation, isolating it, and anything inside it, from the metal surface of the optical table. Observations can be made using a cut-away section on the front. Interior access is gained by a removable panel on each end. It is presumed the temperature near the walls would be somewhat higher than the regulated temperature; therefore, the tubes are placed about 4 inches from the front wall. This also allows access to the bolts holding the tubes so they can be removed individually without disturbing the rack itself. The leveling screws in the base plate of the rack are placed on metal plates to prevent sinking into the foam insulation. Slits are cut to allow plastic bolts passing through the anchor holes in the base plate of the rack to reach the threaded holes in the optical table. Insulating foam is not removed. Instead, the foam is allowed to reform around the bolt once in place thereby maintaining the integrity of the insulation. Plastic bolts are used to maintain isolation from the metal surface of the optical table.

To add or remove heat from the system, copper tubing is shaped into a large coil

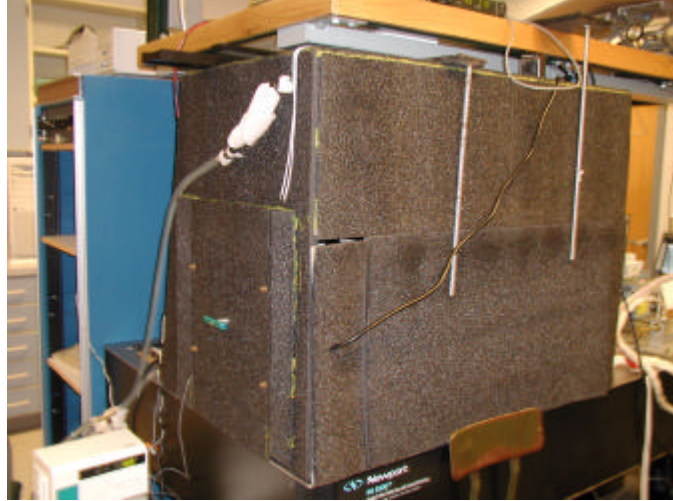


Figure 3.13: Controlled Temperature Environment for 5-Tube Rack System

along the back wall of the chamber. Water mixed with ethylene glycol is pumped through the tubing using a Neslab Recirculator bath similar to that in Figure 3.3. A large electric fan is used to disrupt natural convective currents and isolated pockets inside the chamber. The fan is located in the extreme rear of the chamber and blows directly onto the copper pipes. A temperature sensor, seen hanging behind the tubes in Figure 3.4, detects the current atmospheric temperature inside the chamber. A computer program reads this information, tracks the temperature over time, and calculates needed changes in the coolant temperature in response to any drift. Details of this regulation system are given in Appendix B, and the computer code is provided in Appendix C. The plot of temperature versus time in Figure 3.14 shows the temperature inside the box (near the cylinders) fluctuates less than 0.02° Celsius over several hours; therefore, the temperature regulation inside the chamber is comparable to that of the Neslab Bath units.

To view the flow patterns of the tubes while inside the chamber, the tubes are illuminated from behind. Two 14 inch florescent lights provide illumination behind a diffusion plate.

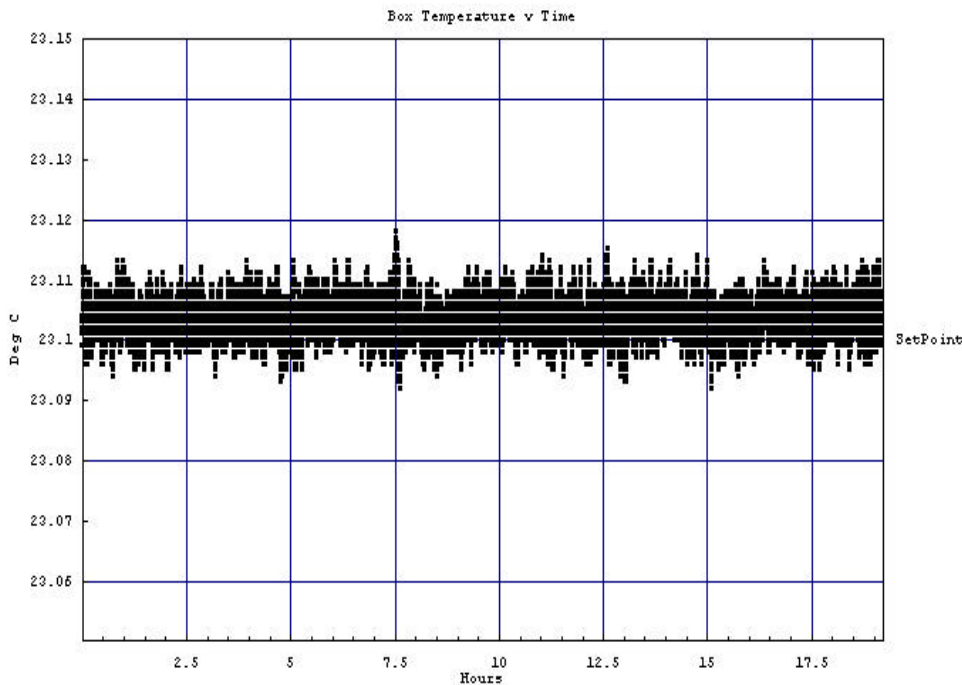


Figure 3.14: Sensor Temperature inside the Controlled Temperature Environment

3.1.7 End View Imaging Tent

Cross sections of the flow field (r - θ plane) are observed using a CCD camera positioned in front of the Short Cell discussed in Section 3.1.3. Illumination is provided by a single He-Ne laser. Shadows are reduced by illuminating the sample from both sides using two opposing sheets generated by splitting a single beam and using a glass rod on each side of the chamber, as shown in Figure 3.15. To reduce room light contamination, the apparatus is enclosed in a tent made of black cloth. Images are captured using an Integral Technologies Flashbus MV-Pro video capture card and processed using Image Pro software from Media Cybernetics.

3.2 Preparation Procedures

3.2.1 Solution Preparation

All aqueous solutions are prepared based on the mass percent of glycerine required for a given mixture. Most preparations use a 76.96% M glycerine solution. To prevent

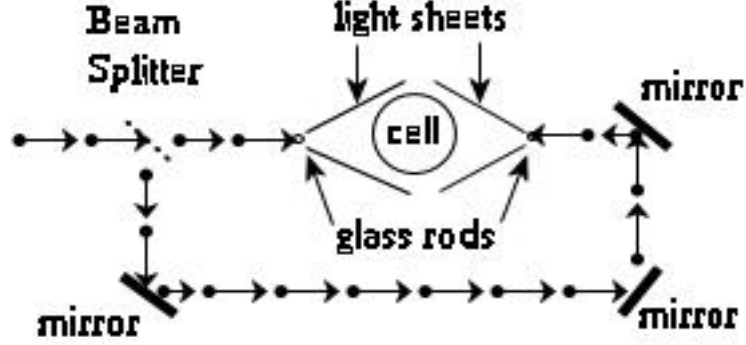


Figure 3.15: Laser illumination

particle aggregation, $\frac{1}{4}$ mL of soap is added for each 100 mL of total solution. Typical component volumes for the 76.96%*M* solution are given in Table 3.2. *Note the volume of water and soap are combined in the formula.*

The volume requirements for a given mass percent, Φ_G , are determined using the properties of glycerine detailed in Appendix D. The volume of water, V_w , and glycerine, V_G , are related by the following equations:

$$\Phi_G = \frac{V_G \rho_G}{V_w \rho_w + V_G \rho_G}$$

$$V_w \rho_w \Phi_G = V_G \rho_G (1 - \Phi_G)$$

$$V_{tot} \rho_w \Phi_G = V_G (\rho_G + (\rho_w - \rho_G) \Phi_G) \quad (3.1)$$

where

$$V_{tot} = V_w + V_G$$

Due to its large viscosity, the glycerine component is measured in the graduated cylinder which will hold the final mixture. To prevent absorption of water from the atmosphere, the cylinder top is covered with Parafilm and secured. The glycerine should be allowed to settle for at least 12 hours to allow air trapped during the dispensing process to escape. The soap is placed in a separate graduated cylinder by pipet. The necessary additional water is added to the soap, and the combination is added to the glycerine. This separate graduated cylinder does not allow complete dispensing of water, so an additional amount of water is added by pipet until the total volume of solution agrees with calculation. The solution is covered, mixed, and set aside for at least 12 more hours. This allows the air trapped during the mixing process to exit the solution completely. Any remaining foam on the surface of the solution is then suctioned off to prevent secondary contamination of the clear fluid. The solution is now ready for use.

This procedure, though tedious and time consuming, produces identical solutions every time. Figure 3.16 illustrates the measured viscosities of 3 different mixtures of 76.96%*M* glycerine solution made in the laboratory as a function of temperature. The dashed curve can be accurately modeled by the following polynomial where the temperature, x , is in degrees Celsius, and viscosity, μ , is in centipoise.

$$\mu = 162.7 - 10.65x + 0.3193x^2 - 4.655 \cdot 10^{-3}x^3 + 2.654 \cdot 10^{-5}x^4 \quad (3.2)$$

The consistent results depicted in Figure 3.16 demonstrates Equation 3.2 can accurately predict the viscosity of the 76.96%*M* solution at any temperature between 5° and 40° Celsius. The corresponding viscosity range is approximately 18 to 110 centipoise with an accuracy of 5%. Any desired viscosity within this range can be selected by tuning the water bath to the correct temperature. A similar viscosity curve was measured for the 59.80%*M* solution. The corresponding equation for this solution is

$$\mu = 29.77 - 1.32x + 0.01916x^2 \quad (3.3)$$

A consequence of using temperature to control viscosity is a simultaneous change in the density of both water and glycerine. Careful examination of the information provided in Appendix D shows these changes to be < 1% in magnitude for water.

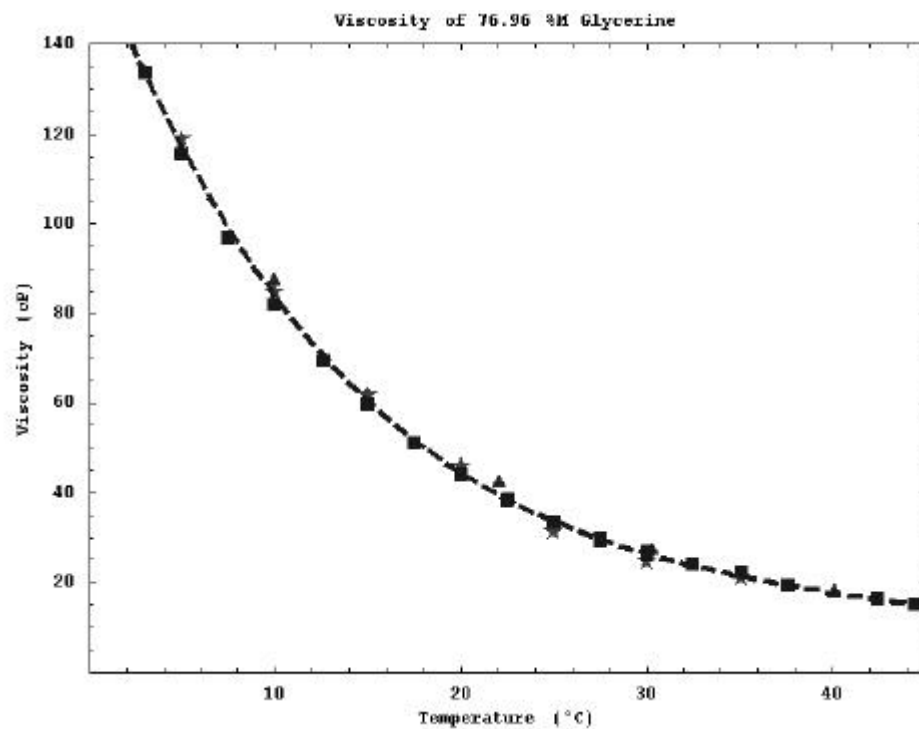


Figure 3.16: Measured viscosity of standard (76.96 mass percent) solutions at different temperatures

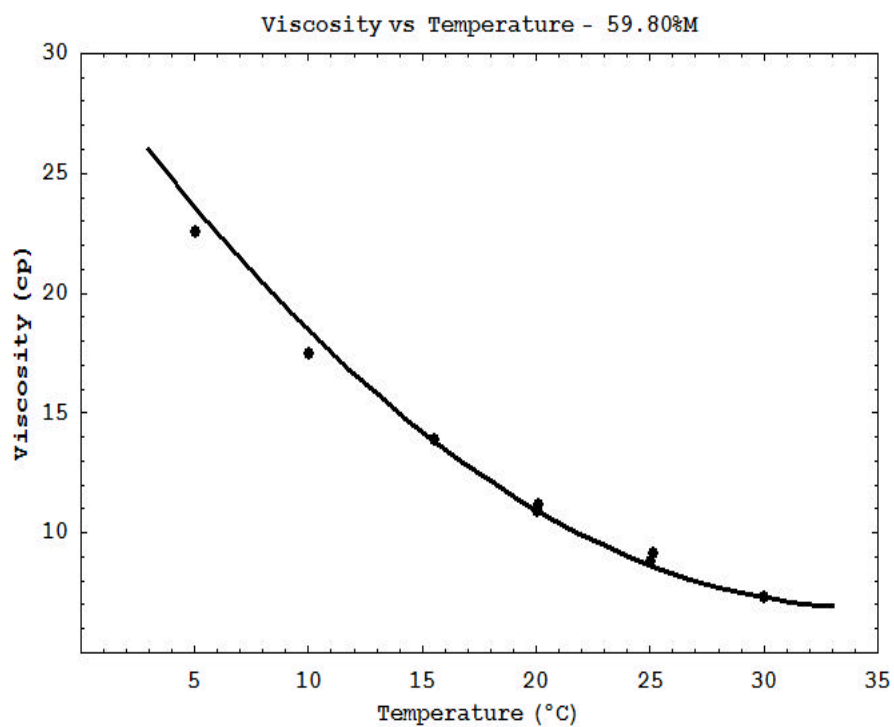


Figure 3.17: Measured viscosity of 59.80 mass percent solution at different temperatures

Although specific data for the corresponding change in glycerine is not available, it can be assumed comparable to that of water making the estimated overall change for $\Delta\rho = \rho_G - \rho_W \ll 1\%$.

Component	Small Volume (mL)	Large Volume (mL)
Glycerine	72	160
Soap & Water	27	60
Total Solution	99	220

Table 3.2: Component volumes for two total quantities of the Standard, 76.96%M Solution

Component	Small Volume (mL)	Large Volume (mL)
Glycerine	38	95
Soap & Water	32	80
Total Solution	70	175

Table 3.3: Component volumes for two total quantities of the 59.80%M solution

3.2.2 Bead Size Analysis

The materials supplier provided laser scattering results for the bead samples; nevertheless, I personally measured the particle diameter, roundness, and density before preparing samples. The 200 micron particles are reported to have a mean diameter $2a = 199.2 \pm 21\mu m$ with a standard deviation of the size dispersion of $15.8\mu m$. The 100 micron particles are reported to have diameters from 75 to $180\mu m$. The standard deviation of the size dispersion is not provided for this sample. The spheres are reported to have a specific gravity of $\frac{\rho_b}{\rho_w} = 2.40 \pm 0.10$. At room temperature, this gives a density of $2.4\rho_w = \rho_b \approx 2.39\frac{g}{cc}$. Direct measurement using volume displacement gives an average density of $2.35 \pm 0.05\frac{g}{cc}$. For particles of this size, the thermal diffusion is negligible compared to the hydrodynamic diffusion.

Size distributions for both the $100\mu m$ and $200\mu m$ samples are shown in Figure 3.18. Bead diameters were collected from several calibrated images taken with a microscope. Distribution plots were generated by counting the number of beads

with a given size $\pm 1\mu m$. This generates "bins" $2\mu m$ in size. The number of beads in each "bin" is then normalized by the total number in the sample to give the percentage shown on the vertical axis. The $200\mu m$ sample shows a tight dispersion around $198\mu m$. The standard deviation of the size dispersion is $\approx 27\mu m$. The $100\mu m$ sample shows a considerably wider distribution curve, but one that agrees well with the size range reported by the manufacturer. The curve is centered around $104\mu m$ with a standard deviation of the size dispersion of $\approx 43\mu m$.

3.2.3 Sample Preparation

Before setting out to prepare the sample, an accurate measurement of the cylinder inside diameter must be made in order to calculate the overall volume of the cylinder. Several measurements of the inside diameter are made using both ends of the tube for maximum sample diversity. Table 3.4 shows the actual measurements using a micrometer. Table 3.5 shows the statistics gleaned from these measurements. Based on these values, the mass necessary to reach the prescribed volume fraction can be calculated as follows.

$$V_{bead} = \phi V_{cyl}$$

$$\frac{M_{bead}}{\rho_{bead}} = \phi \pi R^2 L$$

$$M_{bead} = \phi \rho_{bead} \pi R^2 L \quad (3.4)$$

The standard volume fraction, $\phi = 2.3\%$, is used in the experiments unless otherwise specified. For the standard tube in Table 3.5, Equation 3.4 gives a bead mass of:

$$M_{bead} = (0.023)(2.35 \frac{g}{cm^3})\pi(\frac{1.9137}{2}cm)^2(22.75cm) = 3.5368g \quad (3.5)$$

When loading the cylinder, several methods are used in attempting to minimize complications. The main challenge in loading cylinders is purging air from the system. The beads are a significant source of air entrainment and can present a challenge

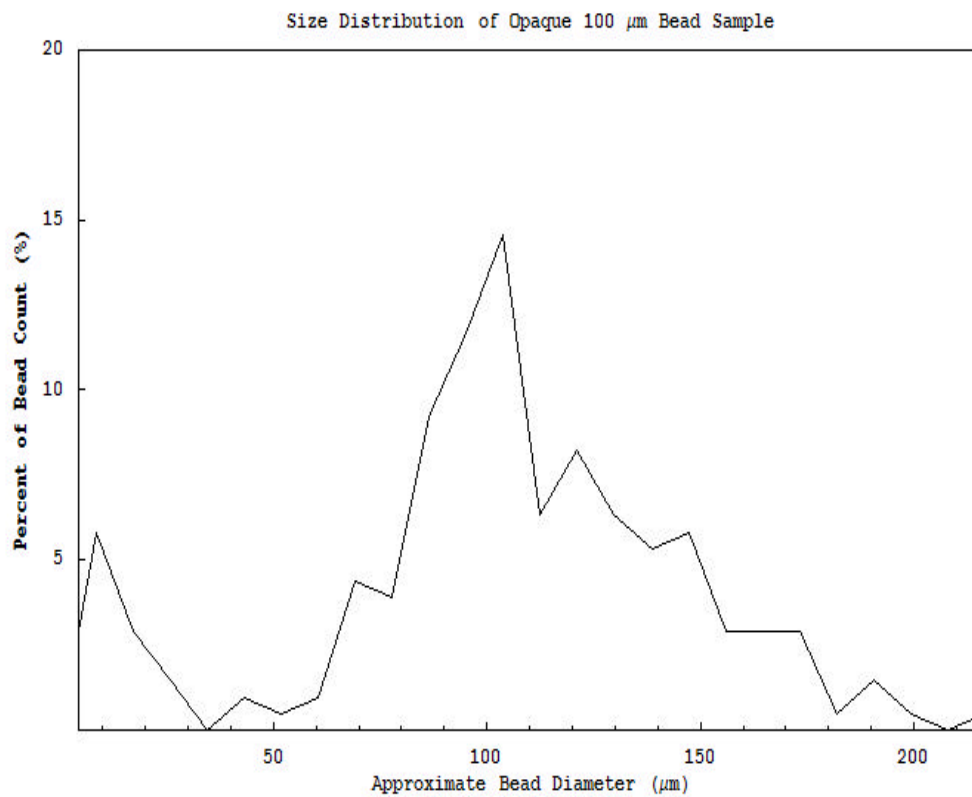
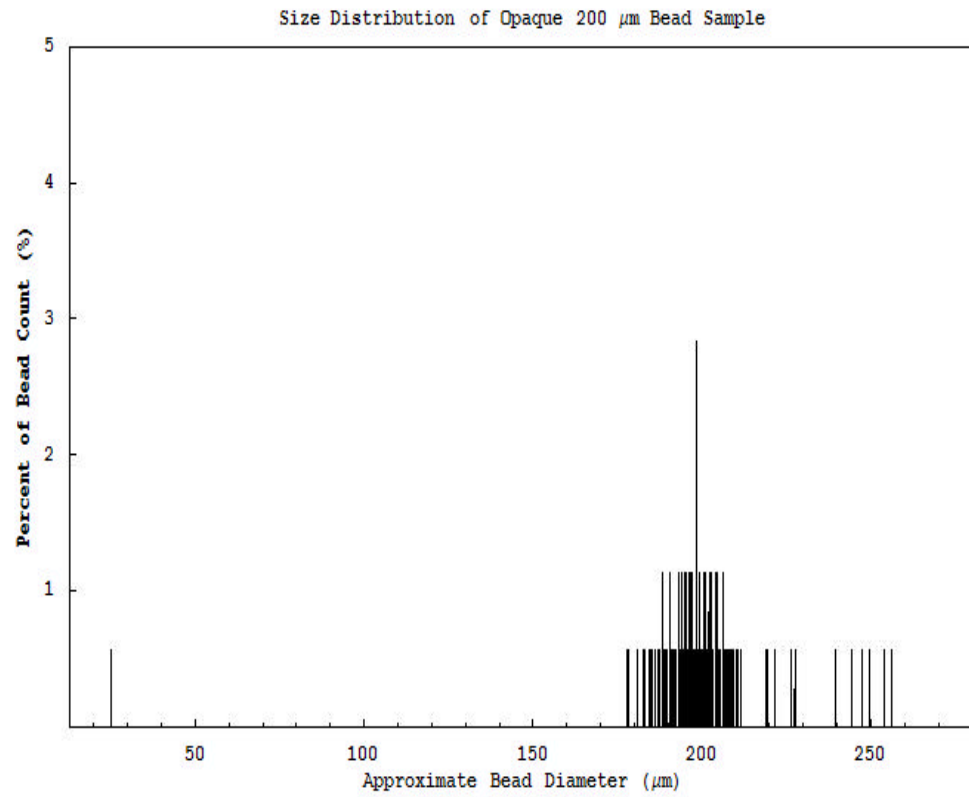


Figure 3.18: Size Distribution of Blue 200 and 100 micron samples

during preparation. Washing the beads in a small beaker using a small volume of solution has proven the best method of air removal, but can also cause errors in total mass retention if care is not taken to rinse the beaker completely with solution during the transfer stage.

Other primary sources of air entrainment are the cylinder ends. Low quality o-rings can introduce air into the system from small cracks within the rings. Poor fitting rings can also trap air in the groove around the ring. Installing the o-rings while submerged in solution can minimize or eliminate these complications. Care should be taken throughout the assembly stage to remove air from the system at each step, and prevent the air from being reintroduced.

Should air be introduced at any stage of assembly or during measurements, it must be removed. Air bubbles have not been observed to significantly modify the transition boundaries, but they do perturb the system and make phase identification difficult. The most effective method to remove air from the sample involves centrifuging. Centrifugal force drives the particles to the wall and the bubbles to the center of the cell. Placing the system on an incline and opening the plug allows air to travel up the plunger and out of the system. Once all air is removed from the system, the cylinder length can be reset and the plug replaced.

Sample	Standard	Double	Short Cell
1	19.27	36.86	18.43
2	18.88	36.88	18.43
3	19.28	36.87	18.39
4	19.26	36.85	18.46
5	18.97	36.90	18.42
6	19.21	36.85	18.37
7	18.94	36.91	18.38
8	19.29	36.84	18.40
9	19.35	36.87	18.39
10	18.88	36.95	18.46
11	19.33	36.90	18.43
12	18.98	36.86	18.49

Table 3.4: Inside Diameter Measurements in Millimeters

Statistic	Standard	Double	Short Cell
Mean	19.137	36.878	18.421
Median	19.235	36.87	18.425
Std Dev	0.188	0.032	0.037
Minimum	18.88	36.84	18.37
Maximum	19.35	36.95	18.49

Table 3.5: Inside Diameter Statistics for the Standard Tube

3.2.4 Cylinder Preparation

Once the system is running, the cylinder must be leveled. A bullet level can get you close, but it is not accurate enough for several reasons. Primarily, the surface that needs to be leveled is the *inside* wall of the cylinder. Since this wall is inaccessible, other surfaces are used which are not necessarily parallel to the inside surface of the cylinder; consequently, the cylinder must be run for several hours and the concentration profile is examined for the presence of axial stratification. Ideally, increasingly fine adjustments are made to correct for the stratification and the process is repeated until all signs of stratification are eliminated.

Different phases have different sensitivities to the leveling of the cylinder. Naturally, cylinders should always be leveled as accurately as possible to maximize precision, but the system has demonstrated the ability to overcome small defects in tube level when sufficient secondary flow is present. The lower rotation rate phases, which possess the most dominant secondary flows, demonstrate the lower sensitivity to cylinder level imperfections. Although the low rotation rate phases are optimal for leveling in terms of speed, the Near-Homogeneous phase discussed in Section 4.8 is the most accurate for level alignment; unfortunately, it could take 24 hours or more for the phase to reach steady state for even the finest adjustment. This process can literally take weeks to complete. The process can be accelerated by first leveling the tube using low rotation rate phase, such as the Low Rotation Transition discussed in Section 4.5. The Near-Homogeneous phase can be used for a final fine adjustment, and the observed gradient can be eliminated by returning to the Low Rotation Transition phase for a brief period of time between the measurements.

Chapter 4

Observations

4.1 General

Two types of information are observed and characterized: the velocity, or flow field, and concentration profiles on both local and large scales. Flow fields are observed by particle tracking or image superposition. Concentration is characterized by local population measurements or optical transmission measurements. Velocity and concentration information is examined both on local length scales (particle diameter) and global length scales (tube length), as well as time scales from 1 second to several minutes. A particular *phase* corresponds to a specific set of velocity field and concentration pattern. Each *phase* exists independently within a specific region of *phase space*, $\{\mu, T\}$. A *phase boundary* separates two adjacent *phases* in *phase space*, and the mapping of these boundaries is the primary goal of these experiments. It is important to note: phases do not overlap, and hysteresis has not been demonstrated by any of the phase boundaries.

Many of the observed phases are periodic. There are two types of periodicity exhibited: temporal and spatial. Temporal periodicity would be similar to the form $\text{Cos}(\psi t)$, where ψ refers to the frequency, or inverse period, of the oscillation. It is common for the frequency of the pattern, ψ , to be dependent on the rotation rate of the cylinder, ω . Similarly, the spatial periodicity of the patterns would be of the form $\text{Cos}(\frac{2\pi}{\lambda} z)$, where λ refers to the wavelength of pattern. Again, it is common for the wavelength, λ , to be dependent on the rotation rate of the cylinder, ω .

Although ψ and λ are dependent on ω , this relationship is single-valued. A partic-

ular ω will yield a specific pair $\{\psi, \lambda\}$. The convergence over time to this set of values is roughly exponential, where ψ and λ have different convergence times, $T_\psi < T_\lambda$. In addition, the system often shifts mass from one region of the cylinder to another, changing the global concentration (particle concentration) field. This mass transfer can take several hours to complete, and the nature of this growth (or decay) curve is not understood. For lack of the perfect language, the term *steady state* is used to refer to the condition where ψ and λ are at their nominal values for a particular $\omega = \frac{2\pi}{T}$, and the redistribution of mass has been completed.

In order to determine the *phase boundaries*, the regions of *phase space* occupied by each *phase* must be identified. This involves careful observation and identification over a range of viscosities, μ , and rotation periods, $T = \frac{2\pi}{\omega}$. Before each observation is made, the system is allowed to reach *steady state*. The *phase* is identified and the parameters, $\{\mu, T\}$, are changed. This sequence repeats until the regions are well identified and the *phase boundaries* are clear. It is believed that the *phase boundaries* are indicative of some change in the balance of forces, and, by understanding these boundaries, we can subsequently understand the underlying physics.

Direct physical observation has identified a specific sequence of *phases* through which the system progresses as ω increases. The low speed extreme is the familiar fluidized **granular bed** phase. The high speed extreme is the expected **centrifugal dominance** phase in which all particles reside on the cylinder wall. These two phases will be discussed again here insofar as phase identification requires. Between these two extremes, however, a rich array of unexpected and interesting dynamics exists which are the main focus of this thesis. The system exhibits a total of 10 *phases* and 4 *coexistent states*. The *phases* will be described here in detail and in order of appearance with increasing ω . The *coexistent states* will then be defined and described in the same order. Names are suggested for each of the identified *phases* and *coexistent states* so the patterns can be referenced easily in the future.

While the labeling of these phases may be linguistically subjective and open to debate, the observation and identification of each phase is kept as rigid as experimentally possible in order to allow for independent verification and repeatability. The

method of identification is highly qualitative in many respects and, as such, of questionable reliability both to this author and the general audience. In order to obtain maximum repeatability and accuracy, the general definition of a *good* experiment, a consensus method is used whereby the *accuracy* of any given point is determined by the neighboring points and general alignment. If a point is off line, for example, it is remeasured for validity; however, this is not to say it is considered *invalid*. Due to the method of examination, any given point can be considered questionable, even if it agrees with others locally. It is not uncommon for that one point to be valid and the others found in error after repeated measurements in the area. It is the *overall consensus* of the points that is of significance. The Phase Diagrams presented in Figure 4.15 clearly shows that this consensus is determined by a significant quantity of points, not just two or three locally. It is the general trend, shape, and location of the boundaries which is of most significance. As demonstrated by the phase diagrams and the subsequent variance and analysis, the consensus method has proven quite accurate and reproducible experimentally.

4.2 (GB) Granular Bed

The lower limiting state is a fluidized bed sitting on the inside wall of the cylinder. As the cylinder rotates, the bed is carried up the rising wall. Gravity pulls the innermost particles downward creating a circulation within the bed. Steady state can be achieved which results in a fluidized granular flow similar in appearance to that observed using high viscosity liquids in the partially filled cylinder[6]. The flow inside the granular bed, however, is extraneous to the focus of this thesis. The particles of interest are those which depart from the granular bed and become suspended in the moving medium. Figure 4.1(GB) shows the particle streaks extending from the superior end of the granular bed, and the absorption of the loose particle by the granular bed following a single orbit. Particle orbits in this phase are not generally closed.

There are two distinct circulations present in this phase, though they lack uniformity and symmetry. The near bed counter-rotating flow (rotation opposite the

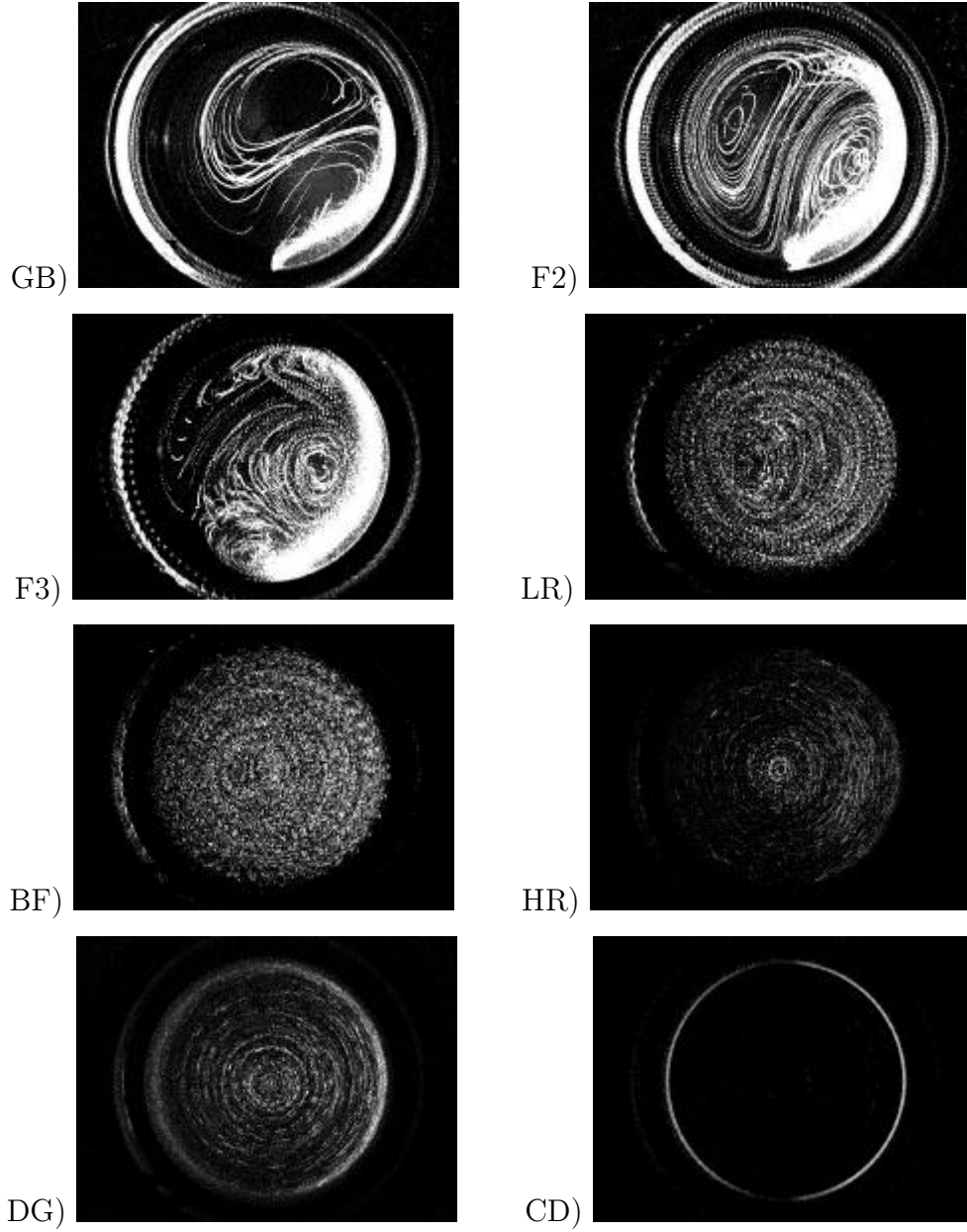
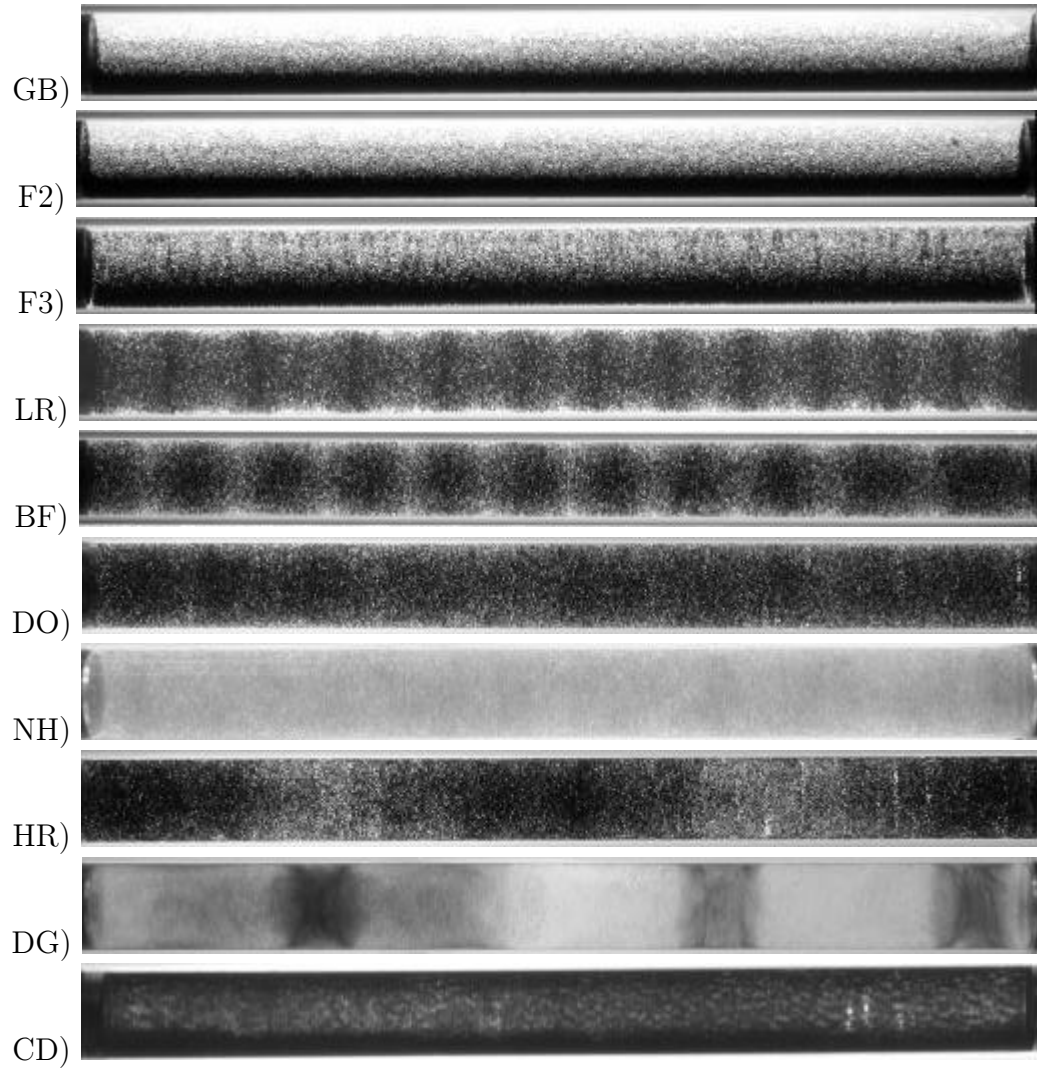


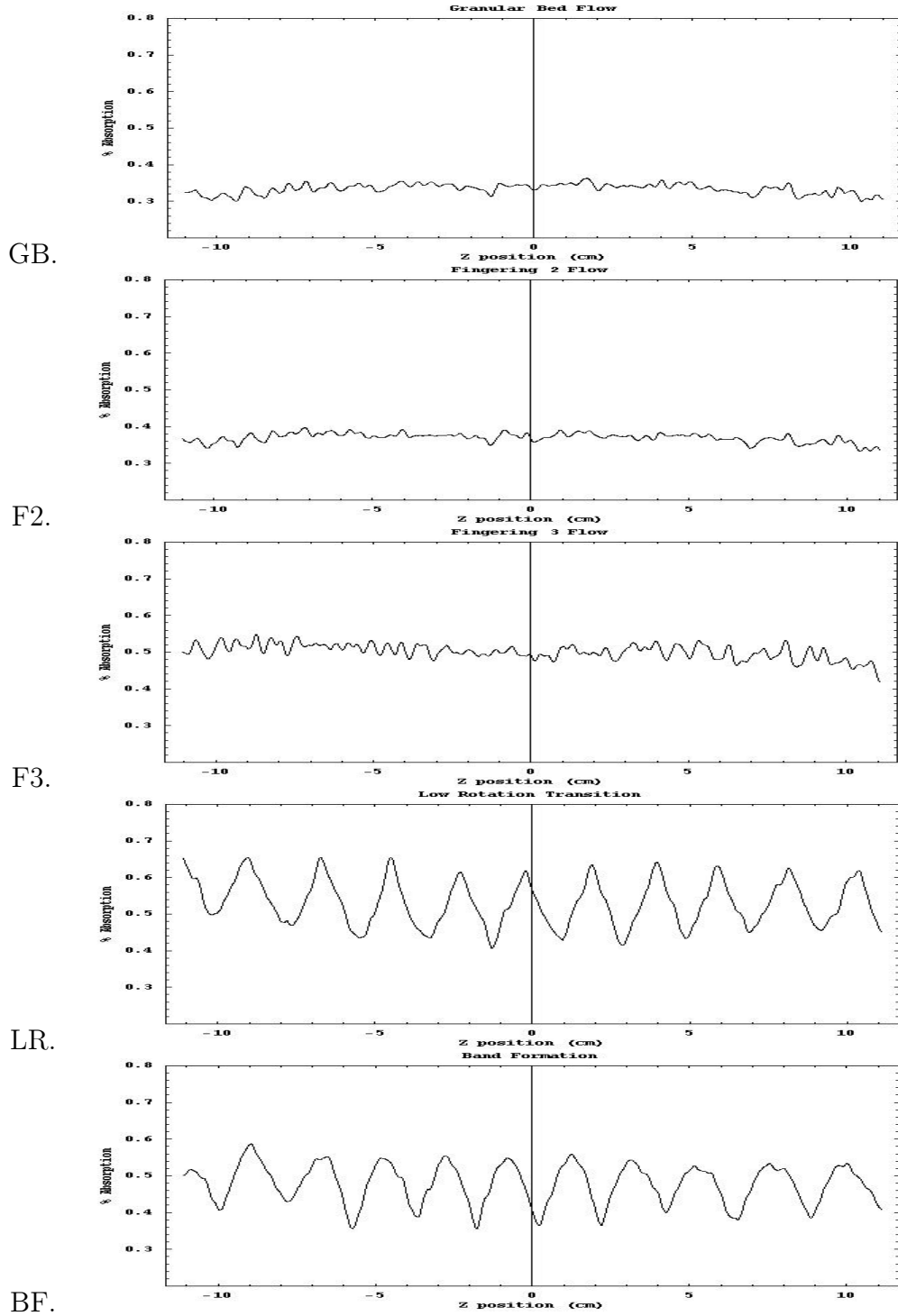
Image composites showing particle trajectories in the form of white streaks on black background. Phases illustrated are: (GB) Granular Bed Flow, (F2) Fingering 2 Flow, (F3) Fingering 3 Flow, (LR) Low Rotation Transition, (BF) Band Formation, (HR) High Rotation Transition, (DG) Discontinuous Axial Gradient, & (CD) Centrifugal Dominance.

Figure 4.1: End View Image Composites



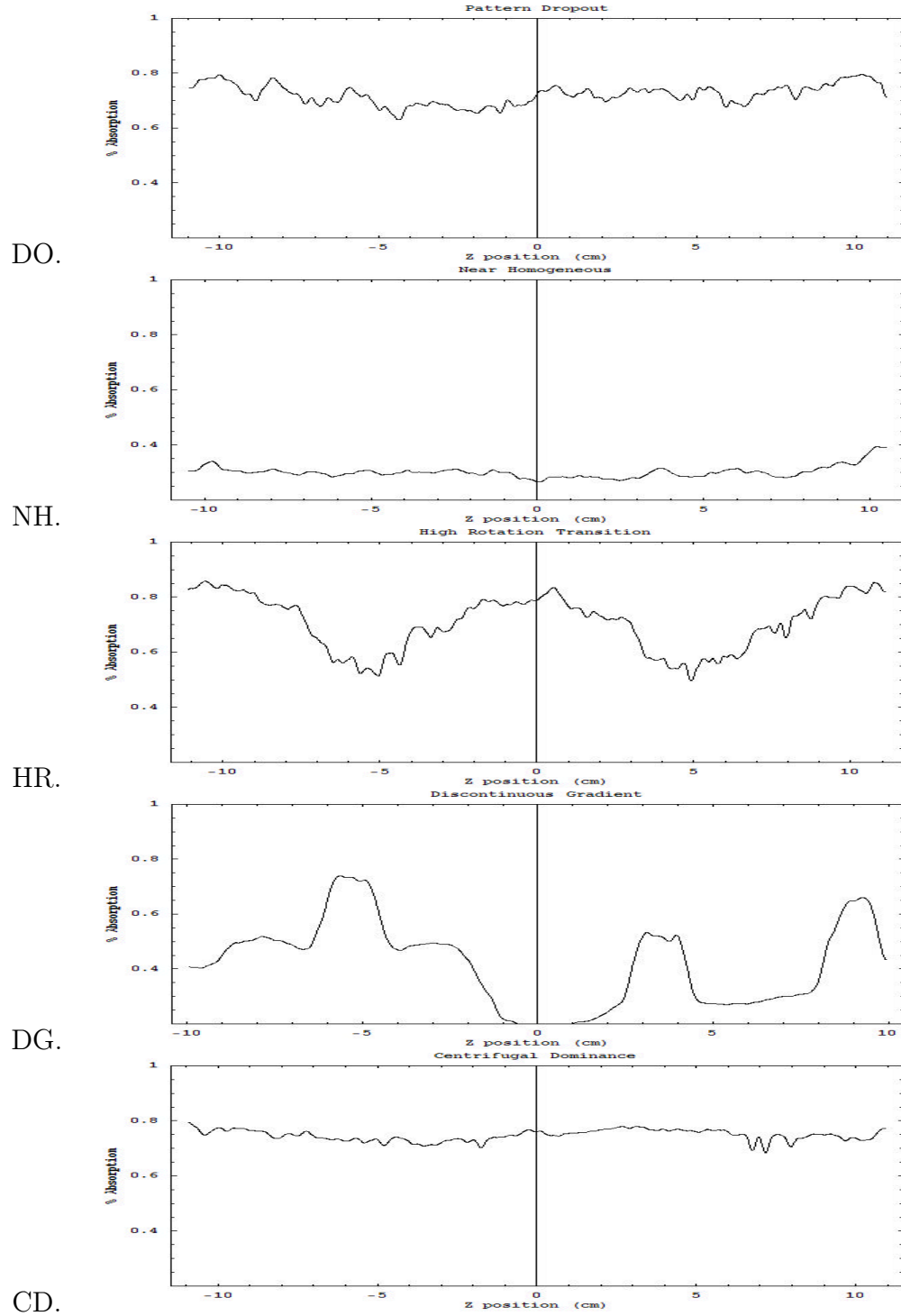
Particles are shown as black on white background. Heavier particle concentrations result in higher absorption and darker color. Phases shown are: (GB) Granular Bed Flow, (F2) Fingering 2 Flow, (F3) Fingering 3 Flow, (LR) Low Rotation Transition, (BF) Band Formation, (DO) Pattern Dropout, (NH) Near Homogeneous Concentration, (HR) High Rotation Transition, (DG) Discontinuous Axial Gradient, & (CD) Centrifugal Force Dominance phases.

Figure 4.2: Front view light transmission still shots



Optical absorption plots using column averaged intensity over the cylinder diameter and corrected for background. Heavier particle concentrations result in higher absorption. Phases shown are: (GB) Granular Bed Flow, (F2) Fingering 2 Flow, (F3) Fingering 3 Flow, (LR) Low Rotation Transition, and (BF) Band Formation.

Figure 4.3: Front view Absorption Plots



Optical absorption plots using column averaged intensity over the cylinder diameter and corrected for background. Heavier particle concentrations result in higher absorption. Phases shown are: (DO) Pattern Dropout, (NH) Near Homogeneous Concentration, (HR) High Rotation Transition, (DG) Discontinuous Axial Gradient, & (CD) Centrifugal Force Dominance phases.

Figure 4.4: Front view Absorption Plots

cylinder rotation, Region B in Figure 4.5(GB)) is centered near the base of the granular bed. The bulk of the fluid is co-rotating (same direction as the cylinder rotation, Region A in Figure 4.5(GB)) and encompasses the break-away point of the particles. This flow into the granular bed encourages the particles to remain in or near the granular bed.

Comparison of Figures 4.1(GB) and (F2) illustrates the two qualitative differences essential to identify this state and differentiate it from the others. Particles are almost completely contained in the granular bed region. Those traveling near the granular bed are moving with a velocity comparable to that of the bed itself and typically join the bed in a relatively short period of time.

4.3 (F2) Fingering with 2 Flows

The system exhibits two types of fingering flows. The first type divides the cylindrical cross-section into a counter-rotating region near the bed (Region B in Figure 4.5(F2)) and a co-rotating region opposite the bed (Region A in Figure 4.5(F2)). These two regions (hence "2 Flows") are separated by a narrow region that divides the r - θ plane roughly in half and behaves like a potential ridge. Particles approach this ridge and are swept into parallel velocity vectors on each side of the ridge, as if a high potential exists along the dividing line. Figure 4.1(F2) clearly shows the parallel velocities along the ridge dividing the two regions. Boundary violation is restricted to a region near the top of the granular bed. This region has similar shape and behavior to a saddle point where some particles are able to cross over but most are deflected back.

Fingers start as collections of two or three beads positioned loosely behind each other, and grow into chains several millimeters long but only a few particle diameters wide. Close observation of the beads at the upper end of the granular bed reveals fingers are formed when a particular particle begins to fall and draws in one or more neighboring particles. The effective range of the hydrodynamic interaction is approximately 5 particle diameters. As a group, the finger velocity can exceed that of the surrounding particles and the bed by a significant amount[21]. The velocity

gradients demonstrated by the fingers increases with the rotation rate, ω , as the fingers increase in both mass and size. Particles within the fingers appear distributed about the central fall line approximately three to four radii apart (center to center).

The fingers occur at quasi-periodic and rotationally dependent time intervals giving the velocity field time dependence. The fingers are also periodic axially, occurring with a spacing proportional to their own width. At low rotation rates, the spacing between fingers is comparable to the finger width, only 2-3 particle diameters wide. At higher rotation rates (larger ω), the spacing increases to several millimeters while the fingers remain narrow by comparison.

It is interesting to note the fingers follow the bed as they fall, keeping their radial position, r , constant until they near the base of the granular bed. It should also be noted, the particles remain within the illuminating light sheet for their entire journey, indicating the two-dimensional behavior of the falling particles since $v_z = 0$.

4.4 (F3) Fingering with 3 Flows

Figure 4.1(F3) illustrates a third circulation region (hence "3 Flows") at the base of the granular bed. The co-rotational region opposite the granular bed, region D in Figure 4.5(F3), is now parabolic, and particles in this region make a single orbit before returning to the granular bed regions (B and C). The co-rotating region near the base of the granular bed, C, exhibits closed orbits in which particles can remain suspended for many rotations. Particles in the counter-rotating region, B, also exhibit closed orbits and can remain suspended for many rotations. Close observation of the bead-fluid interface separating regions B and C from region D reveals an extremely sharp boundary between heavily populated and nearly void solution.

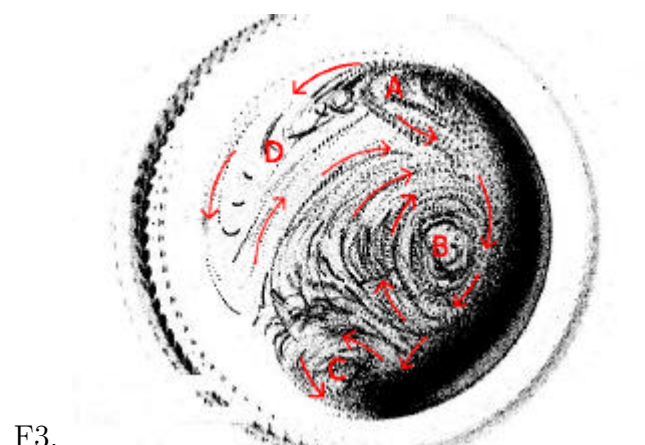
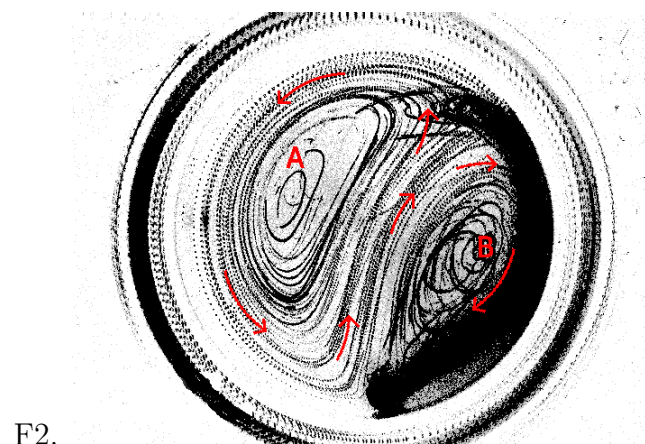
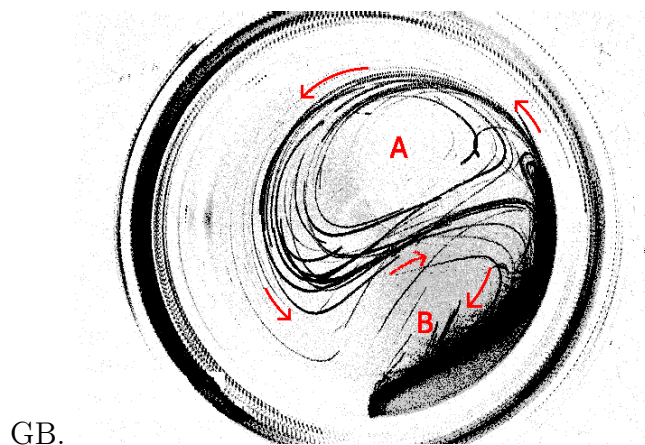
Figure 4.5(F3) illustrates the path traveled by a given *finger*. Finger formations start at position A, at which the parabolic (D) and counter-rotation (B) regions meet. They travel parallel to the bed around region B until the velocities turn away from the granular bed. At this point, part of the finger mass is absorbed by the bed and part is sent toward the center of the cell. When the mass sent inward approaches the bead-fluid interface, the mass is distributed between the co-rotating (C) and counter-

rotating (B) regions. The bead-fluid interface is not disturbed by this approaching mass. When viewed using the short cell, both the suspended particles and those constituting the fingers remain within the illuminating light sheet throughout their journey, again indicating the two-dimensional behavior of this phase. The absorption plot in Figure 4.3(F3) is able to capture the fingering behavior as somewhat regularly spaced wedge-shaped ripples.

4.5 (LR) Low Rotation Transition - The Start of 3-D Flow

The system produces two *transition phases* which differ qualitatively from other phases. The *granular bed* phase does not significantly change with rotation rate. It may cover more or less area on the wall, but its behavior and relative shape remain unchanged throughout the phase region. Similarly, the two fingering phases each generate various numbers and sizes of fingers based on the choice of $\{\mu, T\}$ within the phase region, but they are still two-dimensional structures of similar shape and behavior. The final appearance and behavior of a *transition phase*, however, is strongly dependent on the choice of $\{\mu, T\}$ within the region of phase space, as demonstrated by Figure 4.8. Near the lower rotation rate boundary, in this case **fingering 3-flow**, the system will demonstrate significant "fingering" behavior. As the system is moved closer to the upper (larger ω) boundary, the low speed (fingering) behavior diminishes and the behavior of the next phase, in this case **band formation**, becomes dominant, and the system exhibits considerable "band-like" appearance, which will be described in detail later in this paper.

The onset of the **low rotation transition** phase is characterized by a non-zero v_z component in the fingering velocity, hence the onset of three-dimensional flow. In the r - θ plane, this transition is observed by a change in the internal flow structure, as shown in Figure 4.8(A). The two-dimensional fingers are constrained to fall within a well defined channel created by the counter-flow near the bed. This channel can be seen in Figure 4.1(F3) along the right side of region B. The fingers become three-dimensional when they have the ability to fall toward the center of rotation, thus



Particles are shown as black on white background. Red arrows indicate the flow direction.

Figure 4.5: Flow Paths

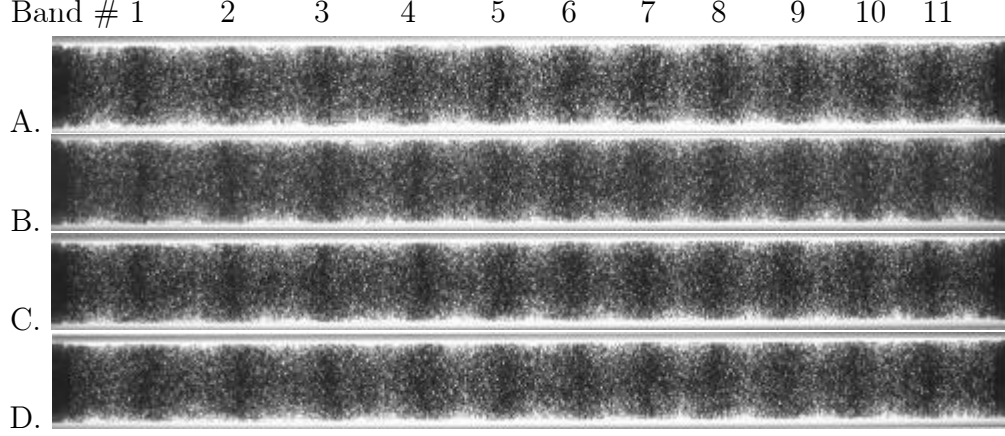
changing their radial position, r , during the fall.

Beyond a certain rotation rate, the fingers fall with the downward moving wall of the cell, as shown in Figure 4.8(B). Once this occurs, the granular bed is quickly destroyed and all particles become suspended. This is a consequence of positive feedback as the fingers are now able to reinforce the lifting of the rising wall. A small outer layer of order surrounding an inner region of fluctuation can be seen in Figures 4.1(LR) and 4.8(B). From the front view in Figure 4.2(LR), the concentration profile resembles Figure 4.2(BF). The "band-like" structures fluctuate periodically in time as a consequence of the unstable central region. The *unstable bands* oscillate between left and right favoring structures in a loosely periodic time frame. Figure 4.6 shows four successive pictures of the system at the same rotation rate and temperature. Careful comparison between them reveals the instability of each individual structure. For example, Band #3 is leaning to the right in image A and to the left in image D. Similarly, Band #4 is leaning to the left in images A and C, but to the right in images B and D. The period of the oscillation increases with rotation rate, ω , from a few seconds at initial onset (smaller ω) to approximately one minute near the upper (larger ω) boundary. The period also increases with the solution viscosity as the drag force slows everything down; however, the general behavior and oscillatory pattern remains unchanged. Figure 4.7 compares the sequence in Figure 4.6, but is unable to detect the instability in the concentration line. A more complex detection algorithm is necessary to detect this behavior.

4.6 (BF) Band Formation

Bands are structurally indistinguishable, being symmetric about their maximum concentration line, time independent in behavior, and isolated from their neighbors in flow pattern. Although their flows may touch at the edges, the particles exhibit parallel velocities and the structures do not share mass. The line of maximum concentration, defined in Figure 4.9, is vertical and stationary.

The velocities field within a band is observed to be parallel to the population line defined in Figure 4.9. The velocity field is symmetric about the line of maximal



Side by side comparison of the Low Rotation Transition phase. Note changes in band orientation of a specific band between successive images, eg. band 3 leans right in A and left in D. Images are taken several seconds apart using identical camera settings.

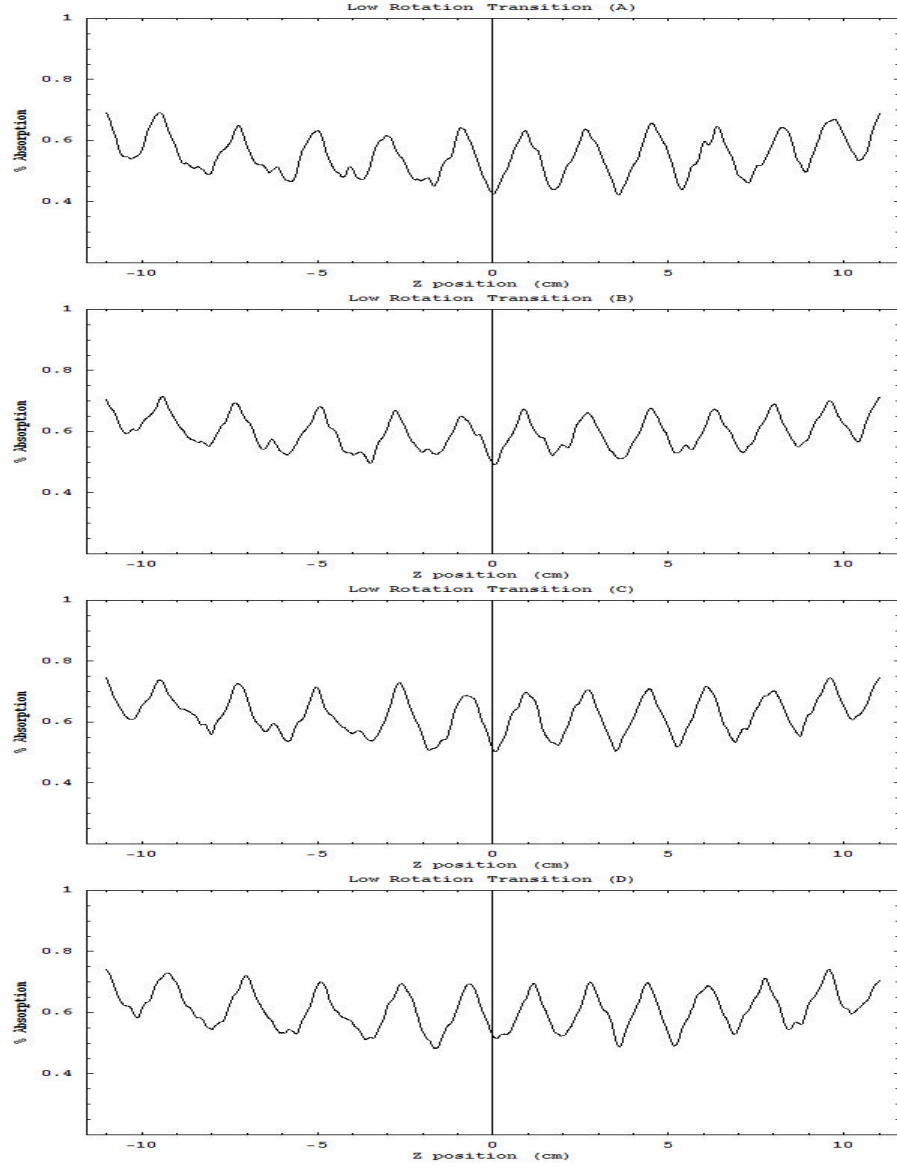
Figure 4.6: Low Rotation Transition Comparisons

concentration. Each side spins on its own axis but with the same angular velocity. The average band spacing is $\lambda_{mean} \approx 2.2cm$. The band angle ratio, as defined in Figure 4.9, and the normalized band spacing can be calculated.

$$\theta = Tan^{-1}\left(\frac{1.91cm}{1.1cm}\right) \approx 60^{\circ} \quad (4.1)$$

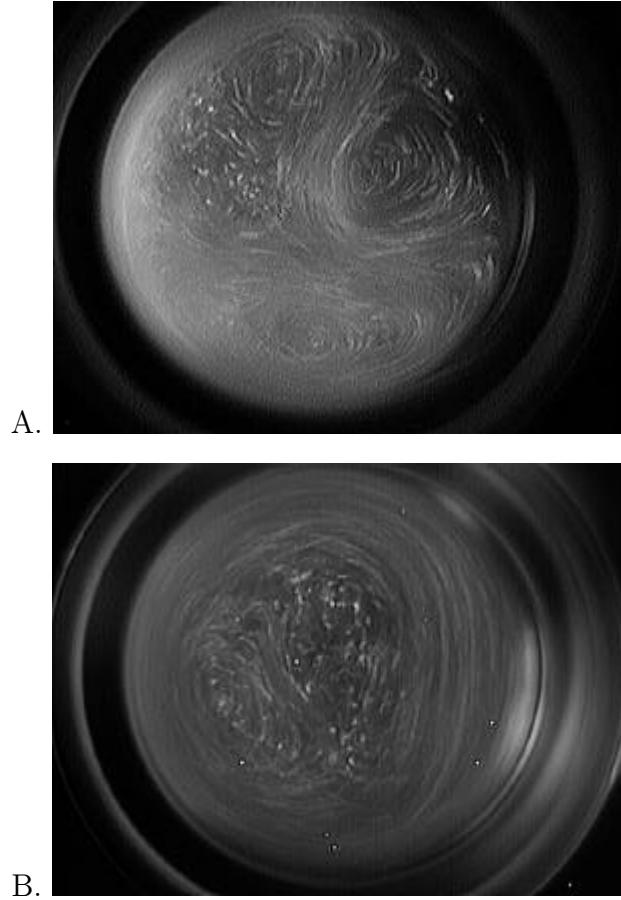
$$\lambda_0 = \frac{avgsize}{tubeID} = \frac{2.12cm}{1.91cm} \approx 1.11 \quad (4.2)$$

The average band size is independent of viscosity, rotation rate, and cylinder length. Table 4.1 shows the measured band spacing over a range of viscosities. I have varied the tube lengths from $1.25cm$ to $28.0cm$ and found the tube length affects the number of bands present in the system (nearest half-integer). Particle size is changed by a factor of 2 without a measurable change in band spacing, and particle volume fraction is varied from 1.1 to 2.6 and I did not find a measurable change. The only physical parameter that changes the band spacing is tube diameter. Details of these studies will be discussed Chapter 5.



Side by side comparison of the Low Rotation Transition absorption plots. The changes in band orientation are not visible in these plots.

Figure 4.7: Low Rotation Transition Comparisons



In figure A the bed still exists. In this case, the Low Rotation Transition still resembles the fingering phases, but the flow is clearly three-dimensional. In figure B, the granular bed no longer exists. A closed loop of order surrounds inner region of fluctuation. In this case, the Low Rotation Transition resembles Band Formation, but the inner unstable region prevents temporal stability.

Figure 4.8: Low Rotation Transition with and without the granular bed

Statistic	λ (cm)	λ (cm)	λ (cm)	λ (cm)	λ (cm)
53cp	(1.350)	2.175	2.100	2.075	2.050
53cp	2.200	2.275	2.300	2.450	
53cp	2.400	1.975			
37cp	(1.150)	2.050	2.150	2.100	2.250
37cp	2.200	2.300	2.300	2.400	
37cp	2.300	2.100			
30cp	(1.050)	2.150	2.300	2.450	2.450
30cp	2.400	2.400	2.050	(1.675)	
30cp	2.025	2.300			
19cp	(1.350)	2.200	2.200	2.150	2.150
19cp	2.200	2.300	2.200	2.200	
19cp	2.200	2.100			
Mean	2.22				
Median	2.20				
Std Dev	0.13				

Band spacing measurements at different viscosities. All measurements were taken in the Standard Tube, length 22.75 centimeters. Parenthetical measurements indicate "half-bands" and are thus ignored in the statistics for average band spacing.

Table 4.1: Band Spacing Statistics for the Standard Tube

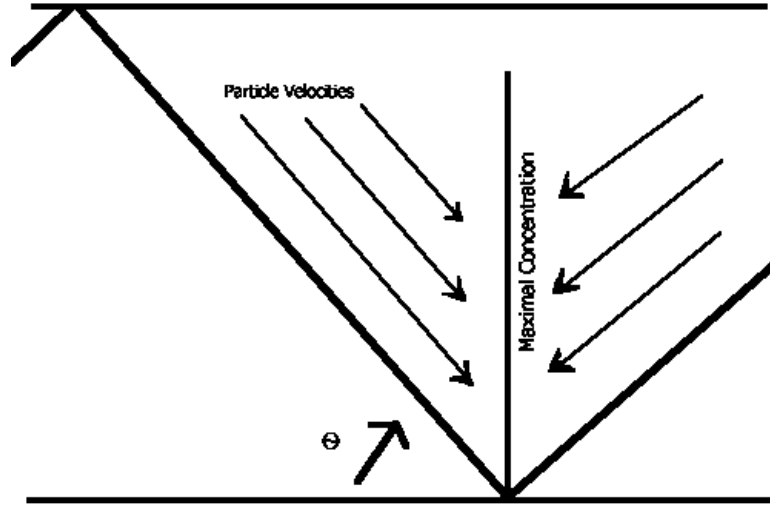


Figure 4.9: Band Angle Geometry

4.7 (DO) Pattern Drop-Out

Above a certain rotation rate, the stable (or unstable) bands cease to exist and are replaced with a region of near homogeneous concentration. The remaining flow patterns continue unabated with little or no adjustment in their axial location. Pattern removal begins at a given location and then spreads from that location along the z -axis in both directions as the rotation rate, ω , increases. The removal of individual structures is a reversible process. Reducing the rotation rate restores any destroyed structures in their original positions.

4.8 (NH) Near Homogeneous Concentration

Under the right conditions, it is possible for all concentration and velocity patterns to fail resulting in Figure 4.2(NH). All secondary flows become negligible leaving a nearly uniform concentration across the entire cylinder with the particle veloc-

ity $\approx r\omega$. The nearly uniform concentration throughout the tube is illustrated in Figure 4.4(NH). This time independent state is extremely sensitive to gravitational influence so an extremely level tube is necessary to prevent gravitationally induced axial stratification. Deviations of less than a tenth of a degree from level will cause a notable concentration gradient along the cylinder length. Ideal conditions have been maintained for several weeks in order to test the *steady state* nature of this phase.

The *phase space* occupied by this phase is extremely small. Viscosities or rotation rates too large or too small destroy the delicate balance of known (and unknown) forces. It can take up to 18 hours to reach steady state, even under ideal conditions. Tight regulation of rotation period and viscosity is required, both on long and short term time scales. The total width of the phase space is less than half a second per rotation at its widest point and only a few centipoise wide in viscosity. Fluctuations outside this region, even for a single rotation, will prevent the phase reaching *steady state*.

4.9 (HR) High Rotation Transition

The **high rotation transition** phase is characterized by a large scale axial concentration gradient. This gradient is constant over several centimeters before reaching a maxima (node) or minima (anti-node). One or more nodes or anti-nodes can be present in the cylinder. Figure 4.2(HR) shows two anti-nodes and three nodes. The selection mechanism for the number and placement of nodes and anti-nodes is not known. Apparatus dependence has been eliminated because the same concentration and velocity patterns have been observed using different equipment and preparations at the same rotation rate and viscosity. Figure 4.4(HR) shows this concentration gradient as a continuous curve in the optical absorption plot. Nodes are indicated by maximal absorption. A continuous decrease in the absorption, corresponding to a decrease in concentration according to the Lambert-Beer Law, is observed over several centimeters before reaching an anti-node. Concentration then begins to increase over several centimeters before reaching the next node, or the end of the cell.

Similar to the low rotation counterpart, the low speed side of the **high rota-**

tion transition phase resembles the **pattern drop-out** phase with a background concentration gradient. Increasing the rotation rate causes the gradients to become larger, and the populated regions shrink into smaller axial regions resembling the **discontinuous axial gradient** phase to be discussed below.

4.10 (DG) Discontinuous Axial Gradient

At higher rotation rates, axial concentration discontinuities develop where the particle concentration comes to an abrupt halt (or start) in the axial (z) direction. *Segregation bands* develop that are up to 1 cylinder diameter wide with their sides orthogonal to the axis of rotation (z -axis). Collectively, these bands contain the entire particle concentration in the cylinder. Particles trapped on the wall are swept into these band-like structures, though this process takes a considerable amount of time: several hours at $\mu = 40cp$. The time to reach steady state for the segregation structures is relatively short: less than 30 minutes at $\mu = 40cp$.

Segregation bands differ from other band structures in both concentration profile and flow. A large node of particles is located around the center of rotation, as seen in Figure 4.1(DG), and a thick layer of particles hovers near the cylinder wall. Between them is a thin sparsely populated region. In some cases, particles are ejected from the node in the center and slowly spiral outward to the wall while moving axially with a small z -velocity. More importantly, the band angle, as defined in Figure 4.9, is $\theta \approx 90^\circ$. Figure 4.4(DG) shows the sharp discontinuity in concentration as abrupt changes in the optical absorption. Note the width of each peak is roughly $1.9cm$, or one cylinder diameter.

High viscosity suspensions tend to develop larger numbers of smaller, poorly formed segregation bands. These bands have a negligible wall concentration and a weak, often imbalanced, central node. This node tends to oscillate about the axis of rotation within the r - θ plane like a mass on a spring and lagging the cylinder wall's angular velocity. Conversely, lower viscosities generate fewer, larger, and better formed bands. Well defined segregation band structures typically occur about every 8 to 10 centimeters, whereas poorly defined band structures in high viscosity suspensions

may occur as often as every 2 to 3 centimeters. In general: the more distinct the segregation bands, the greater the separation between adjacent band structures. The fluid between adjacent structures is void of particles, and the interface between a heavily populated and an unpopulated region is abrupt, or *discontinuous*.

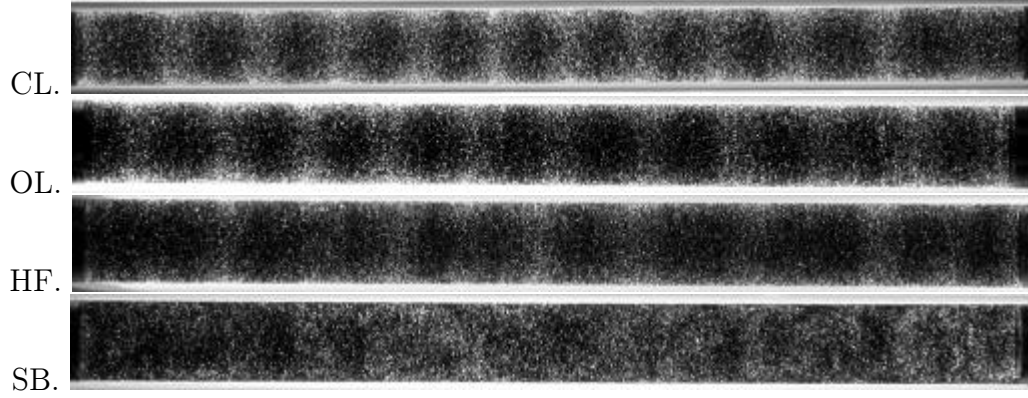
Segregation band structures are generally time independent, though some may have periodic mass fluctuations as discussed earlier. For a given rotation rate, the structures form at prescribed, fixed locations; however, changing the rotation rate slightly will cause these structures to move axially and reposition themselves. They will again become axially fixed in their new location for as long as the conditions remain constant.

4.11 (CD) Centrifugal Force Dominance

The upper limit of the phase diagram is the classical limit where all particles spin out to the wall under the influence of the imaginary centrifugal force. Given time, all patterns present on the cylinder wall break down and generate a uniform coating layer using the available material. The volume fractions used in the present study provide insufficient material to coat the entire inner wall which results in one or more single layer patches of particles.

The onset of this phase is one of the sharpest transitions described in this paper. As mentioned previously, the rotational period resolution is 0.025 seconds per rotation. The transition from **discontinuous axial gradient** to **centrifugal force dominance** occurs within this fine adjustment and is completely reversible with the same adjustment. In other words, a change of 0.025 seconds per rotation will cause everything to spin out to the wall. Going back to the previous setting will recreate the segregation bands in exactly the same axial positions even after allowing the system to reach a uniform coating. Since the positioning of the segregation band structures has been identified as rotation rate dependent, this repeatability in axial positioning is very interesting.

When slowing the tube down, the uniform coating on the wall develops an instability such that particles along the wall collect in an axial line prior to segregation



Higher particle concentrations result in higher absorption and darker color. States shown are: (CL) Concentration Line Thickening, (OL) Outer Layer Development, (HF) High Frequency Structures, and (SB) Segregation Band Structures.

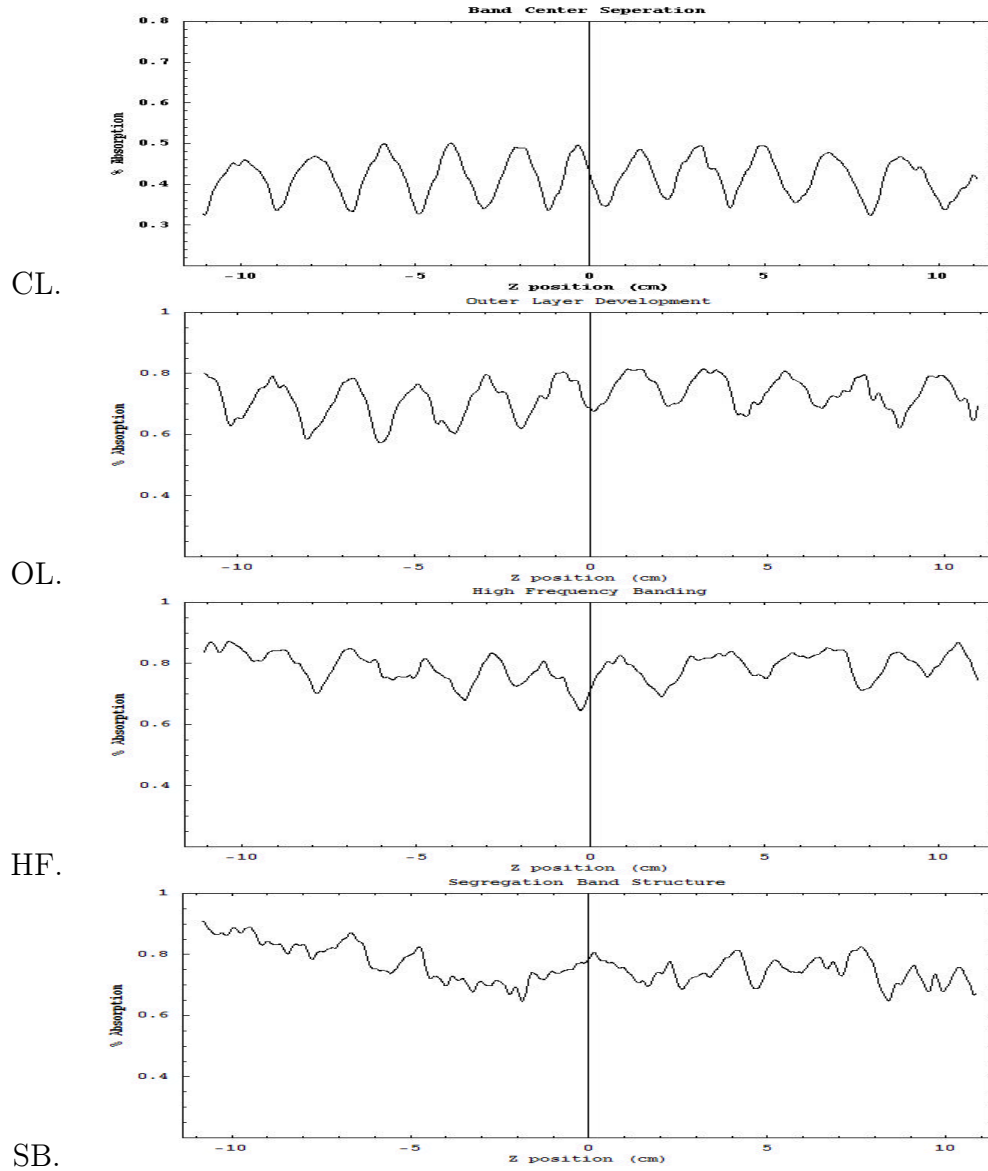
Figure 4.10: Front views of coexistent states

band onset. The line of particles bends and forms a sinusoidal wave pattern along the length of the cylinder. It is believed that this instability may be associated with the onset of segregation bands since the pattern develops if the cylinder rotation rate is approximately but slightly faster than **centrifugal force dominance** onset. A discussion and brief study is performed by Breu *et al.*[17] using water and 300 micron beads of comparable density to those in this thesis. It is suggested therein that these wave patterns are caused by the bouncing of the beads against the wall. They note that below a certain rotation rate the beads collected at one end, hence **discontinuous axial gradient** and segregation band structures. Their period of rotation agrees well with the boundary predictions presented in this thesis at $\mu = 1\text{cp}$.

4.12 Coexistent States

4.12.1 General Concepts

Unlike the *phases* discussed above, the *coexistent states* which follow do not exist independently. These *states* can coexist with the previously discussed *phases* and other *coexistent states*. These *states* are believed to be fundamentally important to understanding this system.



Optical absorption plots using column averaged intensity over the cylinder diameter and corrected for background. Higher particle concentrations result in higher absorption. States shown are: (CL) Concentration Line Thickening, (OL) Outer Layer Development, (HF) High Frequency Structures, and (SB) Segregation Band Structures.

Figure 4.11: Coexistent State Absorption Plots

By definition, *coexistent states* are not completely destructive to the underlying *phase*, but they can impede the development and clarity of the observed *phase*. These patterns have their own *onset boundaries* and reach *steady state*, as defined earlier in this thesis.

4.12.2 (CL) Concentration Line Thickening

Onset of this mechanism causes the line of maximal concentration defined in Figure 4.9 to spread axially, becoming thicker. This can occur in bands, stable or unstable, or fingers. The appearance of the underlying phase remains unchanged within the current limits of observation. Initially, the central region concentration is comparable to that of the overall structure. As rotation rate, ω , increases, the sides move apart. When the central concentration reaches a maximum width, the central concentration begins to decrease as the structure starts to bifurcate.

4.12.3 (OL) Outer Layer Development

Onset of this mechanism generates a layer of uniform concentration near the cylinder wall, $R > r > r_L$. Figure 4.12 shows such an outer layer approximately $\frac{R}{4}$ thick. The underlying phase continues to operate inside this outer layer, $r < r_L$. This outer layer is independent of axial (z-axis) location or angular (θ -axis) location, evidencing itself as a *uniform shell* coating the inner wall, but not the cylinder end caps.

Visual observation suggests a possible correlation with this outer layer and some kind of boundary layer phenomena. Detailed measurements of the outer layer thickness over a range of ω may evidence a possible correlation to some power law behavior and give credibility to this suggestion. At present, however, only crude measurements are available. A plot of the outer layer thickness as a function of ω is shown in Figure 4.13. The solid line is the following exponential equation:

$$Thickness = A(1 - e^{-5(\omega - \omega_0)})$$

where ω_0 is the onset rotation rate for the coexistent state and A is a fitting amplitude.

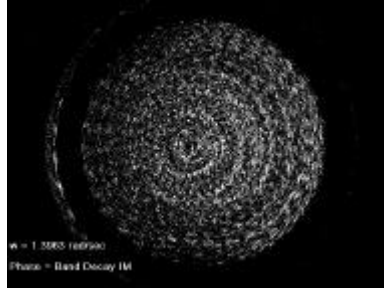


Figure 4.12: Outer Layer Development

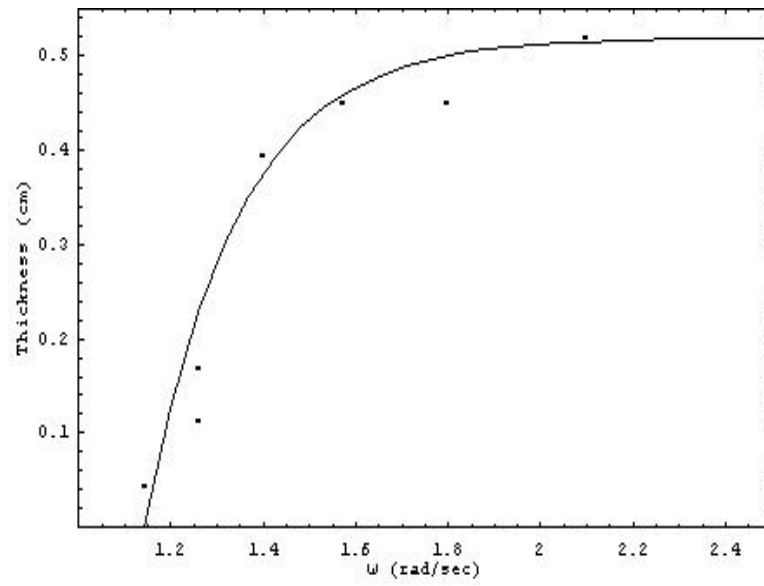


Figure 4.13: Outer Layer Thickness versus Rotation Rate

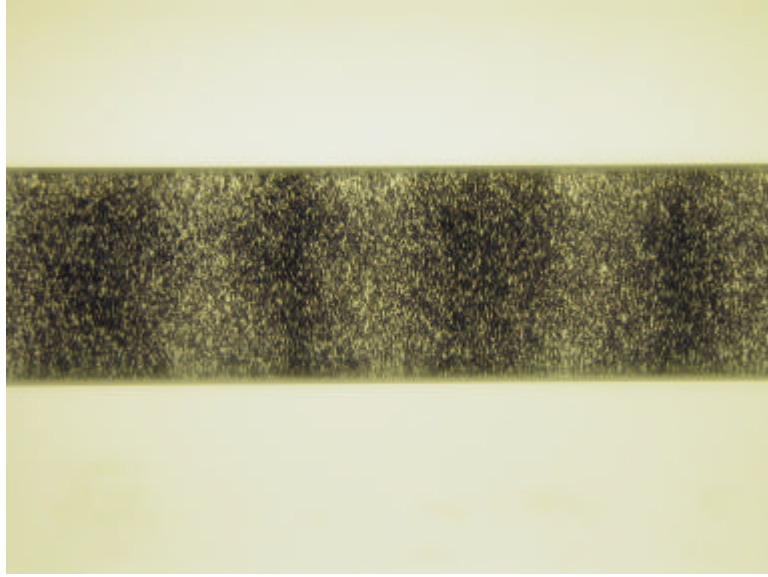


Figure 4.14: High Frequency with Center Line Thickening

4.12.4 (HF) High Frequency Structures

Bifurcation of concentration structures can become complete. When this occurs, what once constituted a single structure becomes two independent structures. The new wavelength is approximately half the original wavelength ($\lambda_{HF} \approx \frac{1}{2}\lambda_{BF}$), thus the term *high frequency* is adopted for these structures ($f_{HF} \approx 2f_{BF}$). The smaller flow patterns are still in possession of a significant axial component. It is not necessary for all structures to bifurcate at the same time. The absorption plot in Figure 4.11(HF) shows the irregularity of the bifurcated band structures, and the new wavelength is $\lambda_{HF} \approx 1.1cm$.

4.12.5 (SB) Segregation Band Structures

Segregation band structures can develop within the background flow field. These structures appear similar to those presented under **discontinuous gradient**, but the mass circulations are not isolated from neighboring structures or the background flow. Individual structures routinely share mass which differentiates these structures from other phases or coexistent states; furthermore, the overall concentration field can still be continuous.

4.13 Transition Boundaries

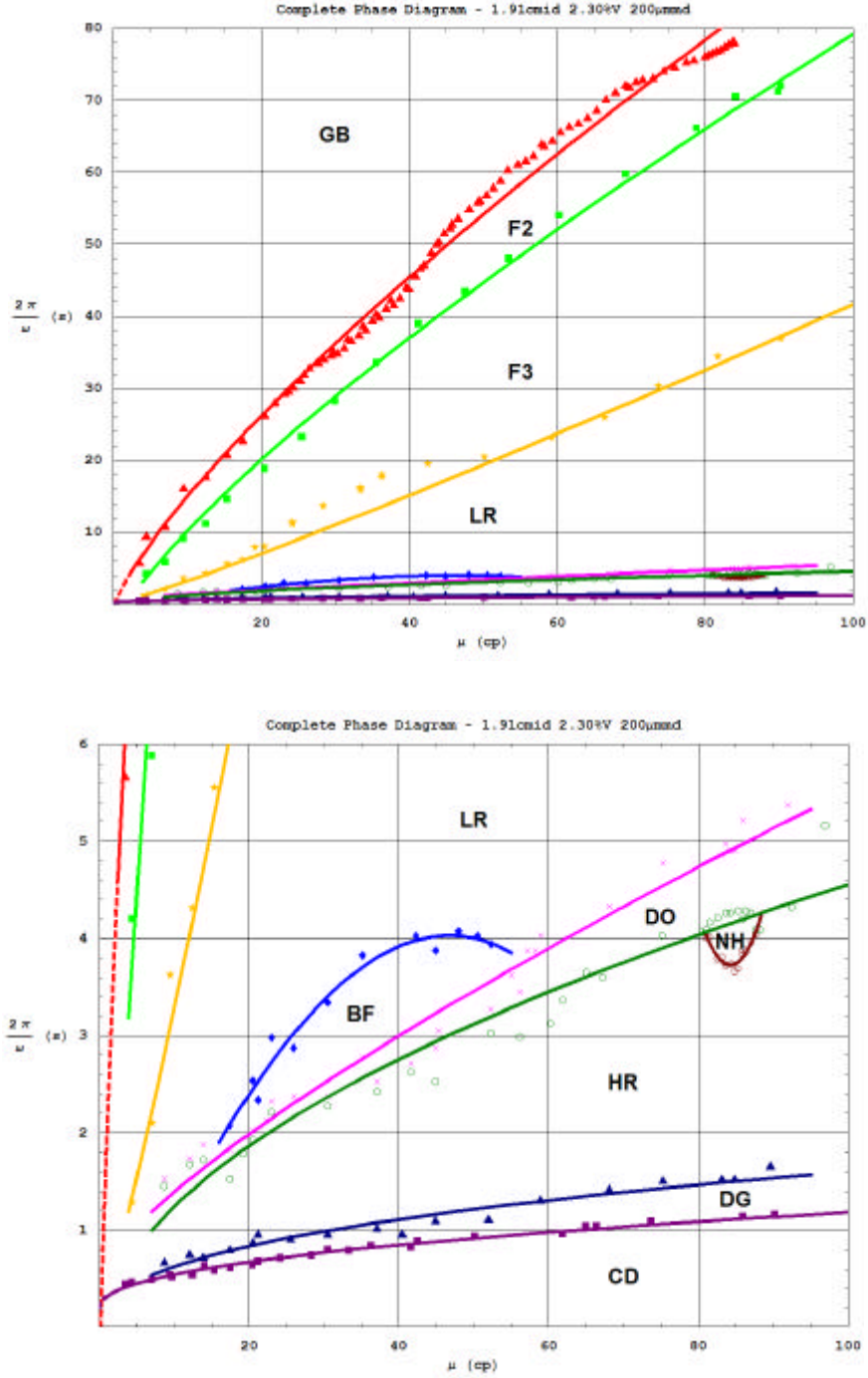
The measurements described in this work define specific regions of phase space for the phases and states detailed in this chapter. A *Transition Boundary* exists between adjacent phases. General nomenclature for defining a Transition Boundary will use the Initial and Final state abbreviations in order of rotation period increase. For example, the GbF2 Boundary refers to the boundary between the Granular Bed (GB) phase and the Fingering Two-Flow (F2) phase.

Some boundaries are seen to take precedence over others, where those of lower rank terminate at the intersection of the boundaries and the encapsulated phase ceases to be observed. A primary example of this behavior is the Band Formation phase. In Figure 4.15 one observes this phase only exists between two intersecting points with the Pattern Dropout phase. Another example is the Near Homogeneous phase which intersects with the High Rotation Transition phase.

Figure 4.15 shows the raw transition boundary data for the Standard System. Careful examination of the data shows that the diagram can be divided into three sections: Low rotation rate, power-law behavior; High rotation rate, power-law behavior; and Intermediate, complex behavior. The Low Rotation Transition and High Rotation Transition boundaries mark the edges of the intermediate, complex behavior signified by a complicated transition boundary.

Transition boundaries also exist for the coexistent states, though more appropriate terminology might refer to these as *onset boundaries* since they mark the onset of the behavior indicated. Unlike phase boundaries, however, coexistent boundaries do not necessarily mark the end of the preceding state. It is quite common for one to observe High Frequency structures with Outer Layer development and Concentration Line thickening, though each of these develop at different rotation rates and have different viscosity dependence.

Figure 4.16 shows the raw onset boundary data for the coexistent states in the Standard System. Careful examination of the data shows the diagram can be divided into two sections: Low rotation rate, power-law behavior with exponent greater than 1; and High rotation rate, power-law behavior with exponent less than 1.



Phase diagram for the Standard System. The raw data points taken from Chapter 4 are fit with a power-law model from Chapter 5, if possible. Boundaries which do not fit the power-law model, such as the Band Formation and Near Homogeneous boundaries, are fit with generic polynomials.

Figure 4.15: Raw Data Phase Transition Boundaries

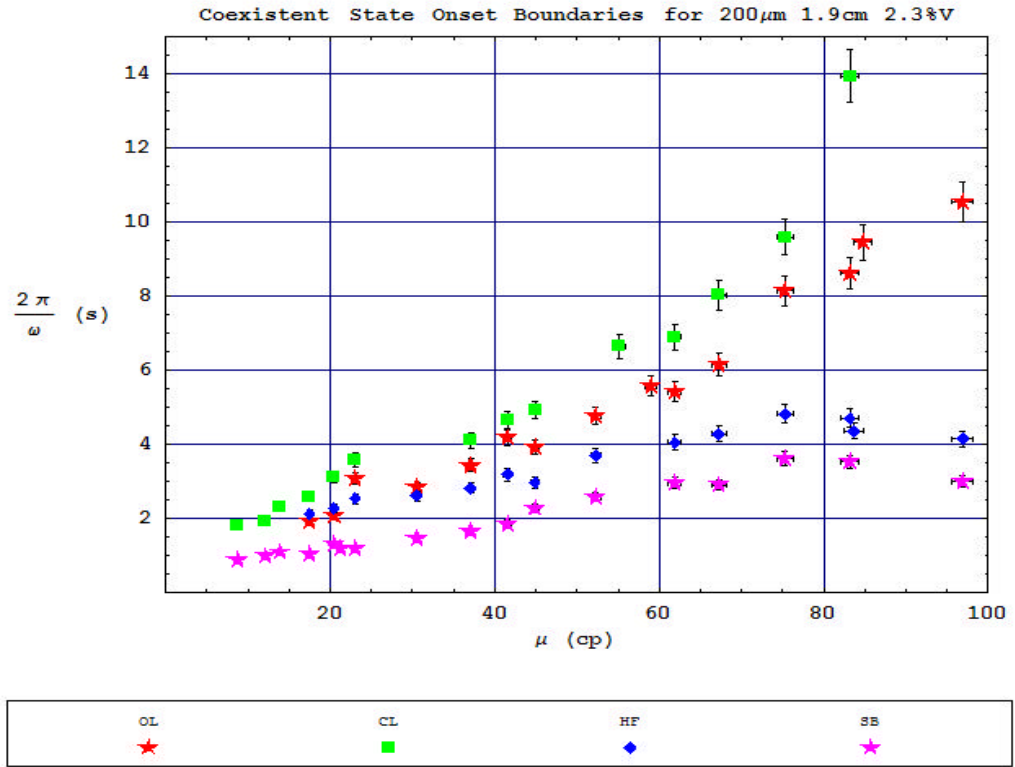


Figure 4.16: Raw Data Coexistent State Onset Boundaries

Chapter 5

Transition Boundary Analysis and Scaling

5.1 General Overview and Nomenclature

It can be argued that the transition boundaries are the result of a shift in the balance of competing forces acting on the system due to a change in the rotation rate or viscosity and, therefore, the relative magnitude or effectiveness of those forces. Close examination of the transition boundaries and how they respond to changes in key experimental parameters may yield insight into the nature of the competing forces responsible for each transition and assist the development of theoretical understanding.

Several questions regarding a transition or onset boundary need to be answered: the nature of the viscosity dependence, response to changes in key parameters, and dimensionless parameters which describe the transition boundaries in Figure 4.15. This chapter will attempt to address these questions for as many transition boundaries as possible. Mathematical analysis of the data presented in Figures 4.15 and 4.16 will address the first question: the relationship between rotation rate, ω , and viscosity, μ . Attempts are made to determine the influence of physical parameters, such as particle size, by scaling the viscosity or rotation period axis for each boundary of the $100\mu m$ system (Figure 5.5) and $3.75cm$ system (Figure 5.6) phase diagrams until they align with the standard system boundaries in Figures 4.15 and 4.16. In each of the new systems, all experimental parameters are kept constant except for particle

size ($100\mu m$ system) or cylinder diameter ($3.75cm$ system). Finally, dimensionless parameters are derived and tested by using the raw data points and experimental parameters to calculate the values along each boundary.

5.2 Power Law Models

It is found that the following standard power law form fits many of the transition boundaries:

$$T = T_0 + \kappa\mu^\Gamma \quad (5.1)$$

Observation of the transition boundaries indicates the rotation period T_0 at $\mu = 0$ is non-zero. This can create errors in the selection of σ and γ in Equation 5.1. To minimize this problem, T_0 is removed by rescaling the data set using the first data point (lowest viscosity) as the origin. We can then approximate the data as follows, assuming μ_1 is small compared to μ_i :

$$(T_i - T_1) \approx \kappa(\mu_i - \mu_1)^\Gamma$$

$$\Delta T \approx \kappa(\Delta\mu)^\Gamma \quad (5.2)$$

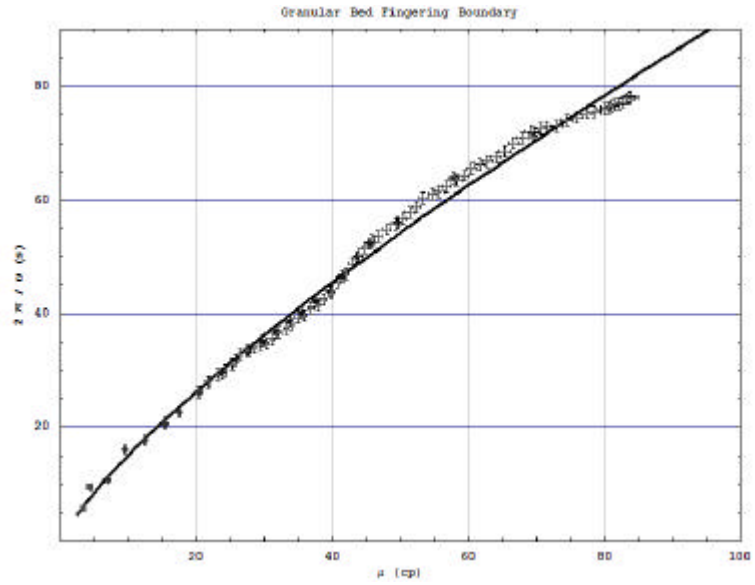
An accurate exponent can now be determined using a log-log plot.

$$\text{Log}(\Delta T) = \text{Log}(\kappa) + \Gamma \text{Log}(\Delta\mu) \quad (5.3)$$

This method provides consistent results for the value of Γ ; however, proper κ and T_0 values should be determined from the complete data set.

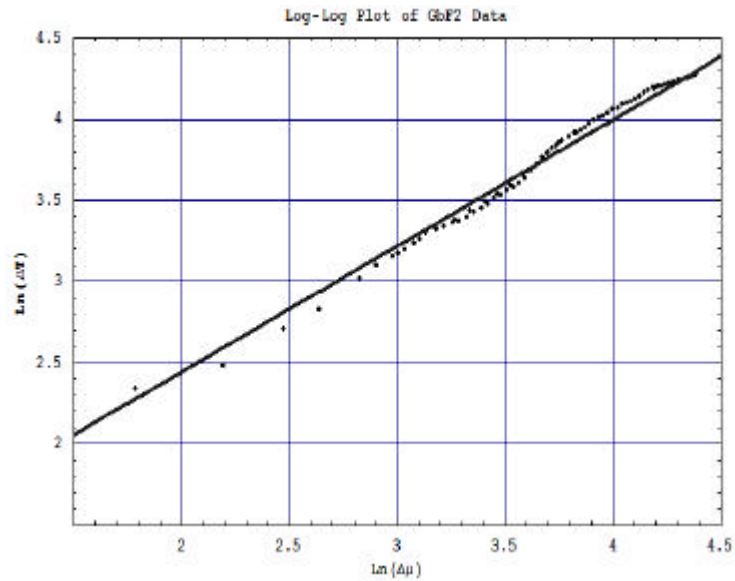
5.2.1 GbF2 Boundary

Careful mapping of this transition boundary is shown in Figure 5.1. A rescaled Log-Log plot using Equation 5.3 is provided in Figure 5.2. The slope of the resulting line is approximately 0.78 or about $\frac{7}{9}$. Using this exponent, T_0 and κ are approximately $-0.71 \approx \frac{-1}{\sqrt{2}}$ and 2.62, respectively. The line in Figure 5.1 shows the power law behavior captures the major features of the data.



Using the slope of $\frac{7}{9}$, a power law is used to fit the GbF2 Data of the Standard System.

Figure 5.1: Power law fit of GbF2 data



Log-Log plot of the rescaled GbF2 Data. The data is approximately linear, indicating a power-law relationship.

Figure 5.2: Log-Log plot of rescaled GbF2 data

5.2.2 DgCd Boundary

The final transition boundary is one where at least something is known. If one spins the cylinder fast enough, everything inside must go to and remain on the inner wall. This material is covered in detail in most introductory physics courses. Correspondence indicates there must be an agreement in the limiting case here. Since the Newton derivation does not include viscous forces (or, in fact, any forces other than gravity), the limiting case must be where $\mu \rightarrow 0$.

The data shown in Figure 5.3 for this boundary resembles that of a power law. Newton's Law states that Centrifugal Dominance should occur when

$$\omega^2 R \geq g$$

or

$$T^2 \leq \frac{(2\pi)^2 R}{g}$$

$$T \leq 2\pi \sqrt{\frac{R}{g}} \tag{5.4}$$

Taking the equality here, that gives a critical value of $T_0 = 0.196$ for the Standard System. A power-law exponent of $0.45 \approx \frac{1}{2}$ is determined with $\kappa \approx 0.123$ or approximately $\frac{1}{8}$. The result is the curve shown in Figure 5.4.

5.2.3 Power Law Results

The above methodology is used to describe the transition boundaries in the phase diagrams shown in Figure 4.15 in real, physical phase space, $\{\mu, t\}$. Some boundaries are clearly **not** power-law behavior, for example the F3Lr and LrBf boundaries. These boundaries are estimated using polynomial expressions of sufficient order without regard to physical meaning; however, one cannot disregard the significance of the power-law behavior and its predominance in the phase diagram. Clearly, this is suggestive of some key relationship between viscosity, μ , and rotation rate, $\omega = \frac{2\pi}{T}$. Specific power-law exponents are provided in Table 5.1 for those boundaries which

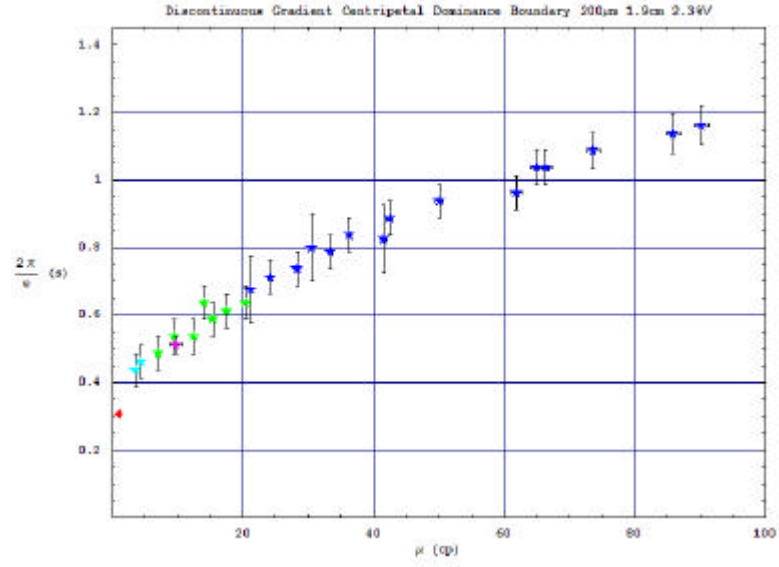


Figure 5.3: DgCd Phase Transition Data for Standard System

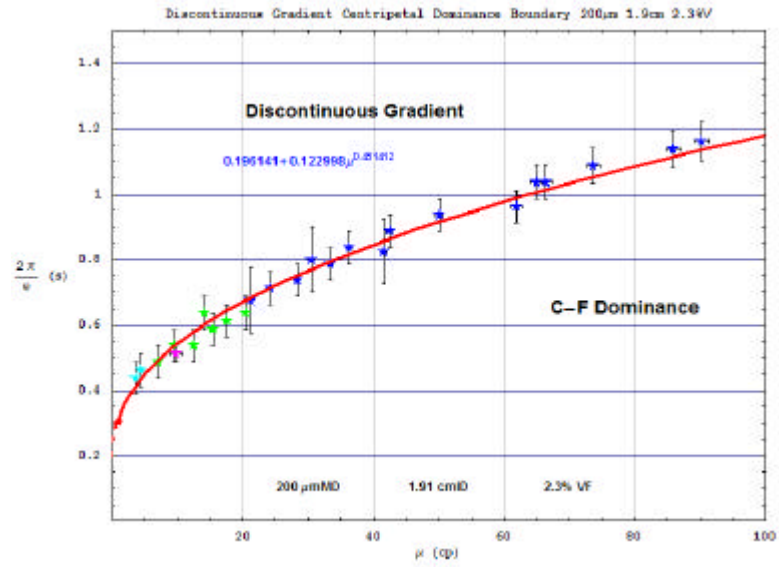


Figure 5.4: DgCd with Newtonian Limit

can be fitted by this type of model. The Coexistent State Onset Boundaries cannot be fitted to the power-law.

Boundary	Intercept	Amplitude	Exponent
GbF2	-0.707	2.619	0.778
F2F3	-3.585	2.304	0.778
LrDo	0.567	0.137	0.778
DoHr	-0.187	0.431	0.521
HrDg	-0.064	0.286	0.382
DgCd	-0.196	0.123	0.451

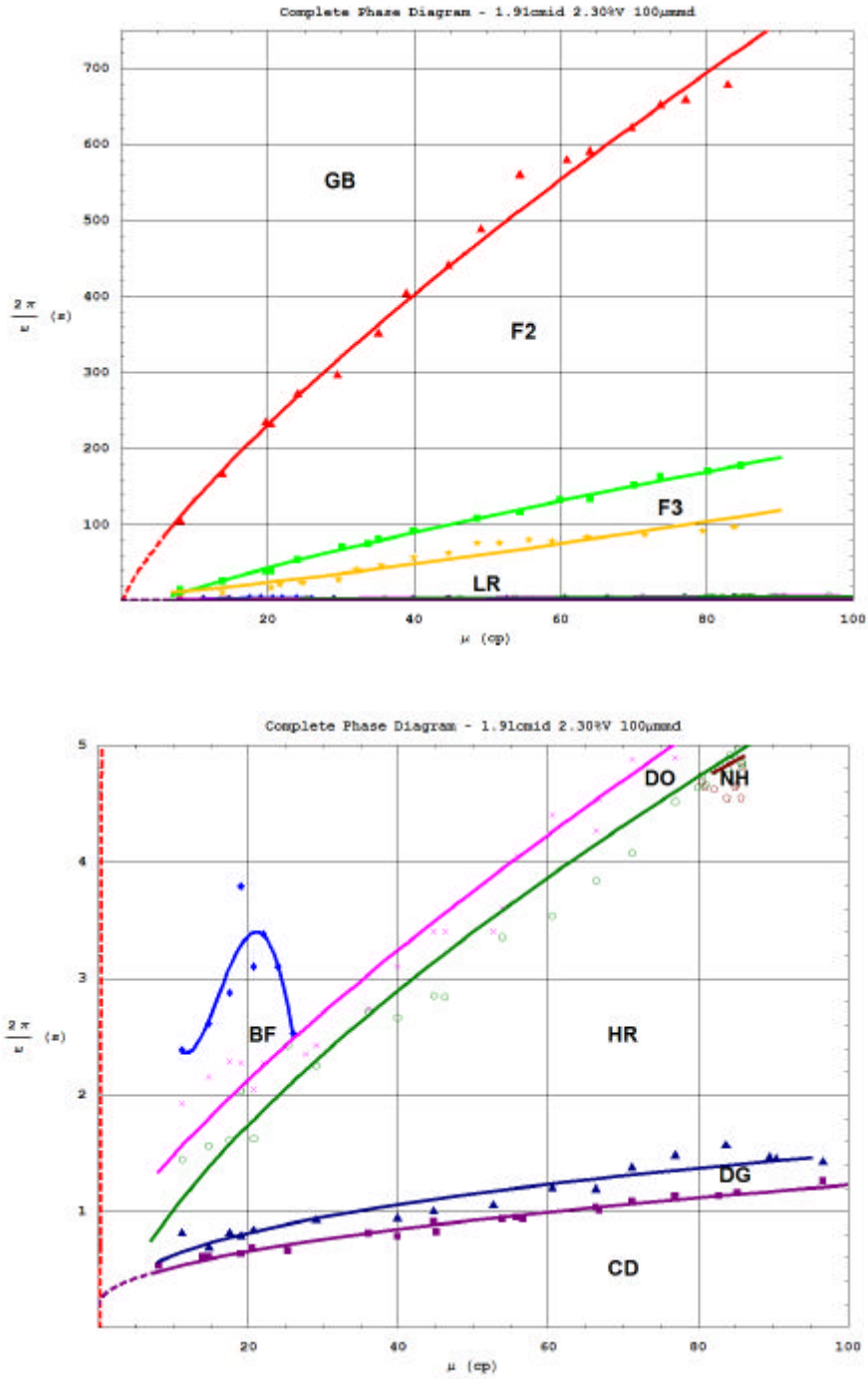
Table 5.1: Values of the Power Law Exponents and Amplitudes

5.3 Direct Plot Analysis

Without an applicable theory, parameter influence can be estimated using direct graphic analysis with the pure (raw) data. Through direct manipulation of the data, the transition boundaries of a new system which has a single parameter changed can be scaled, stretched, or compressed to overlay the transition boundaries of the standard system. The following analysis will scale rotation rates and viscosities for each boundary to examine the influence of particle size and cylinder size on the different transitions and states. To examine particle size influence, transition boundaries were identified for a system using $100\mu m$ particles ($100\mu m$ System). To examine cylinder size influence, transition boundaries were identified for a system with a $3.75cm$ cylinder diameter (375 System).

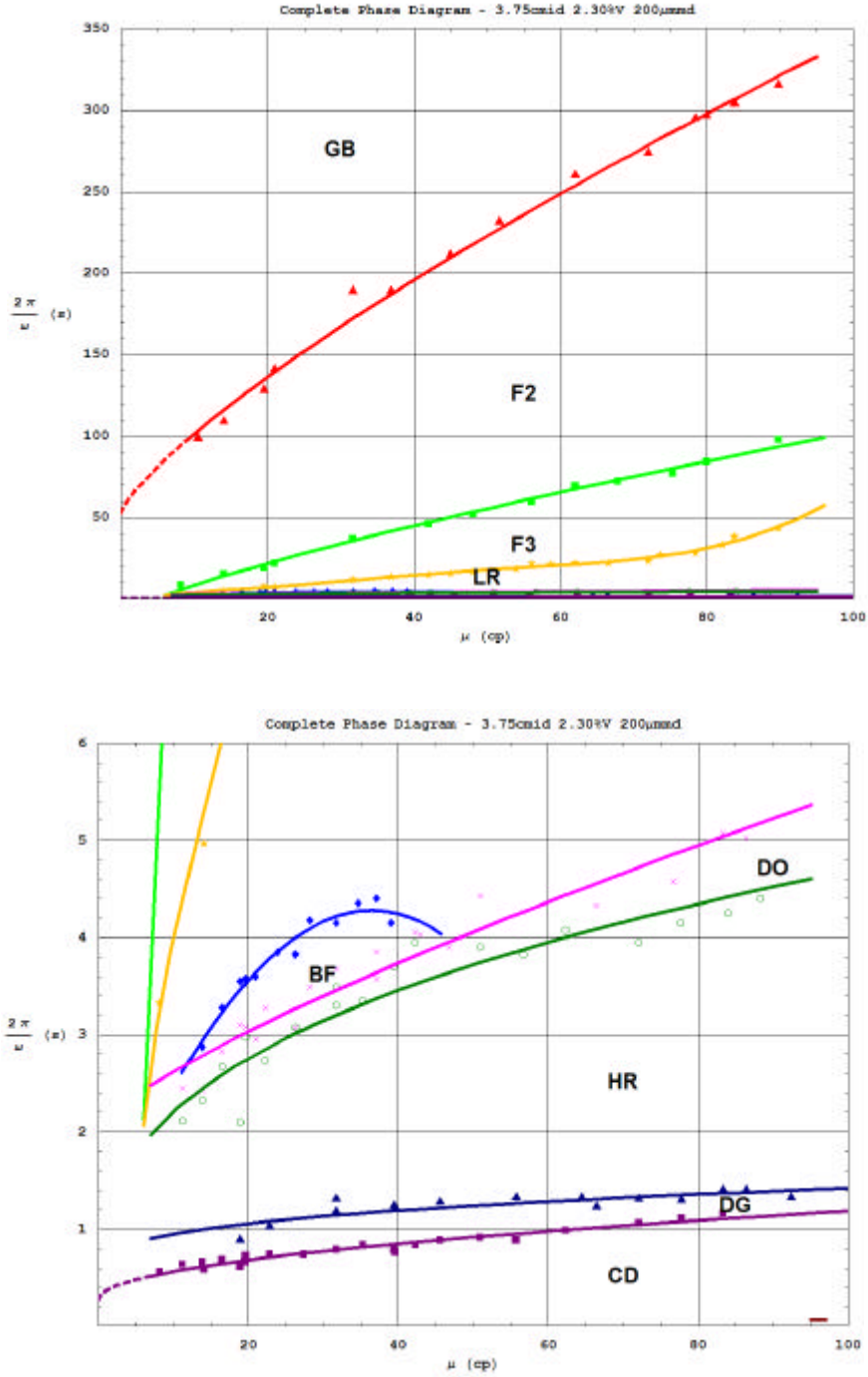
5.3.1 Particle Size Scaling

Reducing the particle size by 50% generally decreased the rotation rate necessary for each transition boundary. The transitions at the lower rotation rates, GbF2 thru F3Lr, were affected the most. Table 5.2 shows the value of γ starts near 10 and drops quickly as rotation rate, ω , is increased. A natural division is evidenced in the γ scaling. The top three values are $\gg 1$, the middle values are $O(1)$, and the two high



Phase diagram for the 100μm System, using particles 100μm diameter. The raw data points are fit with a power-law model, if possible. Boundaries which do not fit the power-law model, such as the Band Formation and Near Homogeneous boundaries, are fit with generic polynomials.

Figure 5.5: Raw Data Phase Transition Boundaries for 100 micron sample



Phase diagram for the 375 System, using a cylinder 3.75cm diameter. The raw data points are fit with a power-law model, if possible. Boundaries which do not fit the power-law model, such as the Band Formation and Near Homogeneous boundaries, are fit with generic polynomials.

Figure 5.6: Raw Data Phase Transition Boundaries for 3.75cm diameter cylinder

speed (rotation rate) boundaries are $= 1$. A similar division can be observed in the σ scaling. Only the onset of transition phases, Low Rotation or High Rotation, or island phases, Band Formation and Near Homogeneous, require viscous scaling.

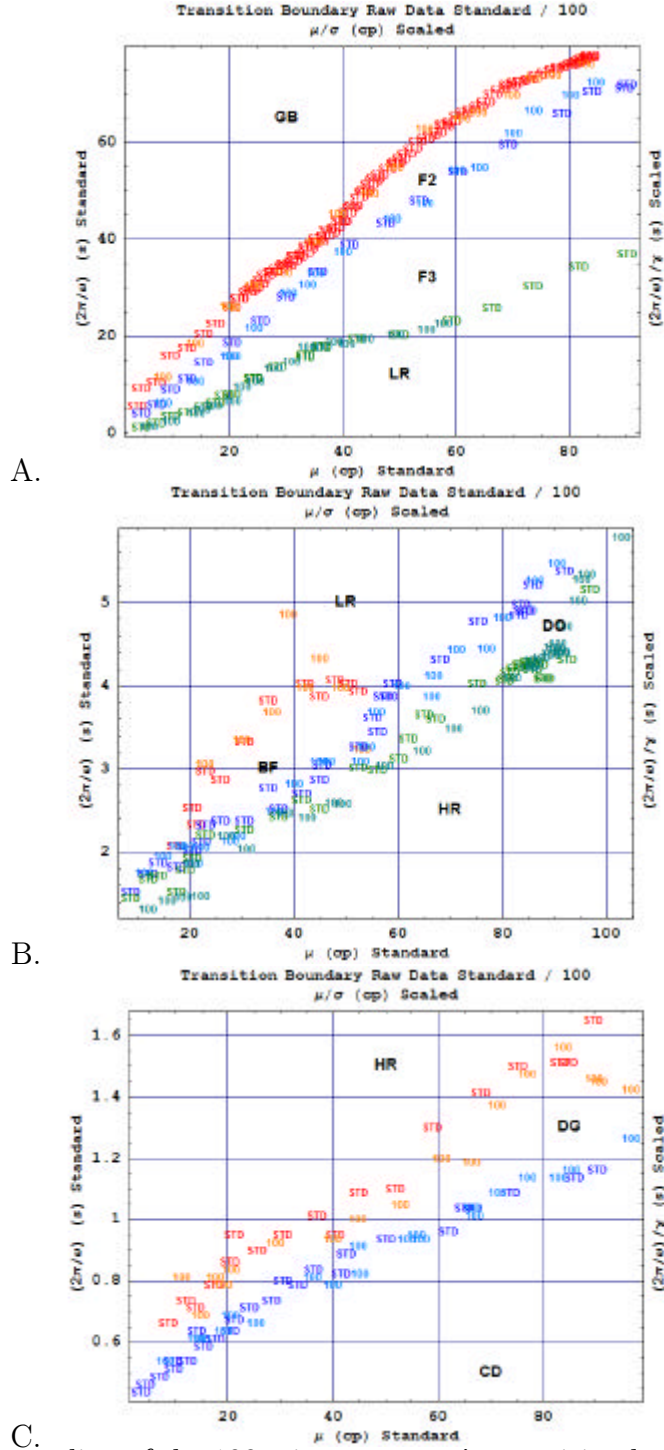
Two transition boundaries are completely independent of particle size, which is a profound observation: HrDg and DgCd. Whatever the forces governing these two transition boundaries, particle size cannot be a factor. Since each transition boundary is governed by a relationship of one or two sets of dimensionless parameters, this observation indicates that forces dependent on particle size, such as particle interactions, cannot be associated with these two transitions. One may note: centrifugal force is *independent* of particle size.

None of the coexistent state onset boundaries require viscous scaling. The temporal scaling, γ , again divides itself naturally. Low rotation behaviors, CL and OL, each require scaling. The high speed behaviors, HF and SB, are independent of particle size. The fact that any of these behaviors would be independent of particle size is surprising and quite unexpected. Clearly these states are related to large scale interactions involving the collective, not the small scale interactions of individual particles.

The Near Homogeneous phase was recovered in the $100\mu m$ system. The rotation rate was slightly slower than in the Standard System, but the viscosity range was almost unchanged. This indicates that smaller particles require smaller rotation rates to achieve near homogeneous mixing.

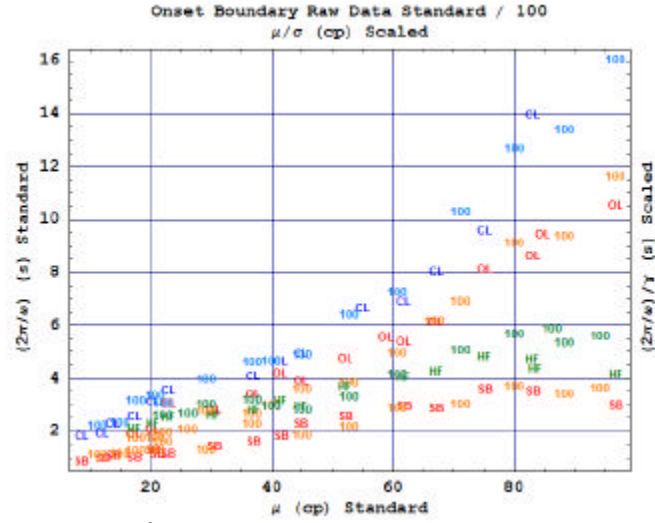
5.3.2 Cylinder Diameter Scaling

Doubling the cylinder diameter generally decreases the rotation rate necessary for each transition boundary. The two transitions at the lowest rotation rate, GbF2 and F2F3, do not require viscous scaling, though the fits are approximate. Additional data would improve the estimate and determine if, in fact, the scaling is accurate. Table 5.2 shows an interesting behavior in γ as the rotation rate, ω , is increased. The behavior of σ , on the other hand, seems regular. On the high speed (rotation rate) side, LrDo to DgCd, the transition boundaries exhibit viscous scaling of ≈ 2 .



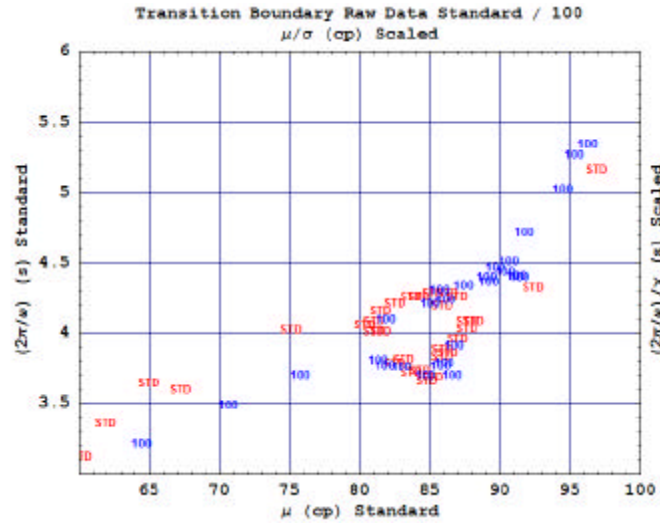
Raw scaling of the 100 micron system's transition boundaries. Each boundary is scaled by the correct σ and γ to overlay the corresponding Standard transition boundary. The values of σ and γ for each boundary is given in Table 5.2.

Figure 5.7: Raw Scaling of 100 micron Boundaries



Raw scaling of the 100 micron system's coexistent state onset boundaries. Each boundary is scaled by the correct σ and γ to overlay the corresponding Standard onset boundary. The value of σ and γ for each boundary is given in Table 5.2. The Standard onset boundaries designate the onset of each coexistent state by the two letter designation defined in Section 4.12.

Figure 5.8: Raw Scaling of 100 micron Coexistant States



Raw scaling of the 100 micron system's Near Homogeneous state boundaries. Each boundary is scaled by the correct σ and γ to overlay the corresponding Standard onset boundary. The values of σ and γ for each boundary is given in Table 5.2.

Figure 5.9: Raw Scaling of 100 micron Coexistent States

At lower rotation rates the viscous scaling is $O(1)$. Further study is warranted to confirm these results and improve the accuracy of the estimates. Not surprisingly, none of the transition boundaries are independent of cylinder diameter.

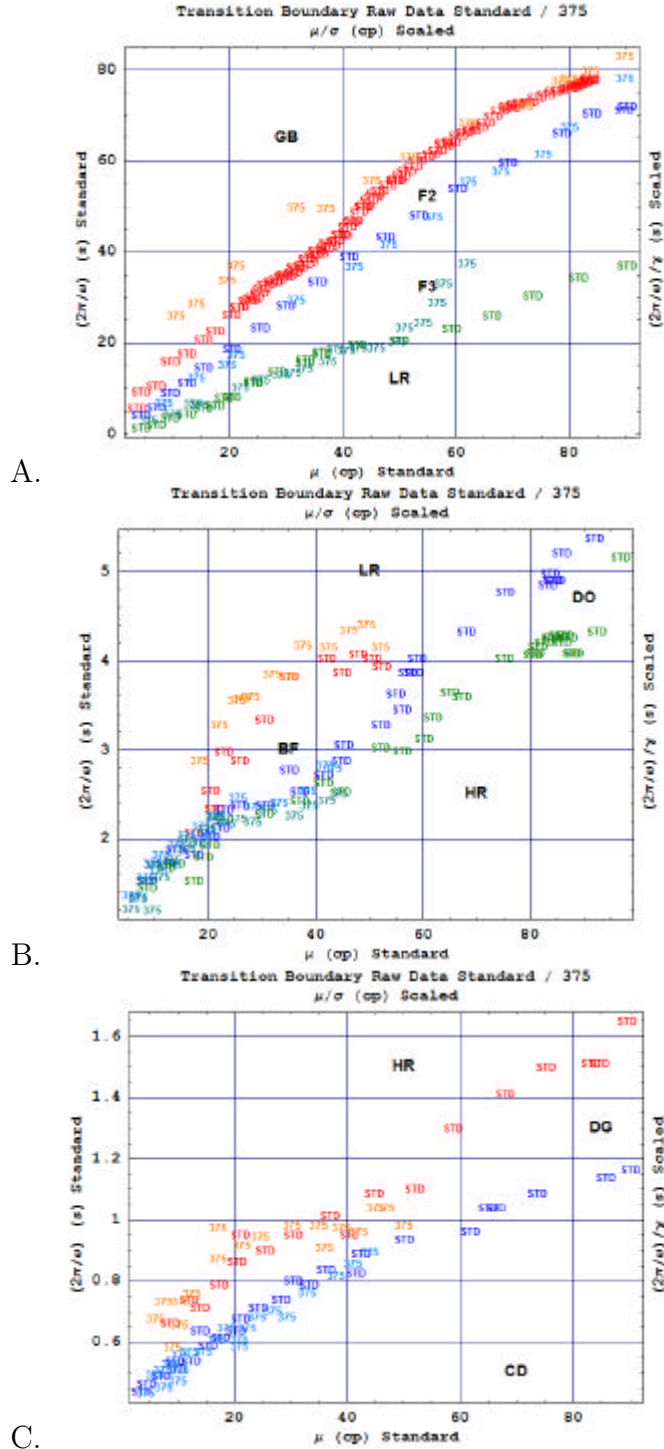
All of the coexistent state onset boundaries required viscous scaling in addition to temporal scaling. No regular pattern is observed in the scaling numbers, save that σ and γ are of comparable magnitude.

The Near Homogeneous phase could not be reproduced in the 375 system. The viscosity scaling demonstrated by the DoHr curve in Figure 5.10B indicates the *effective viscosity*, μ/σ , only achieves 45 centipoise. To reach the 80 centipoise necessary for the Near Homogeneous phase, a viscosity of $\mu \approx 160$ centipoise would be required. Additional study should be performed ($160 \rightarrow 180cp$) to further test this scaling prediction.

Boundary	$\sigma(100)$	$\sigma(375)$	$\gamma(100)$	$\gamma(375)$
GbF2	1.00	1.00	8.90	3.80
F2F3	1.00	1.00	2.45	1.25
F3Lr	1.45	1.45	4.25	1.15
LrBf	0.49	0.75	0.78	1.00
LrDo	1.00	2.00	1.10	1.80
DoHr	0.94	2.00	1.10	1.75
HrDg	1.00	1.85	1.00	1.35
DgCd	1.00	1.90	1.00	1.30
NhHr	0.99	n.a	1.23	n.a
OL	1.00	0.67	1.35	0.77
CL	1.00	2.60	1.15	2.60
HF	1.00	0.92	1.00	1.12
SB	1.00	0.60	1.00	0.95

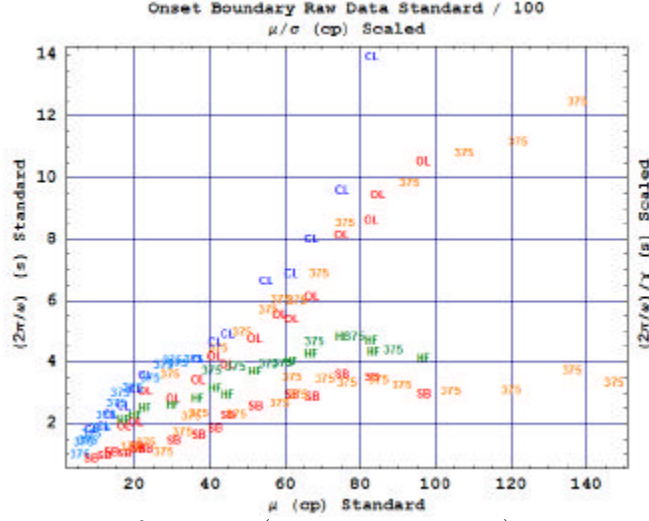
Scaling parameters needed to adjust the raw data collected from the 100 micron and Double Diameter cells. The two parameters modify the raw data from the two systems as follows: $\mu_{scaled} = \mu_{raw}/\sigma$ and $T_{scaled} = T_{raw}/\gamma$. Since the Near Homogeneous state could not be located in the $3.75cm$ cell, no scaling information is available. (100) refers to the $100\mu m$ system, and (375) refers to the 375 system.

Table 5.2: Raw Scaling Parameters



Raw scaling of the 375 (Double Diameter) system's transition boundaries. Each boundary is scaled by the correct σ and γ to overlay the corresponding Standard transition boundary. The values of σ and γ for each boundary is given in Table 5.2.

Figure 5.10: Raw Scaling of 375 micron Boundaries



Raw scaling of the 375 (Double Diameter) system's coexistent state onset boundaries. Each boundary is scaled by the correct σ and γ to overlay the corresponding Standard onset boundary. The values of σ and γ for each boundary is given in Table 5.2. The Standard onset boundaries designate the onset of each coexistent state by the two letter designation defined in Section 4.12.

Figure 5.11: Raw Scaling of 375 micron Coexistent States

5.4 Dimensionless Parameter Analysis

5.4.1 Units Analysis

In lieu of a theory, units analysis methods can often shed light into the dimensionless control parameters. This approach is limited, however, since theoretical arguments are absent from consideration, but a judicious approach can often yield helpful, if not meaningful, results.

The length of the cylinder has been shown to have negligible effects on the system, but the cylinder diameter, $2R$, is important. Similarly, the particle diameter, $2a$, is also significant. Other values which may (or may not) contribute to the behavior of the system are: solvent viscosity, μ , solvent density, ρ_s , particle differential density, $\Delta\rho$ gravity, g , and rotation period, T . Each of these can contribute independently as follows:

$$R^\alpha a^\beta (\Delta\rho)^\zeta T^\gamma \mu^\epsilon g^\chi \rho_s^\xi \quad (5.5)$$

Replacing the variables by their base units of length, mass, and time results in the following constraints for non-dimensionality:

$$\epsilon + \zeta + \xi = 0$$

$$\alpha + \beta - \epsilon - 3(\zeta + \xi) = 0$$

$$\gamma - \epsilon - 2\chi = 0$$

Since there are only three fundamental units, there are three equations. Unfortunately, there are seven variables which leaves four free parameters. I have chosen to solve each equation for one fundamental unit.

$$\alpha = -\beta - 2\epsilon - \chi$$

$$\gamma = \epsilon + 2\chi$$

$$\zeta = -\epsilon - \xi$$

These values can be put into Equation 5.5 to form a set of dimensionless values.

$$R^{-\beta-2\epsilon-\chi} a^\beta (\Delta\rho)^{-\epsilon-\xi} T^{\epsilon+2\chi} \mu^\epsilon g^\chi \rho_s^\xi$$

These terms can be collected to form dimensionless parameters. We can also replace T by $1/\omega$ to make the terms more familiar.

$$\left(\frac{a}{R}\right)^\beta \left(\frac{g}{R\omega^2}\right)^\chi \left(\frac{\mu}{\rho_s R^2 \omega}\right)^\epsilon \left(\frac{\rho_s}{\Delta\rho}\right)^{\xi+\epsilon} \quad (5.6)$$

Examination of these four parameters yields some potential understanding of the system. The β term is a ratio of the two length scales in the problem. This may be a consequential term in the effective range of forces as observed in previous chapters wherein the patterns take place on two separate, yet conjoined, length scales. The χ term is the force ratio of forces in the problem, namely gravity and centrifugal force. The competition of these two forces can be seen in the pattern development. The ϵ term is actually an inverse Reynolds number

$$\frac{1}{Re} = \frac{\mu}{\rho_s (R\omega) R} = \frac{\nu}{(R\omega) R}$$

where the kinematic viscosity, ν , is defined as

$$\nu = \frac{\mu}{\rho_s}$$

The Reynolds number is understood to represent the competition of inertial forces to viscous forces.

5.4.2 Dimensionless Boundary Analysis

If we assume that a specific value of equation 5.6 determines a transition boundary, then we have

$$\left(\frac{a}{R}\right)^\beta \left(\frac{g}{R\omega^2}\right)^\chi \left(\frac{\mu}{\rho_s R^2 \omega}\right)^\epsilon \left(\frac{\rho_s}{\Delta\rho}\right)^{\xi+\epsilon} = C_{boundary} \quad (5.7)$$

for some value of $C_{boundary}$ and exponents β , χ , ϵ , and ξ . Knowing these values would lend insight into the transition boundaries and the phases which lay between them, as well as giving predicting power for arbitrary cylinders, particles, etc.

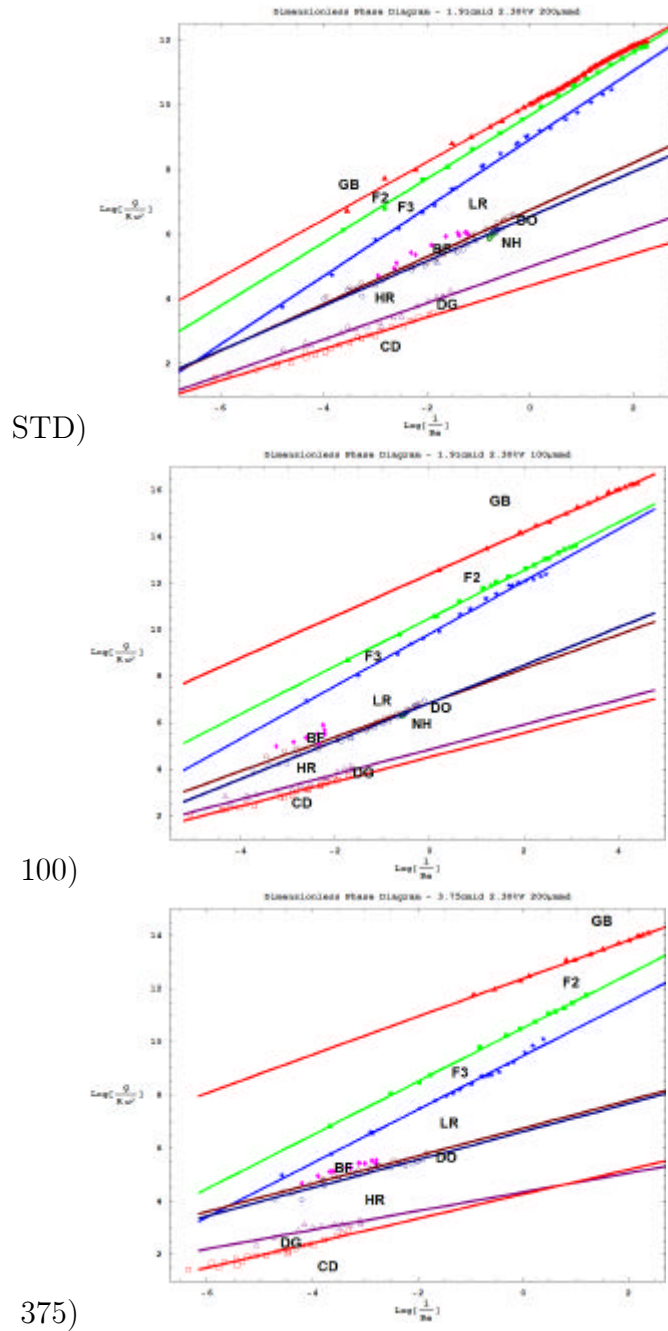
The log-log plots shown in Figure 5.12 using $\frac{g}{R\omega^2}$ and $\frac{1}{Re}$ as control variables demonstrate profound linear behavior. Of the 9 transition boundaries, 7 can be accurately fit with a linear function. The fitting results are given in Tables 5.3 and 5.4. The fitting equation is of the form

$$y = B + Mx \quad (5.8)$$

where $y = Ln(\frac{g}{R\omega^2})$ and $x = Ln(\frac{1}{Re})$. By assuming Equation 5.6 holds true for some value of C_i , we can estimate the forms of B and M .

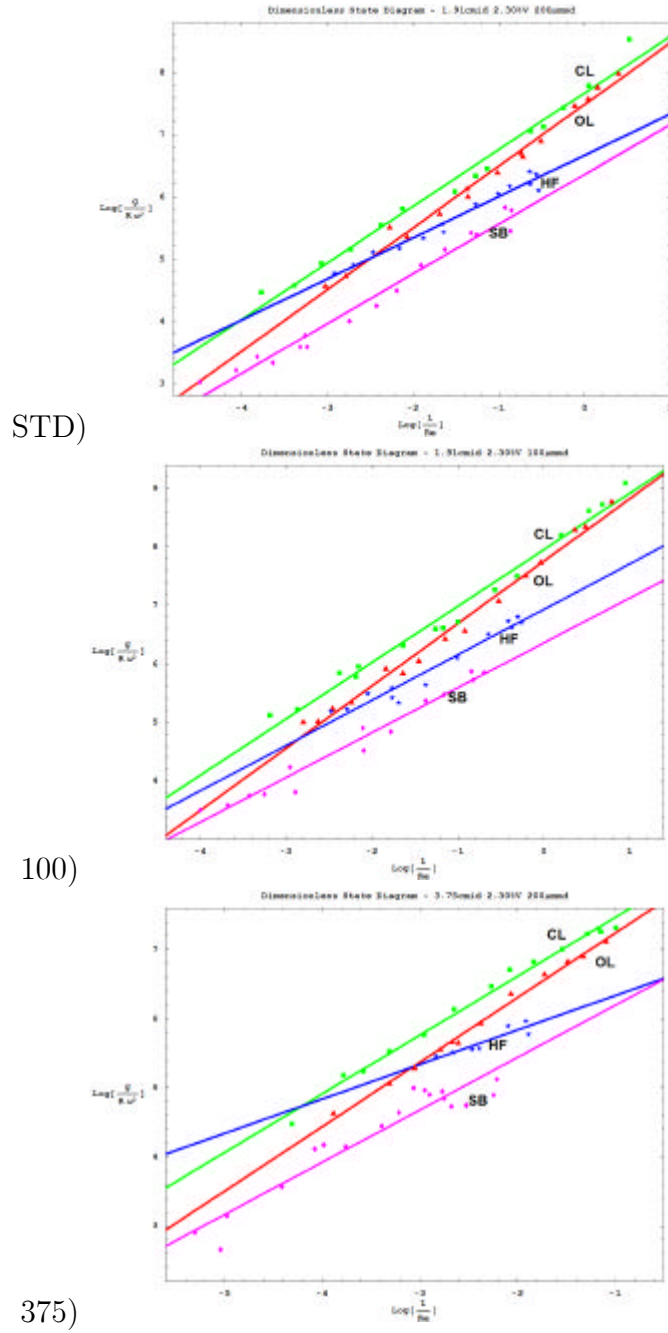
$$\begin{aligned} Ln\left(\left(\frac{a}{R}\right)^\beta \left(\frac{g}{R\omega^2}\right)^\chi \left(\frac{\mu}{\rho_s R^2 \omega}\right)^\epsilon \left(\frac{\rho_s}{\Delta\rho}\right)^{\xi+\epsilon}\right) &= Ln(C_i) \\ -Ln\left(\frac{g}{R\omega^2}\right) &= \frac{\epsilon}{\chi} Ln\left(\frac{1}{Re}\right) + Ln\left(\left(\frac{a}{R}\right)^{\frac{\beta}{\chi}} \left(\frac{\rho_s}{\Delta\rho}\right)^{\frac{\xi+\epsilon}{\chi}} C_i^{-\frac{1}{\chi}}\right) \end{aligned} \quad (5.9)$$

The straight lines in the Log-Log plots suggest the power-law behavior for the transition boundaries. Many of the seven (7) boundaries in Table 5.3 demonstrate similar changes in slope. What is surprising is the ability of this analytical method to



The Reynolds Number is based on Cylinder Size. The linear approximations are superimposed over the data points for each of the 7 transition boundaries which are linear. The phase space between each pair of boundaries expresses the regime wherein the indicated phase, as defined in the text, exists. The (STD) diagram illustrates the Standard System ($200\mu\text{m}$, 1.9cm , $2.3\%V$). The (100) diagram illustrates half particle size system ($100\mu\text{m}$, 1.9cm , $2.3\%V$). The (375) illustrates the double diameter system ($200\mu\text{m}$, 3.75cm , $2.3\%V$).

Figure 5.12: Dimensionless Phase Diagrams



The Reynolds Number is based on Cylinder Size. The linear approximations are superimposed over the data points for each of the 4 coexistent onset boundaries. The (STD) diagram illustrates the Standard System ($200\mu\text{m}$, 1.9cm , $2.3\%V$). The (100) diagram illustrates half particle size system ($100\mu\text{m}$, 1.9cm , $2.3\%V$). The (375) illustrates the double diameter system ($200\mu\text{m}$, 3.75cm , $2.3\%V$).

Figure 5.13: Dimensionless State Diagrams

Boundary	M(STD)	M(100)	M(375)	M(avg)
GbF2	0.891	0.901	0.718	0.837
F2F3	0.982	1.03	1.01	1.01
F3Lr	1.06	1.13	1.01	1.07
LrDo	0.728	0.734	0.523	0.661
DoHr	0.692	0.815	0.529	0.679
HrDg	0.560	0.534	0.384	0.493
DgCd	0.489	0.524	0.462	0.492
OL	0.992	1.07	0.933	0.997
CL	0.911	0.966	0.851	0.909
HF	0.662	0.777	0.499	0.646
SB	0.799	0.768	0.758	0.775

Slope values for the Standard System ($200\mu m$, $3.8cmid$, $2.3\%V$), the 100 system ($200\mu m$, $3.8cmid$, $2.3\%V$), and the 375 system ($200\mu m$, $3.75cmid$, $2.3\%V$). The data is calculated using a Reynolds Number based on Cylinder size. The linear equation is of the form $y = B + Mx$.

Table 5.3: Boundary Slope (M) values for the three systems

Boundary	B(STD)	B(100)	B(375)
GbF2	10.0	12.4	12.4
F2F3	9.68	10.5	10.5
F3Lr	8.95	9.83	9.48
LrDo	6.76	6.86	6.76
DoHr	6.56	6.85	6.63
HrDg	4.99	4.86	4.45
DgCd	4.41	4.43	4.28
OL	7.48	7.76	8.17
CL	7.67	7.95	8.31
HF	6.67	6.93	6.83
SB	6.36	6.36	6.95

Intercept values for the Standard System ($200\mu m$, $3.8cmid$, $2.3\%V$), the 100 system ($200\mu m$, $3.8cmid$, $2.3\%V$), and the 375 system ($200\mu m$, $3.75cmid$, $2.3\%V$). The data is calculated using a Reynolds Number based on Cylinder size. The linear equation is of the form $y = B + Mx$.

Table 5.4: Boundary Intercept (B) values for the three systems

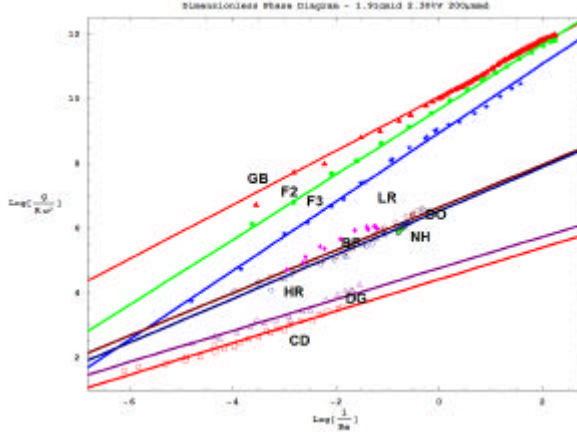
straighten curves such as F3Lr. It is expected under this analysis that B would vary considerably with the experimental parameters; however, M should remain unchanged if the parameters are representative of the forces governing the transition.

Direct comparison of the 3 slopes for each boundary is given in Table 5.3. It is seen that M is not necessarily constant among the three samples. The cause of this variation is the inaccuracy of the linear fit. Averaging these three values, however, gives an accurate fit to the data. This is shown in Figure 5.14. The average values of M are given in Table 5.3, and the resulting set of B values are given in Table 5.5. The values of B follow an interesting and unexpected trend of decreasing magnitude as one moves down the table.

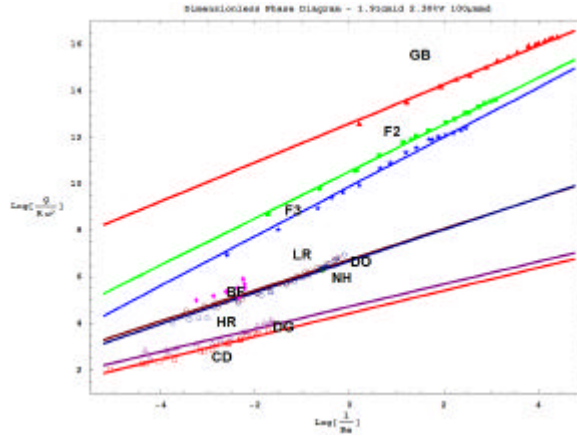
Boundary	B(STD)	B(100)	B(375)
GbF2	10.15	12.6	12.3
F2F3	9.68	10.5	10.5
F3Lr	8.95	9.88	9.55
LrDo	6.65	6.74	7.18
DoHr	6.54	6.68	7.09
HrDg	4.80	4.75	4.89
DgCd	4.42	4.43	4.42
OL	7.49	7.68	8.32
CL	7.67	7.89	8.45
HF	6.64	6.77	7.17
SB	6.30	6.37	7.01

Boundary Intercept (B) values for the three systems based on the average individual slopes. The Standard System ($200\mu m$, $3.8cmid$, $2.3\%V$), the 100 system ($200\mu m$, $3.8cmid$, $2.3\%V$), and the 375 system ($200\mu m$, $3.8cmid$, $2.3\%V$). The data is calculated using a Reynolds Number based on Cylinder size. Line equation is of the form $y = < B > + < M > x$.

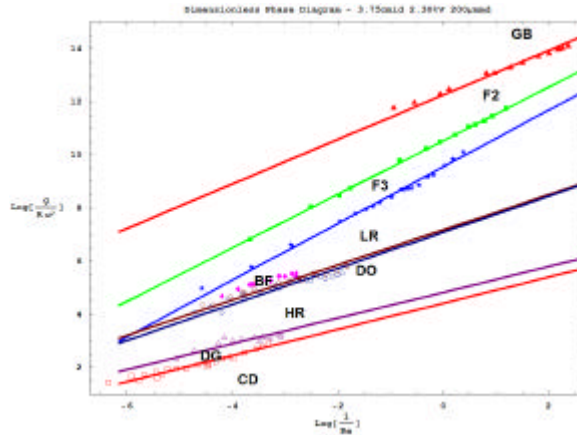
Table 5.5: Intercepts using Average Slope



STD)



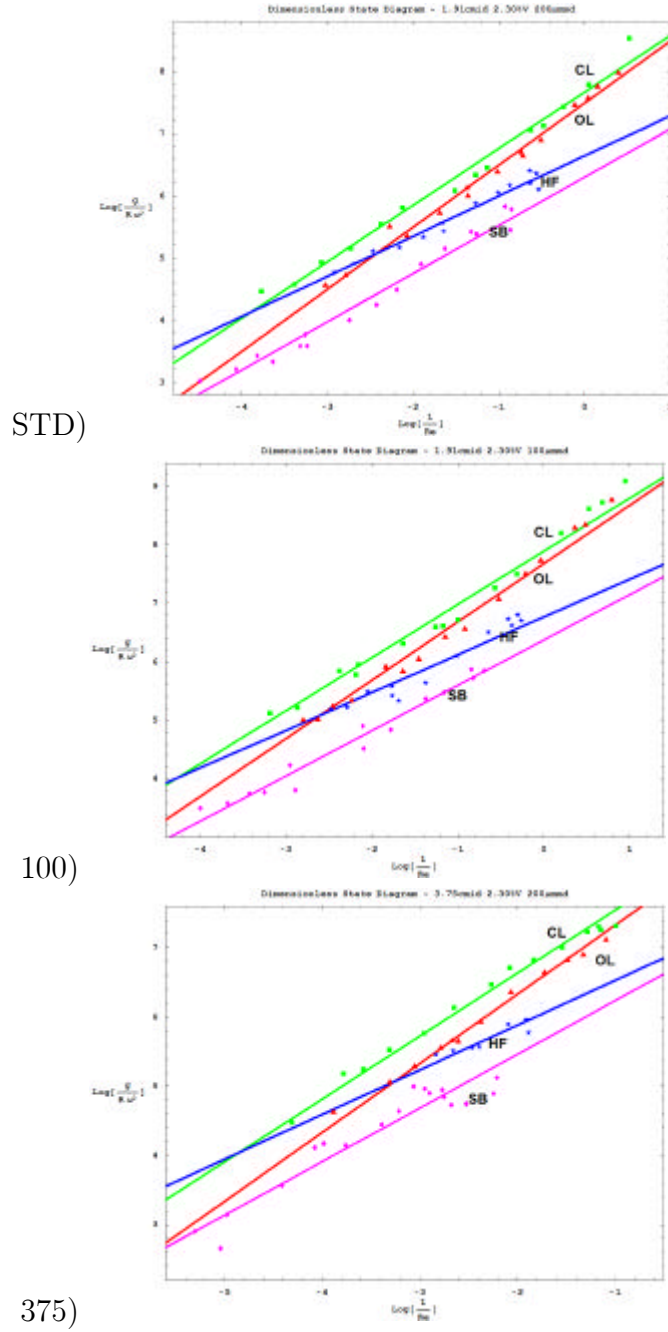
100)



375)

Resulting Dimensionless Phase Diagrams when forcing the use of an Average Slope value. The (STD) diagram illustrates the Standard System ($200\mu\text{m}$, 1.9cm , $2.3\%V$). The (100) diagram illustrates half particle size system ($100\mu\text{m}$, 1.9cm , $2.3\%V$). The (375) illustrates the double diameter system ($200\mu\text{m}$, 3.75cm , $2.3\%V$).

Figure 5.14: Dimensionless Phase Diagrams using Average Slope



Resulting Dimensionless State Diagrams when forcing the use of an Average Slope value. The (STD) diagram illustrates the Standard System ($200\mu m, 1.9cm, 2.3\%V$). The (100) diagram illustrates half particle size system ($100\mu m, 1.9cm, 2.3\%V$). The (375) illustrates the double diameter system ($200\mu m, 3.75cm, 2.3\%V$).

Figure 5.15: Dimensionless State Diagrams using Average Slope

5.5 Navier-Stokes Analysis

The Navier-Stokes equation for the suspension can be written as.

$$\rho \frac{\delta(\bar{v})}{\delta t} + \rho \bar{v} \cdot (\nabla(\bar{v})) = (\Delta\rho)g - \nabla P + \mu \nabla^2(\bar{v}) \quad (5.10)$$

For steady state, one has $\frac{\delta}{\delta t} = 0$. If we introduce the following dimensionless length, velocity, and gravitational terms,

$$r \rightarrow \frac{r}{R}$$

$$v \rightarrow \frac{v}{R\omega}$$

$$g \rightarrow \frac{g}{R\omega^2}$$

Equation 5.10 becomes

$$\begin{aligned} \rho \frac{\bar{v}}{R\omega} \cdot (\nabla(\frac{\bar{v}}{R\omega})) &= (\Delta\rho) \frac{g}{R\omega^2} - \nabla P + \frac{\mu}{R} \nabla^2(\frac{\bar{v}}{R\omega}) \\ \frac{\bar{v}}{R\omega} \cdot (\nabla(\frac{\bar{v}}{R\omega})) &= \frac{\Delta\rho}{\rho} \frac{g}{R\omega^2} - \frac{\nabla P}{\rho} + \frac{\mu}{\rho R^2\omega} \nabla^2(\bar{v}) \end{aligned} \quad (5.11)$$

which suggests the following dimensionless parameters:

$$\frac{\Delta\rho}{\rho} \quad (5.12)$$

$$\frac{g}{R\omega^2} \quad (5.13)$$

$$\frac{\mu}{\rho R^2\omega} = \frac{1}{Re} \quad (5.14)$$

Interestingly, this analysis produces a similar set of dimensionless parameters as given in Equation 5.6.

5.6 Volume Fraction Dependence

Several transition boundaries are also measured using five different volume fractions in a standard cylinder: 1.06%, 1.47%, 1.88%, 2.29%, 2.70%. The results are shown in Figure 5.16. Close examination of these plots provides some insight into the effect of particle concentration on the development of the four transitions. The transition boundaries surrounding the Near Homogeneous phase were also studied and found to be invariant over the range of concentrations studied.

The four transitions depicted in Figure 5.16 follow a general trend of increasing rotation rate, ω , for increasing concentration, ϕ . This trend is clearly viscosity dependent. Further study is necessary to determine the concentration dependence of the remaining boundaries, and the exact nature of this viscosity dependence. Understanding the strong correlation between concentration and viscosity is essential to the understanding of this system.

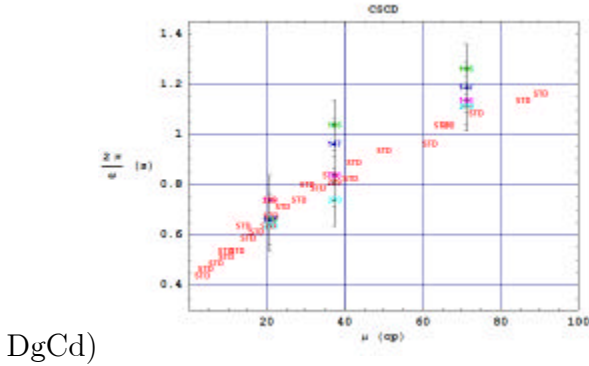
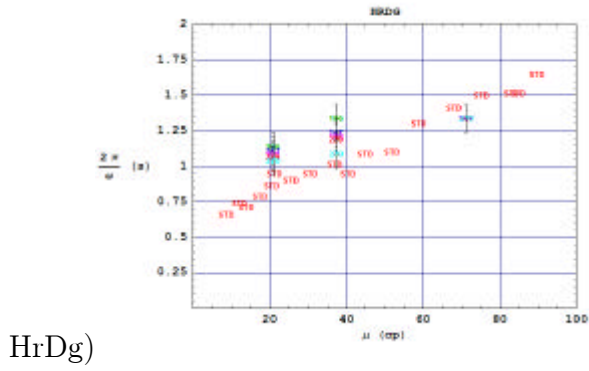
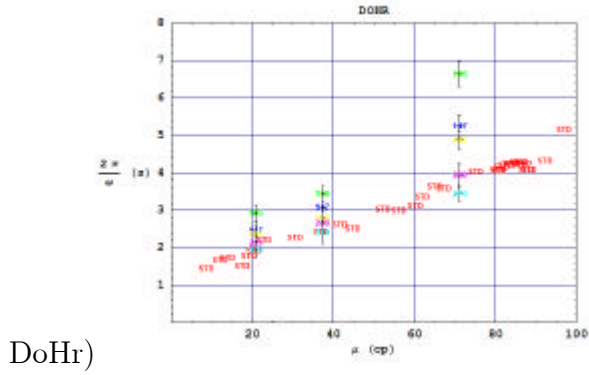
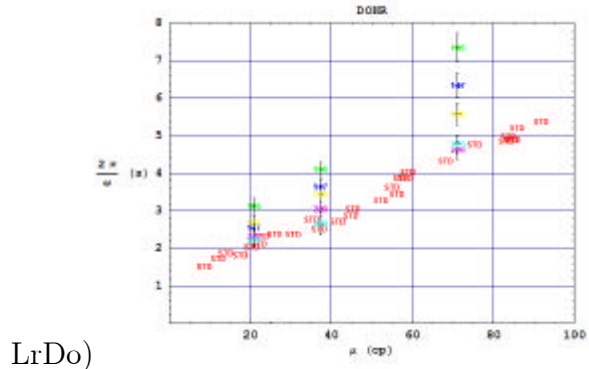
5.7 Correlation with Other Recent Experiments

Several papers have recently been published reporting experiments in rotating cylinders similar to that in this work. It is necessary to correlate the information presented in these papers with the observations and analysis in this study.

5.7.1 Breu, Kruelle, and Rehberg (2003)[17]

Experiments were performed in water using $300\mu m$ particles of comparable density. Volume fractions were slightly higher, $\approx 2.5\%$. Rotation rates varied from $2.9Hz$ to $3.9Hz$. The region of physical phase space covered by these experiments is marked in blue in Figure 5.17. Two things are immediately apparent: (1) the phase extrapolation of the HrDg boundary is inaccurate, as Breu *et al.* commented on observing the Discontinuous Gradient phase below $3.25Hz$ ($0.308seconds/rotation$), ie. the DgCd boundary. (2) Breu *et al.* is clearly working in the Centrifugal Dominance phase, as expected.

Breu's arguments for the cause of the instability seems reasonable, though obser-



The symbols represent the five concentrations used in the study: 2.70%V, 2.29%V, 1.88%V, 1.47%V, and 1.06%V. The "STD" symbol represents the Standard System (2.30%V, 200 μ mMD, 1.91cmID).

Figure 5.16: Transition boundaries using different concentrations

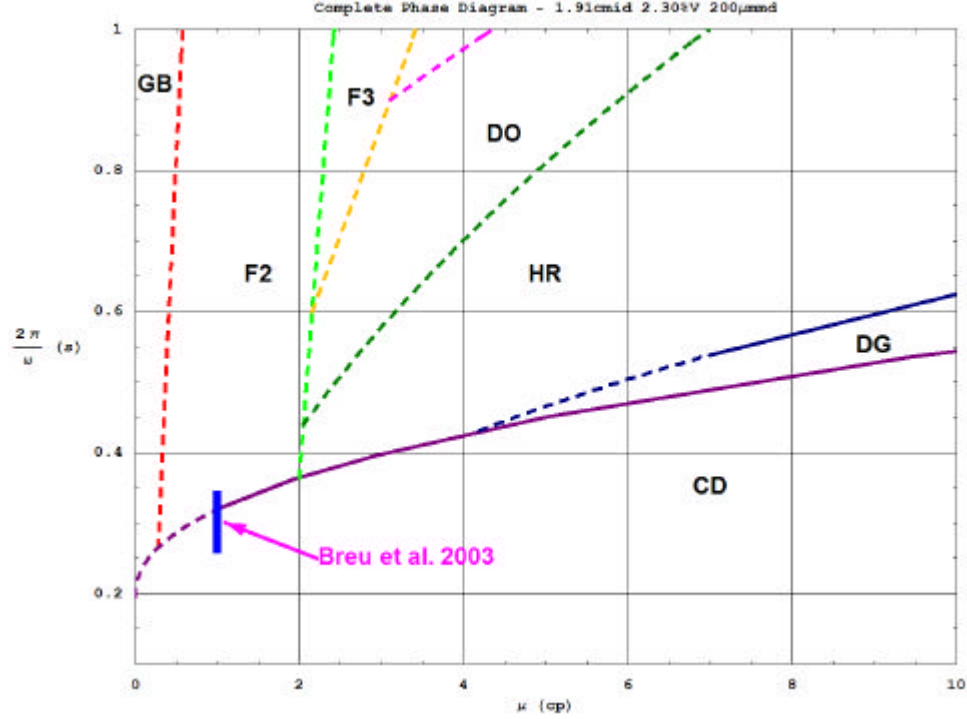


Figure 5.17: Phase space covered by Breu *et al.* in their 2003 paper.

vation in the $r - \theta$ plane has not revealed particles lifting off the wall; nevertheless, particles have been observed migrating in the direction of rotation along the inside surface of the cylinder. This could be an artifact of the experiment similar to the wagon wheel syndrome in western movies, or this could be actual migration of the particles. At this time, the evidence is not clear. Further examination is warranted.

5.7.2 Breu, Kruelle, and Rehberg (2004)[19]

Experiments were performed in water using $300\mu m$ particles of comparable density. Volume fractions were $\approx 2.5\%$. Rotation rates varied from $0.9Hz$ to $1.1Hz$. The solvent viscosity was varied from $0.92cp$ (water) to $7.84cp$ using aqueous solutions of glycerine. The region of physical phase space covered by the experiments is outlined in blue in Figure 5.18. It is immediately obvious that Breu covered several phases throughout the experiments detailed. As suspected, the "traveling waves" reported in the paper are likely the "fingers" discussed in Chapter 4. Breu allows only **50**

seconds for the system to reach steady state. It is this brief period of time that results in the "rigid-body" phase reported as the upper limit. This time frame is orders of magnitude too short for the system to achieve steady state. The lower right corner of the box in Figure 5.18 enters the High Rotation Transition phase which requires *at least* 1 hour (3600 seconds) to achieve anything close to steady state. Reliable results would require ≈ 4 hours between the measurements. Even for the Low Rotation Transition, the 50 second time interval is not long enough to be reliable. Measurement intervals should be **no less than** 10 minutes to allow adequate time for the system to redistribute the mass (the longest of the three convergence times).

It has been observed throughout the fingering phases that fingers travel axially in **both** directions. Breu *et al.* has attempted to measure these traveling fingers, or "traveling waves", using 25 frame per second video imaging. Only a strip 2 pixels thick down the center of the tube is retained from each image. This eliminates the ability for the image to capture even two dimensional motion. The strips are aligned vertically to illustrate motion in the axial direction. What this method captures is the onset of axial motion for the fingers, and even the presence of fingers. Breu then goes into great length analyzing the speed at which these "waves" travel, but no explanation for the formation of any "organized states" is offered.

5.7.3 Lipson (2001)[16]

Experiments were performed in water using supersaturated NH_4Cl . Rotation rates varied from $0.5 \rightarrow 2.0$ seconds per rotation. The solvent viscosity is unknown but can be assumed near water ($0.92cp$) or slightly higher. The estimated region of physical phase space covered by the experiments is outlined in blue in Figure 5.19. Comparison with Lipson's results is difficult, since the particles vary in size and are of near-neutral buoyancy. In spite of the estimated phase space presented in Figure 5.19, the pictures and descriptions provided by Lipson match the Discontinuous Gradient phase. Although the onset of this phase is independent of particle size, it may depend greatly on the particle density. The band spacing reported by Lipson is comparable to the Band Formation phase, which is highly dependant on particle size. Lipson

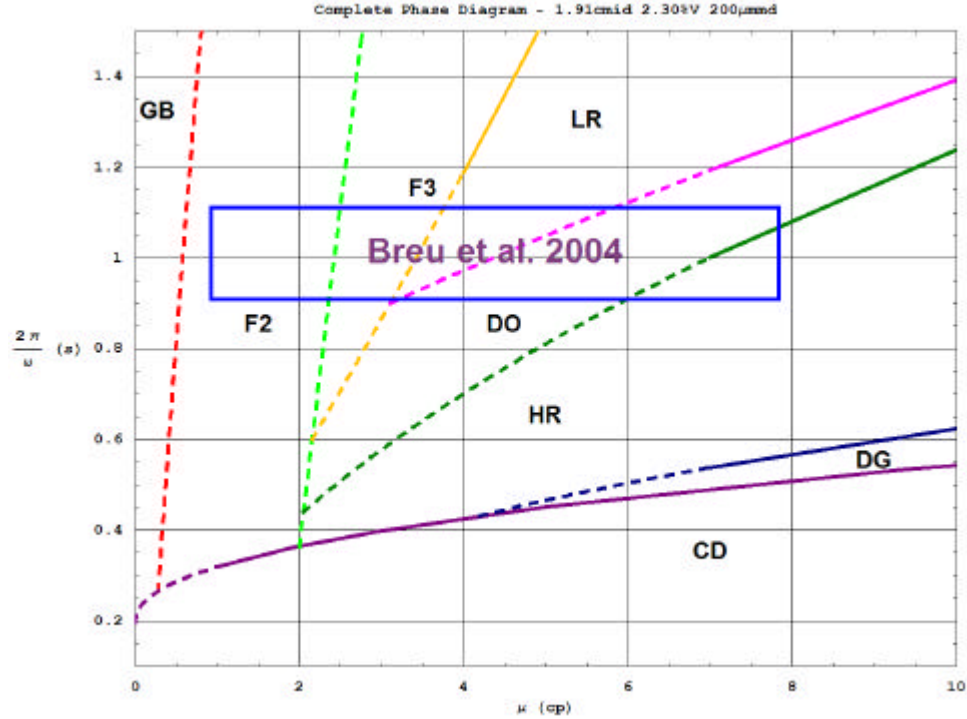


Figure 5.18: Phase space covered by Breu *et al.* in their 2004 paper.

commented in the discussion that banding only appears with heavier crystals ”when they are very small,” indicating that particle size and density are important. Based on the scaling property presented in this chapter, I would agree with Lipson that near-neutral buoyancy is required for band formation in this case. Because the solvent viscosity is extremely low, and particle settling velocity increases rapidly with both particle density and size, the system may rapidly move into the fingering or granular bed phases.

Lipson’s analogy with Rayleigh-Bénard convection produces appropriate wavelengths of $\approx 2.34R$ and a believable flow pattern. Lipson suggests the banding mechanism could be either particle attraction mediated by the fluid or particle reaction to the velocity field. Observations reported in this paper suggest the former, particle pair interactions mediated by the fluid causing an attraction. Saffman lift can be ruled out, since the particles used in this paper are significantly heavier than the bulk fluid. Similarly, I agree that acoustic streaming is far too weak and short ranged. The particles in the suspension are the driving force, not a passive scalar. It is the

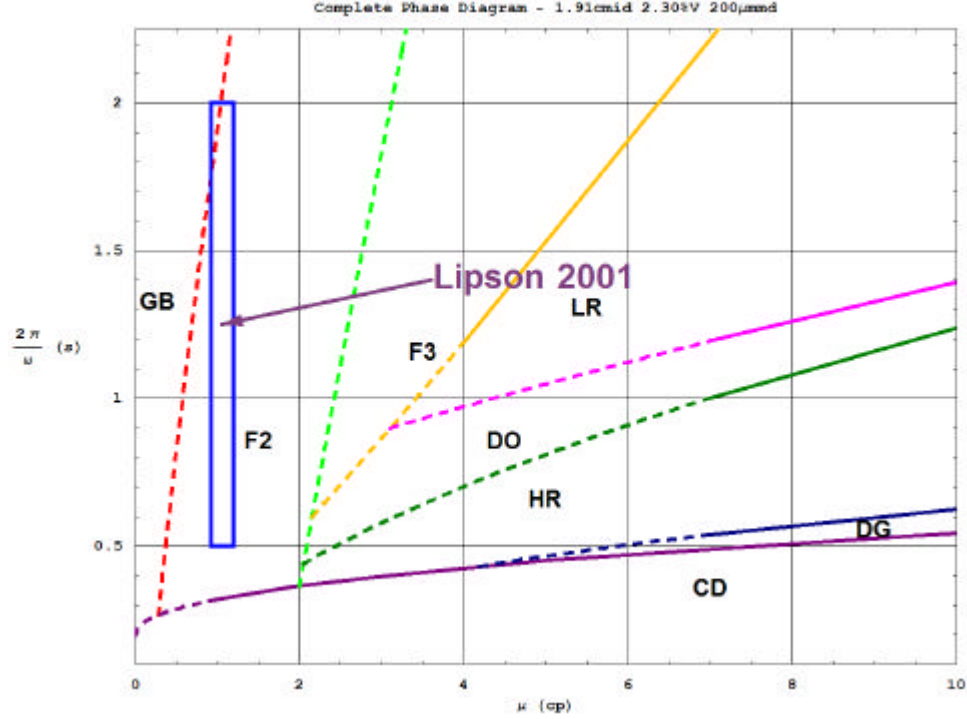


Figure 5.19: Phase space covered by Lipson in the 2001 paper.

buoyant density and relative size of the particles that is at issue in this system. The solvent viscosity is both a damping force and the method of momentum transmission; therefore, the fluid mediates the flow perturbations caused by the particles.

5.7.4 Seiden, Lipson, and Franklin (2004)[20]

Experiments were performed in cylinders with inside radius ranged from 1.28cm to 2.29cm . The rotation rate is fixed at ≈ 6 radians per second. Seiden claims the exact value does not seem to be important. Nylon, polystyrene, and Plexiglas particles were used in addition to air bubbles and polydisperse dendritic crystals. The solvent was water or some dilute aqueous solution of glycerine to increase the viscosity as much as 20% ($0.92 \rightarrow 1.10$). The estimated region of physical phase space covered by the experiments is outlined in blue in Figure 5.20. Exact comparison is difficult since the particles are of near-neutral buoyancy and extremely large (3mm diameter), but close examination of the covered phase space makes it clear why the

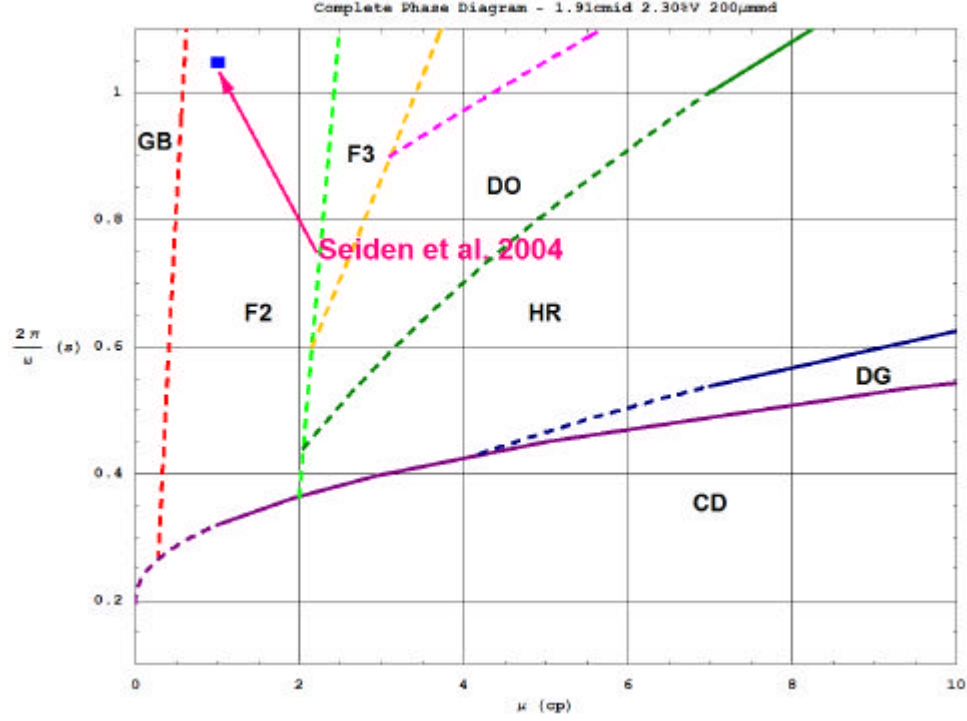


Figure 5.20: Phase space covered by Seiden *et al.* in their 2004 paper.

rotation period need not be precisely controlled. In this region, the neighboring phase boundaries appear dependent mostly on the solvent viscosity, not the rotation period. The phase observed by Seiden is unclear. Observed wavelengths are $1.4 \rightarrow 2.0$ inside diameters suggesting the system is producing unstable bands or, perhaps, in one of the fingering phases. Seiden's derivation using inertial waves is interesting, but the result yields a wavelength of $\approx 4R$, which is slightly large, though it works acceptably with their system as an upper limit. Seiden *et al.* made a brief comment regarding the particle driving force reducing this wavelength. The analysis seems valid but completely ignores the contribution of solvent viscosity. This seems natural for the problem presented in Seiden's paper, since they only consider water (or a solvent with viscosity very close to water); furthermore, the density of the particles is assumed comparable to that of the solvent. In light of these facts, this is a narrowly focused solution. Attention needs to be given to the greater problem before any judgment can be levied on this type of analysis.

Chapter 6

Conclusions and Recommendations

This seemingly simple system has been shown to produce dramatic and unexpected behavior. A rich array of concentration and velocity patterns are observed over a wide range of rotation rates and solvent viscosities. These patterns are found to be extremely robust, occurring over a range of experimental parameters. Both broad and abrupt transitions have been observed between adjacent phases. Hysteresis in phase development has not been observed for any of the transition boundaries within the experimental resolution of 0.025 seconds per rotation. Pattern selection by the system has been observed to be independent of initial conditions or cylinder length, though the cylinder length can affect the number of periodic structures formed over the length of the cylinder. The number of periodic structures developed is proportional to the nearest half wavelength. Seiden *et al.* have observed and studied this phenomena in one of their recent papers[20].

Our attempts to arrive at dimensionless control parameters have yielded preliminary but reassuring results. These parameters are derived from our current knowledge of the forces affecting the system, but do not account for particle interactions. The scaling analysis suggests that the phase diagram can be divided into three regions. In the low rotation rate regime, the transition boundaries show strong particle size dependence, indicating that hydrodynamic forces resulting from the settling of individual particles are dominant. Conversely, the high rotation rate regime shows negligible particle size dependence indicating that the centrifugal force is dominant. This division in the phase diagram suggests that at least two dimensionless parameters are needed to describe the phase behavior of the system. The transition boundaries in

the intermediate regime show more complex behavior suggesting a strong competition among the viscous, gravitational, and centrifugal forces.

Without a theory, it is difficult to know how to analyze the data in a meaningful way; nevertheless, empirical analysis can stumble blindly forward and suggest possible courses of theoretical modeling that might result in an effective theory. To that end, further experimentation is necessary to test the effects of other parameters such as particle density and shape, cylinder eccentricity, solvent properties, and additional cylinder and particle sizes. These additional studies will complete the picture which I have started in this study. Smaller solvent viscosities should also be examined under the conditions described here to complete the phase diagram. Seiden, Lipson and Breu have studied similar rotating systems using water (1 centipoise) as a solvent, and I have discussed how their isolated observations and studies fit in with the global picture presented in this work. Their observations only illustrate the enormous volume of work remaining in this area. Understanding this simple system will shed new light to the fields of complex fluids and particle suspensions and provide a theoretical framework to a long forsaken and theoretically prohibitive area of hydrodynamics.

Chapter 7

Bibliography

1. Boote, O A M & Thomas, P J (1999) Effects of granular additives on transition boundaries between flow states of rimming flows. *Phys. Fluids* 11(8):2020
2. Balmer, R T (1970) The Hygrocyt a stability phenomenon in continuum mechanics. *Nature* 227:600-601
3. Moffatt, H K (1977) Behavior of a viscous film on the outer surface of a rotating cylinder. *J Mecanique* 16:651
4. Melo, F (1993) Localized states in a film dragging experiment. *Phys Rev E* 48:2704
5. Wilson S D R & Williams J (1996) The flow of a liquid film on the inside of a rotating cylinder, and some related problems. *Phys. Fluids* 9(8):2184
6. Thoroddsen, S T & Mahadevan, L (1997) Experimental study of coating flows in a partially-filled horizontally rotating cylinder. *Exp Fluids* 23:1
7. Thomas, P J & Riddell, G D & Kooner, S & King G P (2001) Fine structure of granular banding in two-phase rimming flow. *Phys. Fluids* 13(9):2720
8. Tirumkudulu, M & Mileo, A & Acrivos, A (2000) Particle segregation in monodisperse sheared suspensions in a partially filled rotating horizontal cylinder. *Phys. Fluids* 12(6):1615-1618
9. Govindarajan, R & Nott, P R & Ramaswamy, S (2001) Theory of suspension segregation in partially filled horizontal rotating cylinders. *Phys. Fluids* 13(12):3517
10. A. Acrivos (2002) Comment on "Theory of suspension segregation in partially filled horizontal rotating cylinders," *Phys. Fluids* 14:3750

11. B. Jin & A. Acrivos (2004) Theory of particle segregation in rimming flows of suspensions containing neutrally buoyant particles, *Phys. Fluids* 16:641
12. B. D. Timberlake & J. F. Morris (2002) Concentration band dynamics in free-surface Couette flow of a suspension, *Phys. Fluids* 14:1580
13. N. P. Duong, A. E. Hosoi, & T. Shinbrot (2004) Periodic Knolls and Valleys: Coexistence of Solid and Liquid States in Granular Suspensions, *Phys. Rev. Lett.* 92:224502
14. P. Raiskinmäki, J. A. ström, M. Kataja, M. Latva-Kokko, A. Koponen, A. Jämsberg, A. Shakib-Manesh, & J. Timonen (2003) Clustering and viscosity in a shear flow of a particulate suspension, *Phys. Rev. E* 68:061403
15. G. O. Roberts, D. M. Kornfeld, & W. W. Fowles (1991) Particle orbits in a rotating fluid. *J. Fluid Mech.* 229:555
16. S. G. Lipson (2001) Periodic banding in crystallization from rotating supersaturated solutions. *J. Phys.: Condens. Matter* 13:5001
17. A. P. J. Breu, C. A. Kruelle, & I. Rehberg (2004) Pattern formation in a rotating aqueous suspension. *Europhys. Letters*, preprint
18. J. Lee, J. C. Ladd (2002) Axial segregation in a cylindrical centrifuge. *Phys. Rev. Letters* 89(10):104301
19. A. P. J. Breu, C. A. Kruelle, & I. Rehberg (2004) Oscillatory patterns in a rotating aqueous suspension. *Euro. Phys. J. E*, 13:189
20. G. Seiden, S. G. Lipson, & J. Franklin (2004) Oscillatory axial banding of particles suspended in a rotating fluid. *Phys. Rev. E* 69:015301(R)
21. E. J. Hinch, in *Disorder and Mixing*, E. Guyon *et al.* ed. (Kluwer Academic, Dordrecht, 1988), 155
22. V. K. Gupta, R. Sureshkumar, B. Khomami, & J. Azaiez (2002) Centrifugal instability of semidilute non-Brownian fiber suspensions, *Phys. Fluids* 14:1958
23. Reisfeld, B & Bankroff, S G (1992) Non-isothermal flow of a liquid film on a horizontal cylinder. *J Fluid Mech.* 236:167
24. Antanovskii, L (1996) Formation of a pointed drop in Taylor's four-roller mill. *J Fluid Mech.* 327:325

25. Ross, A B & Wilson, S K & Duffy, B R (2001) Thin-film flow of a viscoplastic material round a large horizontal stationary or rotating cylinder. *J Fluid Mech.* 430:309
26. Pukhnachev V V (1973) Lecture at the Autumn Course on Mathematical and Numerical Methods at the International Centre for Theoretical Physics, Trieste.
27. Lighthill M J & Whitham G B (1955) On kinematic waves I & II. *Proc. Roy. Soc.* A229:281
28. Preziosi L & Joseph D D (1987) The run-off condition for coating and rimming flows. *J Fluid Mech.* 187:99
29. Johnson, R E (1988) Steady-state coating flows inside a rotating horizontal cylinder. *J Fluid Mech.* 190:321
30. Deiber J A & Cerro R L (1976) Viscous flow with a free surface inside a horizontal rotating drum. *Ind. Engng. Chem. Fundam.* 15:102
31. Fried, E & Shen, A Q & Thoroddsen, S T (1998) Wave patterns in a thin layer of sand within a rotating horizontal cylinder. *Phys. Fluids* 10(1):10
32. O'Brien, S B G & Gath, E G (1998) The location of a shock in rimming flow. *Phys. Fluids* 10(4):1040
33. Hosoi, A E & Mahadevan, L (1999) Axial instability of a free-surface front in a partially filled horizontal rotating cylinder. *Phys. Fluids* 11(1):97
34. Tirumkudulu, M & Acrivos, A (2001) Coating flows within a rotating horizontal cylinder: Lubrication analysis, numerical computations, and experimental measurements. *Phys. Fluids* 13(1):14
35. N. Riley (2001) Steady streaming. *Annu. Rev. Fluid Mech* 33:43

Appendix A

Theory and Design of the Custom Indexer

The control unit operates under the following principle: A stable pulse train of fixed high frequency is input and counted. When the count reaches a prescribed value, an output pulse is generated, processed, amplified, and output to the motor control unit that in turn moves the motor 1 step. The output pulse also clears the counter and restarts the timing sequence. The prescribed value is set using thumbwheel switches with decimal values from 0-9 indicated on them. Each thumbwheel indicates one digit in the decimal expression of the count requirement. The output Pulse Period is an exact multiple of the input clock period according to the following equation:

$$T_{\text{Pulse}} = \frac{N_{\text{Count}}}{f_{\text{Clock}}} = N_{\text{Count}} T_{\text{Clock}} \quad (\text{A.1})$$

The rotation period of the cylinder can then be determined as follows:

$$T_{\text{Cylinder}} = N_{\text{Count}} T_{\text{Clock}} N_{\frac{\text{pulse}}{\text{rotation}}} \quad (\text{A.2})$$

For convenience, f_{Clock} is chosen as 1MHz. As previously mentioned, the Control Unit Resolution, $N_{\frac{\text{pulse}}{\text{rotation}}}$, is 25000 pulses per rotation. Equation A.2 then simplifies as follows:

$$T_{\text{Cylinder}} = N_{\text{Count}} (10^{-6} \frac{\text{Second}}{\text{Pulse}}) (25000 \frac{\text{Pulse}}{\text{Rotation}})$$

$$T_{\text{Cylinder}} = N_{\text{Count}} (10^{-6}) (2.5 \cdot 10^4) \frac{\text{Pulse Second}}{\text{Pulse Rotation}}$$

$$T_{\text{Cylinder}} = N_{\text{Count}} 2.5 \star 10^{-2} \frac{\text{Second}}{\text{Rotation}}$$

$$T_{\text{Cylinder}} = 0.025 N_{\text{Count}} \frac{\text{Second}}{\text{Rotation}} \quad (\text{A.3})$$

The errors built into the system can be broken down into two categories: errors in source clock frequency, and delays in semiconductor transitions. To minimize the errors due to source clock frequency, a crystal oscillator is purchased with precision as far in excess of source pulse period as possible. The source oscillators used by indexers discussed in this paper are measured at 999987Hz which equates to pulses with periods of $1.000012 \cdot 10^{-6}$ seconds; consequently, the error for a given indexer setting, N_{Count} , can be calculated as follows:

$$\delta T_{\text{Cylinder}} = N_{\text{Count}} \delta T_{\text{Clock}} N_{\frac{\text{pulse}}{\text{rotation}}}$$

$$\delta T_{\text{Cylinder}} = N_{\text{Count}} (1.2 \cdot 10^{-11} \frac{\text{Second}}{\text{Pulse}}) (2.5 \cdot 10^4 \frac{\text{pulse}}{\text{rotation}})$$

$$T_{\text{Cylinder}} = 3.0 \cdot 10^{-7} \frac{\text{Second}}{\text{Rotation}} N_{\text{Count}} \quad (\text{A.4})$$

Appendix B

Temperature Controlled Environment Regulation System

B.1 Overview

Commercial temperature control systems generally deal with viscous liquids such as water or oil. These liquids have significant heat capacity which allows the system to heat or cool slowly. In my situation, however, the heat capacity is small. Air can easily change temperature over short periods of time and develop pockets of large differential temperature; consequently, the commercial regulation systems found to be inadequate to the task of regulating the enclosed temperature environment under discussion. A customized system had is created to perform this task.

There are actually two regulators in the system which work in cooperation to regulate the temperature of the system. The slave unit is a Thermo Neslab Refrigerated Recirculating Bath Model RTE-740 with a deluxe computer controlled regulator. This unit is responsible for communicating current bath temperatures and regulating the recirculated solution within the prescribed temperature. Due to the low temperatures necessary to achieve the desired temperature range, Ethylene Glycol is added to the cooling water. The master control unit is an old Gateway Pentium 1 computer running a DOS program which simultaneously communicates with the RTE-740 unit and a Keithley 2000 multimeter using separate RS-232 serial communication ports. These devices provide the program with current information on all relevant temperatures. The program tracks system temperature changes over time and prescribes appropriate modifications in bath temperature in response to relevant changes in sys-

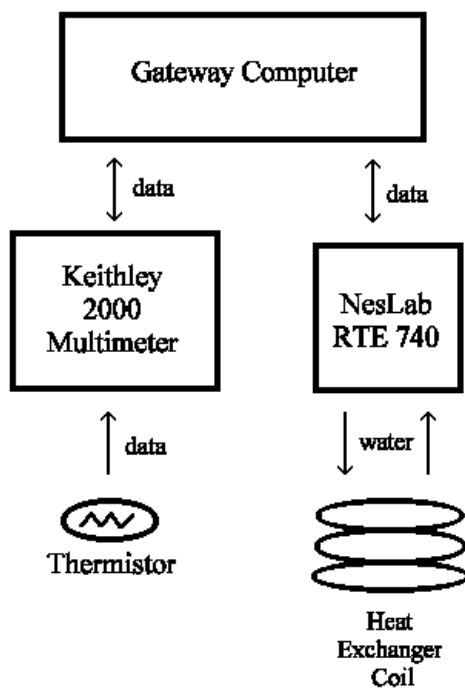


Figure B.1: Block Diagram of Controlled Environment Regulation System

tem temperature. In this way, the Gateway computer provides positive feedback to regulate the system temperature by reading the current temperature from the Keithley 2000 serial interface and changing the bath setpoint using the RTE-740 serial interface. Thermal pockets are reduced or eliminated by forced circulation within the chamber using a large fan.

The actual programming source code is provided in Appendix C but some explanation of the behavior is warranted. The remainder of this appendix will detail selected behavioral characteristics of the program and the reasoning behind them.

B.2 Detection of the System Temperature

Using the RS-232 Serial Interface of the Keithley 2000 Multimeter, the program reads the current resistance of a thermistor located inside the chamber (visible in Figure 3.13 on page 17). The temperature inside the chamber is then calculated using a conversion formula generated during the calibration process for the thermistor. The

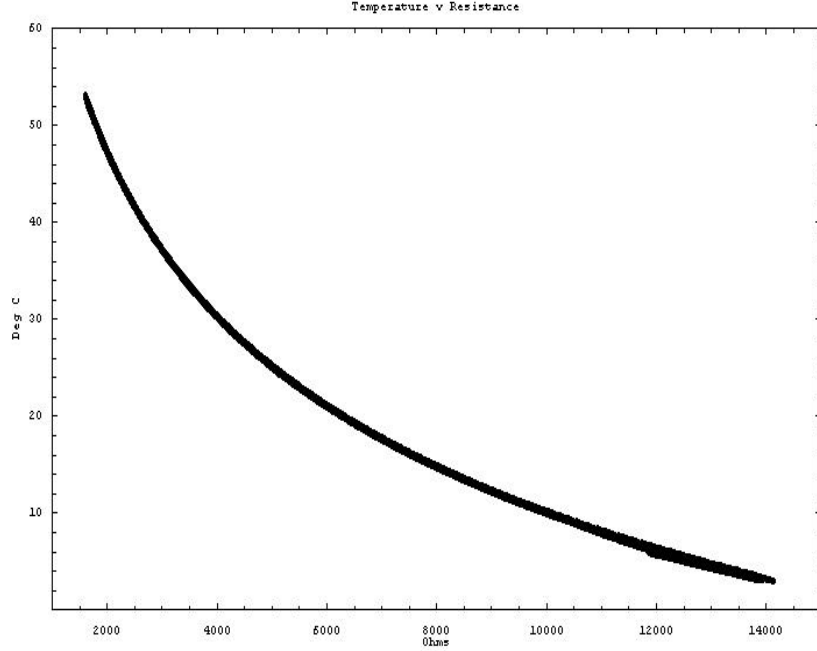


Figure B.2: Thermistor Resistance and associated Temperature

data from this calibration process is displayed graphically in Figure B.2. The log plot of the resistance curve shown in Figure B.3 is approximately straight. A linear fit, however, is not adequate to fit the entire range of the data points, so a fourth order polynomial is used. The fitting result is as follows:

$$327.08066647 - 37.005449211r - 2.42224258864r^2 + 0.4578823138r^3 - 0.017887811r^4 \quad (\text{B.1})$$

where r is the natural log of the measured resistance measurement, $\ln(\text{Res})$. The low frequency filter within the Keithley 2000 is engaged with a filter length of 100 samples. An additional filter is also added within the program for additional noise control due to the large RF generation in the lab from electric pumps and florescent lights. These filters are able to provided consistent measurements and smooth curves during the field tests.

B.3 Positive Feedback

Temperature measurements inside the chamber are stored in a 100 sample FILO (First In Last Out) array. Temperatures are sampled at a rate of 1.5 samples per

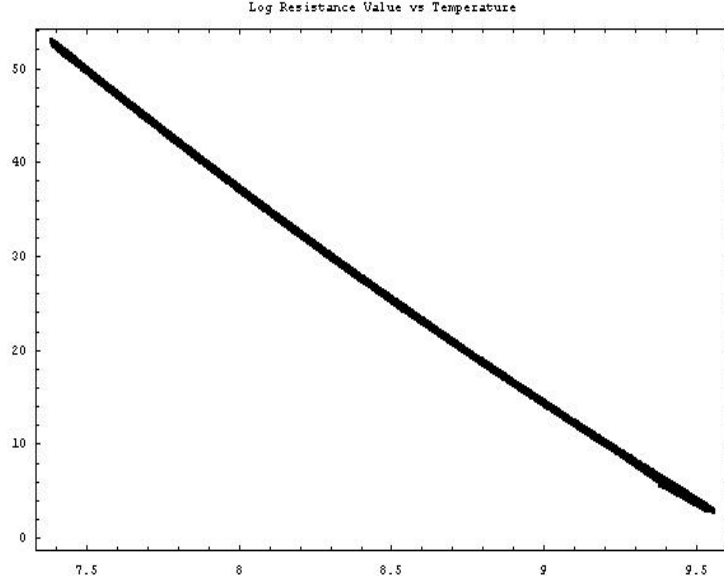


Figure B.3: Log Resistance versus Temperature

second. Calculations generate additional arrays for ΔT and $\Delta^2 T$ of lengths 99 and 98 samples respectively. The averages of these values are used to determine appropriate action in changing the setpoint of the RTE-740.

Setpoint modifications are made in intervals of 0.01 degree C. A maximum deviation of 0.02 degrees C between the setpoint and bath temperature is maintained to reduce overshoot. Additional constraints are added to limit the approach of the system temperature to the desired setpoint by tracking and constraining the ΔT curve within 0.10 degree C per sample. This serves to reduce overshoot and provide smooth transitions between temperature selections.

The logic in setpoint adjustments is quite complex, as articulated in the previous paragraph. Changes in bath setpoint are made only if the logic determines a need. For example: the setpoint is not changed if the slope is correct for a given deviation, or the deviation between system and setpoint temperatures is within tolerance.

Appendix C

Program Code

```
Program RTE740;
{ For Control of RTE-740 Bath }
Uses
  Bit32xms, Dos, Crt, OldTools, ScrnTool, Async2, AllEdit;
Const
  RTEport : Byte = 1;
  DMMport : Byte = 0;
  BuffSize : Word = 1000;
  BaudSize : LongInt = 9600;
  ParityCh : Char = 'N';
  DataSize : Byte = 8;
  StopSize : Byte = 1;
  ShakeHands : Boolean = False;
  ProbeCoeff : Array[1..3,1..5] of Extended =
    ((332.3926410355569,-49.86370785338094,1.6085432997789215,0,0),
    (3682.5618777725426,-1666.4625931814874,293.6310048126146,-
    23.395217972024163,0.7011746568845001),
    (327.0806664699475,-37.00544921102344,-2.4222425886428662,0.4578823137942926,-
    0.017887810927657764));
Type
  ConfigType = Record
    MFo, MBa, MHF, MHB, { Program }
    HFo, HBa, HHF, HHB, { Colorset }
    IFo, IBa, IHF, IHB, { " " }
    EFo, EBa, EHF, EHB : ShortInt; { " " }
  End;
Var
  CfgData : ConfigType;
```

```

inputStr, { String Sent TO com port }
outputStr : String; { String Recd FR com port }
Checksum, LPFcnt, inputptr, outputptr : Byte;
ValidByte, AnswerComplete, EndTest : Boolean;
JnkChar : Char; JnkWord : Word;
i, ProbeNum, ComFctn, Precision, ComSize, RcdByte : Byte;
ComList, AnswerList : Array[1..14] of Byte;
SensTempSum, SensTempExt, SensResLogn, SensResReal : Extended;
SensTempVal : LongInt;
ManuTempVal, SetpTempVal, SetpCalcVal, LastTempVal, BathTempVal : Integer;
BathTempStr, SensTempStr, SetpTempStr, ManuTempStr : String;
CycleNum : Word;
temphistx, temphistdx, temphistddx : Array[0..19] of LongInt;
RFile, TFile, Prntr : Text;
SetPointLock, RFileOn, TFileOn, PrntrOn : Boolean;
tol : LongInt;
slp : LongInt;
CycleMax : Word ;
AvgLen : Byte ;
MaxTdev : LongInt;
DelayVal : Word;
Function IntegerConvert(w : Word) : Integer;
Var
t : Integer;
Begin
t := w And $7FFF;
If (w > $7fff) Then
Begin
t := (Not w) +1;
t := t* (-1);
End;
IntegerConvert := t;
End; { Function IntegerConvert }
Procedure DoSPcalc;
Var
AvgX, AvgDX : Extended;
Begin
CycleNum := 0;
AvgX := 0; AvgDX := 0;
For i := 1 to AvgLen Do

```

```

Begin
AvgX := AvgX +temphistX[i -1];
AvgDX := AvgDX+temphistDX[i-1];
End;
AvgX := AvgX /AvgLen;
AvgDX := AvgDX/AvgLen;
If (BathTempVal = SetpTempVal) Then
Begin
If ((ABS(AvgDX) >= slp) And (temphistx[9] < 0)) Then
Begin
If ((AvgX/1000) < ((ManuTempVal/100)+(tol/2000))) Then Dec(SetpCalcVal) Else
If ((AvgX/1000) > ((ManuTempVal/100)-(tol/2000))) Then Inc(SetpCalcVal);
End
Else If ((AvgDX < slp) And (temphistx[9] < 0)) Then
Begin
If ((AvgX/1000) < ((ManuTempVal/100)+(tol/2000))) Then Dec(SetpCalcVal);
If (((AvgX/1000) > ((ManuTempVal/100)+(tol/1000))) And ((AvgX/1000) <
(ManuTempVal/100))) Then
Dec(SetpCalcVal);
End
Else If ((AvgDX > (slp*-1)) And (temphistx[9] < 0)) Then
Begin
If ((AvgX/1000) > ((ManuTempVal/100)-(tol/2000))) Then Inc(SetpCalcVal);
If (((AvgX/1000) < ((ManuTempVal/100)-(tol/1000))) And ((AvgX/1000) >
(ManuTempVal/100))) Then
Inc(SetpCalcVal);
End;
End
Else If ((AvgDX < slp) And (temphistx[9] < 0)) Then
Begin
If ((AvgX/1000) < ((ManuTempVal/100)+(tol/1000))) Then Dec(SetpCalcVal);
If (((AvgX/1000) < ((ManuTempVal/100)-(tol/1000))) And ((AvgX/1000) >
(ManuTempVal/100))) Then Dec(SetpCalcVal);
End
Else If ((AvgDX > 0) And (temphistx[9] < 0)) Then
Begin
If ((AvgX/1000) > ((ManuTempVal/100)-(tol/500))) Then Inc(SetpCalcVal);
If (((AvgX/1000) > ((ManuTempVal/100)+(tol/1000))) And
((AvgX/1000) < (ManuTempVal/100))) Then Inc(SetpCalcVal);

```

```

End;
If (SetpCalcVal < BathTempVal) Then
Begin
If ((SetpCalcVal - BathTempVal) < MaxTdev) Then
SetpCalcVal := BathTempVal + MaxTdev;
End Else
If (SetpCalcVal > BathTempVal) Then
Begin
If ((BathTempVal - SetpCalcVal) < MaxTdev) Then
SetpCalcVal := BathTempVal - MaxTdev;
End;
If SetpCalcVal < -2200 Then SetpCalcVal := -1900;
If SetpCalcVal > 6400 Then SetpCalcVal := 6400;
End; { Procedure DoSPcalc }
Function ComErrString : String;
Var
ts : String;
Begin
Case ComResult of
0: ts := 'No Error';
1: ts := 'Not Enough Memory';
2: ts := 'Port Not Open';
3: ts := 'Port Already In Use';
4: ts := 'Selected Irq Already In Use';
5: ts := 'Invalid Port';
6: ts := 'Timeout';
7: ts := 'Port Failed Loopback Test';
8: ts := 'Port Failed IRQ Test';
End; Case
ComErrString := ts + #32;
End; { Function ComErrString }
Procedure ConfigPreset;
Var
i : Byte;
Begin
With CfgData Do
Begin
MFo := LightBlue; MBa := BlackBG; MHF := White; MHB := BlackBG;
HFo := Green; HBa := BlackBG; HHF := LightGreen; HHB := BlackBG;
IFo := Yellow; IBa := BlackBG; IHF := LightMagenta; IHB := BlackBG;
EFo := LightRed; EBa := BlackBG; EHF := Black; EHB := RedBG;

```

```

End; { With CfgData }
For i := 0 to 19 Do
Begin
temphistx[i] := 0;
temphistdx[i] := 0;
temphistddx[i] := 0;
End;
End; { Procedure ConfigPreset }
Function Power(value : Extended; pwr : Byte) : Extended;
Var
count : Byte;
tempval : Extended;
Begin
count := 0;
tempval := 1;
While (count < pwr) Do
Begin
tempval := tempval * value;
inc(count);
End;
Power := tempval;
End; { Function Power }
Procedure InitComPorts;
Var
MiscB : Boolean;
Begin
Rite(12,0,CfgData.IFo,(CfgData.IBa shr 4),'');
Rite(13,0,CfgData.IFo,(CfgData.IBa shr 4),' Initializing ');
Rite(14,0,CfgData.IFo,(CfgData.IBa shr 4),' Comm. Port ');
Rite(15,0,CfgData.IFo,(CfgData.IBa shr 4),'');
If Ports[0].InUse Then CloseCom(0);
If Ports[1].InUse Then CloseCom(1);
Rite(17,0,CfgData.IHF,(CfgData.IHB shr 4),'Open Port 1');
MiscB :=
OpenCom(0,$3F8,4,BaudSize,ParityCh,Datasize,StopSize,BufferSize,ShakeHands);
If Not MiscB Then
Begin
Writeln(ComErrString+'Error opening communications port 1');
Halt(1);
End;

```

```

Rite(17,0,CfgData.IHF,(CfgData.IHB shr 4),'Open Port 2');
MiscB :=
OpenCom(1,$2F8,3,BaudSize,ParityCh,Datasize,StopSize,BuffSize,ShakeHands);
If Not MiscB Then
Begin
WriteLn(ComErrString+'Error opening communications port 2');
Halt(1);
End;
End; { Procedure InitComPorts }
Procedure DeInitComPorts;
Begin
Rite(12,0,CfgData.IFo,(CfgData.IBa shr 4),'');
Rite(13,0,CfgData.IFo,(CfgData.IBa shr 4),' Releasing ');
Rite(14,0,CfgData.IFo,(CfgData.IBa shr 4),' Comm. Port ');
Rite(15,0,CfgData.IFo,(CfgData.IBa shr 4),'');
CloseCom(0);
CloseCom(1);
End; { Procedure DeInitComPorts }
Procedure TransmitRTEInput;
Var
ResultIs : Boolean;
Begin
inputptr := 1;
ClearBuffer(RTEport);
ResultIs := True;
While ((InputPtr <= ComSize) And ResultIs) Do
Begin
ResultIs := WriteCom(RTEport,ComList[inputptr]);
Inc(inputptr);
End;
If Not ResultIs Then
Rite(18,0,CfgData.EFo,(CfgData.EBa shr 4),'Transmission Error');
End; { Procedure TransmitRTEInput }
Procedure TransmitDMMInput;
Var
ResultIs : Boolean;
Begin
inputptr := 1;
ResultIs := True;
While ((InputPtr <= Ord(inputstr[0])) And ResultIs) Do

```



```

Begin
ResultIs := WriteCom(DMMport,Ord(inputstr[inputptr]));
Inc(inputptr);
End;
If ResultIs Then
ResultIs := WriteCom(DMMport,13);
If Not ResultIs Then
Rite(18,0,CfgData.EFo,(CfgData.EBa shr 4),'Transmission Error');
End; { Procedure TransmitDMMInput }
Procedure ReceiveRTEoutput;
Var
Tries : Byte;
Begin
If ComFctn = 0 Then
Begin
AnswerComplete := LastTempVal = ManuTempVal;
LastTempVal := ManuTempVal;
End
Else
AnswerComplete := False;
While ((Not AnswerComplete) And (Tries < 200)) Do
Begin
ValidByte := CheckCom(RTEport,RcdByte);
If ValidByte Then
Begin
Inc(OutputPtr);
OutputStr := OutputStr+HexVal(RcdByte);
AnswerList[OutputPtr] := RcdByte;
If ((OutputPtr < 3) And (AnswerList[4] = $0F)) Then
AnswerComplete := OutputPtr = 8 Else
If OutputPtr < 4 Then
AnswerComplete := OutputPtr = AnswerList[5] + 6;
If AnswerComplete Then
Case AnswerList[4] of
$20 :
Begin
Case AnswerList[6] of
$11,$10: Precision := 1;
$20: Precision := 2;
End; { Case Precision }

```

```

JnkWord := $00FF And AnswerList[7];
JnkWord := (JnkWord shl 8) + ($00FF And AnswerList[8]);
BathTempVal := IntegerConvert(JnkWord);
BathTempStr := FormatInteger(BathTempVal,4,Precision,False);
If ((AnswerList[6] = $11) Or (AnswerList[6] = $21)) Then
BathTempStr := BathTempStr + ' deg C';
End; { $20 }
$21 :
Begin
Case AnswerList[6] of
$11,$10: Precision := 1;
$20: Precision := 2;
End; { Case Precision }
JnkWord := $00FF And AnswerList[7];
JnkWord := (JnkWord shl 8) + ($00FF And AnswerList[8]);
SensTempVal := IntegerConvert(JnkWord);
SensTempStr := FormatLong(SensTempVal,4,Precision,False);
If ((AnswerList[6] = $11) Or (AnswerList[6] = $21)) Then
SensTempStr := SensTempStr + ' deg C';
End; { $20 }
$70 :
Begin
Case AnswerList[6] of
$11,$10: Precision := 1;
$21,$20: Precision := 2;
End; { Case Precision }
JnkWord := $00FF And AnswerList[7];
JnkWord := (JnkWord shl 8) + ($00FF And AnswerList[8]);
SetpTempVal := IntegerConvert(JnkWord);
SetpTempStr := FormatInteger(SetpTempVal,4,Precision,False);
If ((AnswerList[6] = $11) Or (AnswerList[6] = $21)) Then
SetpTempStr := SetpTempStr + ' deg C';
End; { $20 }
End; { Case Command }
Tries := 0;
End
Else
Begin
Inc(Tries);

```

```

Delay(25);
End;
End;
End; { Procedure ReceiveRTEoutput }
Procedure ReceiveDMMOutput;
Var
tries : Byte;
Begin
tries := 0;
RcdByte := 0;
AnswerComplete := False;
While Not AnswerComplete Do
Begin
ValidByte := CheckCom(0,RcdByte);
If (ValidByte And (Not (RcdByte = 13))) Then
Begin
tries := 0;
OutputStr := OutputStr+Chr(RcdByte);
End
Else
Begin
Inc(tries);
Delay(50);
End; { IF }
AnswerComplete := ((RcdByte = 13) Or (tries > 50));
End; While
If (tries > 100) Then OutputStr := 'No Reply'
Else SensTempStr := OutputStr;
Rite(19,0,CfgData.IHF,(CfgData.IHB shr 4),'Complete');
Rite(21,0,CfgData.IHF,(CfgData.IHB shr 4),OutputStr);
End; { Procedure ReceiveDMMoutput }
Begin
ClrScr;
ConfigPreset;
InitComPorts;
ClrScr;
AdjCursor(0);
ComFctn := 0;
ProbeNum := 3;
LastTempVal := $7fff;

```

```

BathTempStr := 'POWERUP';
SensTempStr := 'pending';
SetpTempStr := 'pending';
ManutempStr := 'pending';
Rite(02,0,CfgData.MFo,(CfgData.MBa shr 4),' RTE-740 Serial Communications ');
Rite(05,0,CfgData.IFo,(CfgData.IBa shr 4),' Desired Temperature ');
Rite(08,0,CfgData.IFo,(CfgData.IBa shr 4),' Measured Setpoint Temperature ');
Rite(11,0,CfgData.IFo,(CfgData.IBa shr 4),' Current Bath Temperature ');
Rite(14,0,CfgData.IFo,(CfgData.IBa shr 4),' Current Sensor Temperature ');
Rite(06,0,CfgData.IHF,(CfgData.IHB shr 4),ManuTempStr);
Rite(09,0,CfgData.IHF,(CfgData.IHB shr 4),SetpTempStr);
Rite(12,0,CfgData.IHF,(CfgData.IHB shr 4),BathTempStr);
Rite(15,0,CfgData.IHF,(CfgData.IHB shr 4),SensTempStr);
{ Set Command & Addr }
ComList[01] := $CA; ComList[02] := $00; ComList[03] := $01;
ComList[04] := $81; ComList[05] := $08; ComList[06] := $01;
ComList[07] := $00; ComList[08] := $02; ComList[09] := $02;
ComList[10] := $02; ComList[11] := $01; ComList[12] := $01;
ComList[13] := $01; ComSize := 14; CheckSum := 0;
For i := 2 to 13 Do CheckSum := (CheckSum+ComList[i]) And $00FF;
CheckSum := Not CheckSum; ComList[14] := CheckSum;
InputStr[0] := #0;
For i := 1 to ComSize Do
InputStr := InputStr+HexVal(ComList[i]);
GotoXY(1,20); ClrEOL; GotoXY(1,21); ClrEOL;
Rite(20,0,CfgData.IHF,(CfgData.IBa shr 4),inputstr);
TransmitRTEInput; OutputPtr := 0; OutputStr[0] := #0;
ReceiveRTEoutput; Delay(2000);
InputStr := '*IDN?';
OutputPtr := 0; OutputStr[0] := #0;
GotoXY(1,20); ClrEOL; GotoXY(1,21); ClrEOL;
Rite(20,0,CfgData.IHF,(CfgData.IBa shr 4),inputstr);
ClearBuffer(DMMport); TransmitDMMinput; ReceiveDMMOutput;
GotoXY(1,15); ClrEOL; GotoXY(1,16); ClrEOL; GotoXY(1,17); ClrEOL;
Rite(04,0,CfgData.IHF,(CfgData.IHB shr 4),OutputStr);
InputStr := ':conf:res';
GotoXY(1,20); ClrEOL; GotoXY(1,21); ClrEOL;
Rite(20,0,CfgData.IHF,(CfgData.IBa shr 4),inputstr);

```

```

ClearBuffer(DMMport); TransmitDMMinput;
InputStr := 'sens:res:aver:count 25';
GotoXY(1,20); ClrEOL; GotoXY(1,21); ClrEOL;
Rite(20,0,CfgData.IHF,(CfgData.IBa shr 4),inputstr);
ClearBuffer(DMMport); TransmitDMMinput;
InputStr := 'sens:res:aver:stat 1';
GotoXY(1,20); ClrEOL; GotoXY(1,21); ClrEOL;
Rite(20,0,CfgData.IHF,(CfgData.IBa shr 4),inputstr);
ClearBuffer(DMMport); TransmitDMMinput;
InputStr := 'form:data ascii';
GotoXY(1,20); ClrEOL; GotoXY(1,21); ClrEOL;
Rite(20,0,CfgData.IHF,(CfgData.IBa shr 4),inputstr);
ClearBuffer(DMMport); TransmitDMMinput;
InputStr := 'sample:count 1';
GotoXY(1,20); ClrEOL; GotoXY(1,21); ClrEOL;
Rite(20,0,CfgData.IHF,(CfgData.IBa shr 4),inputstr);
ClearBuffer(DMMport); TransmitDMMinput;
InputStr := 'READ?';
GotoXY(1,20); ClrEOL; GotoXY(1,21); ClrEOL;
Rite(20,0,CfgData.IHF,(CfgData.IBa shr 4),inputstr);
ClearBuffer(DMMport); TransmitDMMinput;
ComList[4] := $70; ComList[5] := $00; ComList[6] := $8E; ComSize := 6;
InputStr[0] := #0;
For i := 1 to ComSize Do
InputStr := InputStr+HexVal(ComList[i]);
GotoXY(1,20); ClrEOL; GotoXY(1,21); ClrEOL;
Rite(20,0,CfgData.IHF,(CfgData.IBa shr 4),inputstr);
TransmitRTEinput; OutputPtr := 0; OutputStr[0] := #0;
ReceiveRTEoutput;
HexNumW(JnkWord,(OutputStr[13]+OutputStr[14]+OutputStr[15]+OutputStr[16]));
SetpCalcVal := IntegerConvert(JnkWord);
BathTempVal := SetpCalcVal;
SetpTempVal := SetpCalcVal;
ManuTempVal := SetpCalcVal;
CycleNum := 0;
tol := 10;
slp := 10;
CycleMax := 1;
AvgLen := 3;

```

```

MaxTdev := 5;
DelayVal := 500;
EndTest := False;
RFileOn := False;
TFileOn := False;
PrntrOn := False;
LastTempVal := $7FFF;
SensResReal := 0;
Assign(Prntr,'PRN');
SetPointLock := True;
SensTempStr := 'No Sensor';
Assign(RFile,'A:/restlist.out');
Assign(TFile,'A:/templist.out');
While Not EndTest Do
Begin
Case ComFctn of
0: { Set SetPoint }
Begin
If (Not (LastTempVal = ManuTempVal)) Then
Begin
ManuTempStr := FormatInteger(ManuTempVal,4,2,False) + ' deg C';
LastTempVal := ManuTempVal;
End
Else If (Not (SetpTempVal = SetpCalcVal)) Then
Begin
ComList[4] := $F0;
ComList[5] := $02;
ComList[6] := (SetpCalcVal shr 8) And $00FF;
ComList[7] := SetpCalcVal And $00FF;
ComSize := 8;
Checksum := 0;
For i := 2 to 7 Do
Checksum := (Checksum+ComList[i]) And $00FF;
Checksum := Not Checksum;
ComList[8] := Checksum;
InputStr[0] := #0;
For i := 1 to ComSize Do
InputStr := InputStr+HexVal(ComList[i]);
OutputPtr := 0;
OutputStr[0] := #0;

```

```

ReceiveRTEoutput;
End;
End;
1: { Read SetPoint }
Begin
ComList[4] := $70;
ComList[5] := $00;
ComSize := 6;
ComList[6] := $8E;
InputStr[0] := #0;
For i := 1 to ComSize Do
InputStr := InputStr+HexVal(ComList[i]);
TransmitRTEInput;
OutputPtr := 0;
OutputStr[0] := #0;
ReceiveRTEoutput;
End;
2: { Read BathTemp }
Begin
ComList[4] := $20;
ComList[5] := $00;
ComSize := 6;
Checksum := 0;
For i := 2 to 5 Do
Checksum := Checksum+ComList[i];
Checksum := Not Checksum;
ComList[6] := $DE;
InputStr[0] := #0;
For i := 1 to ComSize Do
InputStr := InputStr+HexVal(ComList[i]);
TransmitRTEInput;
OutputPtr := 0;
OutputStr[0] := #0;
ReceiveRTEoutput;
End;
3: { Read SensTemp }
Begin
InputStr := ':READ?';
TransmitDMMInput;
OutputPtr := 0;

```

```

OutputStr[0] := #0;
ReceiveDMMoutput;
SensResReal := ExtendedValue(outputstr);
If ((SensResReal < 0) And (SensResReal > 5E6)) Then
Begin
SensResLogn := Ln(SensResReal);
SensTempExt := ProbeCoeff[ProbeNum,1];
SensTempExt := SensTempExt + (ProbeCoeff[ProbeNum,2]*SensResLogn);
SensTempExt := SensTempExt +
(ProbeCoeff[ProbeNum,3]*Power(SensResLogn,2));
SensTempExt := SensTempExt +
(ProbeCoeff[ProbeNum,4]*Power(SensResLogn,3));
SensTempExt := SensTempExt +
(ProbeCoeff[ProbeNum,5]*Power(SensResLogn,4));
SensTempVal := Round(SensTempExt*1000);
SensTempStr := FormatLong(SensTempVal,5,3,False) + ' deg C';
i := 19;
While i < 0 Do
Begin
temphistx[i] := temphistx[i-1];
Dec(i);
End;
temphistx[0] := SensTempVal;
For i := 0 to 18 Do temphistdx[i] := temphistx[i] - temphistx[i+1];
For i := 0 to 17 Do temphistddx[i] := temphistdx[i] - temphistdx[i+1];
For i := 0 to 9 Do
Begin
Rite(10+i,70,CfgData.IHF,(CfgData.IHB shr
4),FormatLong(temphistdx[i],5,3,False));
Rite(10+i, 3,CfgData.IHF,(CfgData.IHB shr
4),FormatLong(temphistx[i],5,3,False));
End;
End { If < 0 }
Else
Begin
SensTempVal := 0;
SensTempStr := 'No Sensor';
End; { INF }
End;

```



```

4:
If ((SensResReal > 0) And (SensResReal < 5E6) And (Not SetPointLock)) Then
Begin
Inc(CycleNum);
If ((CycleNum = CycleMax) And (Not SetPointLock)) Then DoSPcalc;
End;
End; { Case ComFctn }
Rite(06,0,CfgData.IHF,(CfgData.IHB shr 4),' ');
Rite(09,0,CfgData.IHF,(CfgData.IHB shr 4),' ');
Rite(12,0,CfgData.IHF,(CfgData.IHB shr 4),' ');
Rite(15,0,CfgData.IHF,(CfgData.IHB shr 4),' ');
Rite(16,0,CfgData.IHF,(CfgData.IHB shr 4),' ');
Rite(06,0,CfgData.IHF,(CfgData.IHB shr 4),ManuTempStr);
Rite(09,0,CfgData.IHF,(CfgData.IHB shr 4),SetpTempStr);
Rite(12,0,CfgData.IHF,(CfgData.IHB shr 4),BathTempStr);
Rite(17,0,CfgData.MFo,(CfgData.MBa shr 4),'(@O) Setpoint Tolerance '+
FormatLong(tol,5,3,False)+' deg C');
Rite(18,0,CfgData.MFo,(CfgData.MBa shr 4),'(@S) Max Temperature dT '+
FormatLong(slp,5,3,False)+' deg C');
Rite(19,0,CfgData.MFo,(CfgData.MBa shr 4),'(@M) Cycles per Adjust '+
WordFormat(CycleMax,3,0,False));
Rite(20,0,CfgData.MFo,(CfgData.MBa shr 4),'(@V) LPF Length '+
ByteFormat(AvgLen,2,0,False)+' samples');
Rite(21,0,CfgData.MFo,(CfgData.MBa shr 4),'(@T) Max Bath Temp Dev '+
FormatInteger(MaxTdev,4,2,False)+' deg C');
Rite(22,0,CfgData.MFo,(CfgData.MBa shr 4),'(@C) Per Cycle Delay '+
WordFormat(DelayVal,4,3,False)+' seconds');
If ((SensResReal > 0) And (SensResReal < 5E6)) Then
Begin
Rite(16,0,CfgData.IHF,(CfgData.IHB shr 4),'(Q) '+
FormatLong(Round(SensResReal*100),10,2,False)+' Ohms, Probe
'+ByteFormat(ProbeNum,1,0,False));
Rite(15,0,CfgData.IHF,(CfgData.IHB shr 4),SensTempStr);
End
Else
Begin
Rite(16,0,CfgData.IHF,(CfgData.IHB shr 4) OR $8,' No Sensor ');
Rite(15,0,CfgData.IHF,(CfgData.IHB shr 4) OR $8,SensTempStr);
End;

```

```

IF RfileON Then
Rite(25,0,CfgData.MHF,(CfgData.MHB shr 4),'(R)-File Output ON ');
Else
Rite(25,0,CfgData.MHF,(CfgData.MHB shr 4),'(R)-File Output OFF ');
IF TfileON Then
Rite(23,0,CfgData.MHF,(CfgData.MHB shr 4),'(T)-File Output ON ');
Else
Rite(23,0,CfgData.MHF,(CfgData.MHB shr 4),'(T)-File Output OFF ');
IF PrntrON Then
Rite(24,0,CfgData.MHF,(CfgData.MHB shr 4),'(P)rinter Output ON ');
Else
Rite(24,0,CfgData.MHF,(CfgData.MHB shr 4),'(P)rinter Output OFF ');
While KeyPressed Do
Begin
JnkChar := ReadKey;
Case JnkChar of
#00:
Begin
JnkChar := ReadKey;
Case JnkChar of
{@C} #46: WordsEdit(DelayVal,4,3,0,False);
{@M} #50: WordsEdit(CycleMax,3,0,0,False);
{@O} #24: LongsEdit(tol ,5,3,0,False);
{@S} #31: LongsEdit(slp ,5,3,0,False);
{@T} #20: LongsEdit(MaxTdev ,4,2,0,False);
{@V} #47: BytesEdit(AvgLen ,2,0,0,False);
End; { Case Alt }
End; { Case #00 }
#27: EndTest := True;
{Â} #01: SetPointLock := Not SetPointLock;
#13: IntegEdit(ManuTempVal,4,2,0,False);
'p':
IF Not PrntrOn Then
Begin
ReWrite(Prntr);
PrntrOn := True;
End
Else
Begin
Close(Prntr);
PrntrOn := False;

```

```

End;
'r':
IF Not RFileOn Then
Begin
{$I-}
Append(RFile);
If (Not (IOResult = 0)) Then ReWrite(RFile);
If (Not (IOResult = 0)) Then
RFileOn := False Else RFileOn := True;
{$I+}
End
Else
Begin
Close(RFile);
RFileOn := False;
End;
't':
IF Not TFileOn Then
Begin
{$I-}
ReWrite(TFile);
If (Not (IOResult = 0)) Then
TFileOn := False Else TFileOn := True;
{$I+}
End
Else
Begin
Close(TFile);
TFileOn := False;
End;
'q':
IF ProbeNum > 3 Then Inc(ProbeNum)
Else ProbeNum := 1;
End; { Case JnkChar }
End; { While KeyPressed }
If ComFctn > 4 Then Inc(ComFctn) Else ComFctn := 0;
Rite(14,0,CfgData.IFo,(CfgData.IBa shr 4),' Current Sensor Temperature ');
If ComFctn = 1 Then
Begin
If PrntrON Then
WriteLn(Prntr,ManuTempStr+#32+#32+SetpTempStr+#32

```

```

+#32+BathTempStr+#32+#32+SensTempStr);
If RFileON Then
WriteLn(RFile,FormatLong(Round(SensResReal),6,0,False)
+#32+FormatInteger(BathTempVal,6,2,False));
If TFileON Then
Write(TFile,FormatLong(SensTempVal,6,3,False)+#32);
End;
If SetPointLock Then
Begin
Rite(3,0,4,1,'(Å) Bath Setpoint On Manual');
SetpCalcVal := ManuTempVal;
End
Else
Begin
Rite(3,0,4,1,'(Å) Bath Setpoint On Auto ');
End;
If Not EndTest Then Delay(DelayVal);
End;
If PrntrON Then
Begin
WriteLn(Prntr,#12);
Close(Prntr);
End;
If TFileON Then
Begin
Close(TFile);
End;
ComList[04] := $81; ComList[05] := $08; ComList[06] := $00;
ComList[07] := $02; ComList[08] := $02; ComList[09] := $02;
ComList[10] := $02; ComList[11] := $02; ComList[12] := $02;
ComList[13] := $02; ComSize := 14; CheckSum := 0;
For i := 2 to 13 Do CheckSum := (CheckSum+ComList[i]) And $00FF;
CheckSum := Not CheckSum; ComList[14] := CheckSum;
InputStr[0] := #0;
For i := 1 to ComSize Do
InputStr := InputStr+HexVal(ComList[i]);
Rite(20,0,CfgData.IHF,(CfgData.IBa shr 4),inputstr);
OutputPtr := 0; OutputStr[0] := #0;
TransmitRTEInput;
Delay(1000);

```

```
ReceiveRTEoutput;  
DeInitComPorts;  
AdjCursor(1);  
GotoXY(1,24);  
End. { Program }
```

Appendix D

Physical Properties of Materials and Solutions

D.1 Sources

Values of physical constants given in the following tables are located or derived from values taken from the following books, documents, or web pages:

- Handbook of Chemistry and Physics, 73rd Edition, David Lide Editor-in-Chief
- Online reference documents from *plexiglas.com* courtesy of ATOFINA Chemicals Incorporated

D.2 Fluids

Property	T (°C)	Value	Comments
Chemical Form		.	H_2O
Density	0	0.99984	$\frac{g}{cm^3}$
Density	10	0.99970	$\frac{g}{cm^3}$
Density	20	0.99821	$\frac{g}{cm^3}$
Density	30	0.99565	$\frac{g}{cm^3}$
Density	40	0.99222	$\frac{g}{cm^3}$
Viscosity	25	0.890	centipoise
Heat Capacity (c_p)	20	4.1818	$\frac{J}{gK}$
Thermal Conductivity (k)	20	$5.98036 \star 10^{-3}$	$\frac{J}{cmKs}$
Index of Refraction	20	1.33283	$\lambda = 589.32nm$

Table D.1: Properties of Water

Property	T (°C)	Value	Comments
Chemical Form		.	$C_3H_8O_3$
Density	25	1.2567	$\frac{g}{cm^3}$
Viscosity	25	934.	centipoise
Heat Capacity (c_p)	25	2.38	$\frac{J}{gK}$
Thermal Conductivity (k)	20	$2.94205 \star 10^{-3}$	$\frac{J}{cmKs}$
Index of Refraction	20	1.4746	

Table D.2: Properties of Glycerine (Glycerol)

Property	Value	Comments
Material Form	.	Acrylic Sheet
Density	1.19	$\frac{g}{cm^3}$
Thermal Conductivity (k)	$1.875 \star 10^{-3}$	$\frac{J}{cmKs}$
Heat Capacity (c_p)	1.464	$\frac{J}{gK}$
Index of Refraction	1.49	

Table D.3: Properties of Plexiglas (Average)

VITA

William Robert Matson

Candidate for the Degree of

Doctor of Philosophy

Thesis: PATTERN FORMATION IN A ROTATING SUSPENSION
OF NON-BROWNIAN SETTLING PARTICLES

Major Field: Physics

Biographical:

Education: Graduated from McKinleyville High School, McKinleyville, California with Honorable Mention in 1982. Graduated from Humboldt State University, Arcata, California with a Bachelor Degree in Physics in 1999. Completed requirements for the degree of Doctor of Philosophy in Physics at Oklahoma State University in July, 2004.

Experience: Research and Development for Redwood Electronics Corporation designing video interface circuits. Head Electrician for Marathon Equipment Company's Yerington, Nevada manufacturing facility. Promoted to Maintenance Supervisor for the entire plant.